Additive Manufacturing, Experimental Characterization, and Constitutive Modeling of Functionally Graded Polymeric Structures

Zur Erlangung des akademischen Grades Doktor-Ingenieur (Dr.-Ing.)
Genehmigte Dissertation von Iman Valizadeh aus Teheran
Tag der Einreichung: 28.11.2023, Tag der Prüfung: 13.02.2024

1. Gutachten: Prof. Dr. rer. nat. Oliver Weeger
2. Gutachten: Prof. Dr.-Ing. Ralf Müller
Darmstadt, Technische Universität Darmstadt, 2024

TECHNISCHE UNIVERSITÄT DARMSTADT

Mechanical Engineering Department

Cyber-Physical Simulation

Additive Manufacturing, Experimental Characterization, and Constitutive Modeling of Functionally Graded Polymeric Structures

Accepted doctoral thesis by Iman Valizadeh

Date of submission: 28.11.2023
Date of thesis defense: 13.02.2024

Darmstadt, Technische Universität Darmstadt, 2024

Bitte zitieren Sie dieses Dokument als:
URN: urn:nbn:de:tuda-tuprints-267568
URL: http://tuprints.ulb.tu-darmstadt.de/26756
Jahr der Veröffentlichung auf TUprints: 2024

Dieses Dokument wird bereitgestellt von tuprints,
E-Publishing-Service der TU Darmstadt
http://tuprints.ulb.tu-darmstadt.de
tuprints@ulb.tu-darmstadt.de

Acknowledgements

It is with great pleasure that I present this doctoral thesis, the result of four years of research at the Institute Cyber-Physical Simulation (CPS) at the Technical University of Darmstadt. Grateful for the valuable support from individuals who shaped my academic experienc.

First of all, I extend my sincere appreciation to my supervisor, Prof. Dr. rer. nat. Oliver Weeger, for providing me with the valuable opportunity to work under his guidance and for his encouragement, support, and trust throughout the research process. His mentorship and constructive feedback greatly contributed to the successful completion of this thesis. I also express my gratitude to Prof. Dr.-Ing. Ralf Müller from the Institute for Mechanics at TU Darmstadt for his role as my co-advisor and for offering inspiring advice.

I am grateful for the collaboration with colleagues from diverse groups and universities, whose assistance significantly contributed to the success of this project. My sincere appreciation goes to Prof. Dr.-Ing. Edgar Dörsam and Dr.-Ing. Ahmad Al Aboud from Institute of Printing Science and Technology, and Prof. Dr. Thomas Halfmann and Dr. Alexander Bruns from Institute for Applied Physics at TU Darmstadt for providing access to facilities and aiding in mechanical and optical measurements. I am thankful to Dr. Tannaz Tayyarian at the Catholic University of America for her collaboration that greatly assisted this thesis.

I express my gratitude to my colleagues at CPS for the enriching collaborative experience and strong support during this academic journey. Special thanks are extended to Dominik Klein and Juan Camilo Alzate Cobo for carefully proofreading my thesis and their insightful comments, and Yusuf Elbadry for engaging in insightful discussions. Acknowledgment is also due to Monika Müller for her administrative support and Michael Fladerer for supplying the equipment and resources that contributed to the success of this thesis. I am particularly grateful to students whose dedicated efforts were instrumental in the completion of this thesis, especially Jasper Schommartz, Alexander Kohlstetter, Cédric Hammes, and Niklas Hogen.

I express my deepest gratitude to my parents for their strong support and constant presence. my heartfelt thanks are reserved for my wife, Arezoo Moosavifard, for her exceptional encouragement and support throughout my entire Ph.D. study. Without the support of all of you, I would not be in this position today.

Abstract

Vat Photopolymerization-based additive manufacturing methods, such as stereolithography and digital light processing, typically use a single material to fabricate structures, presenting a limitation of this printing method. A potential solution to this constraint involves the utilization of grayscale masked stereolithography (gMSLA) for the purpose of 3D printing functionally graded materials using vat photopolymerization. Adjusting the grayscale values of the masks allows precise control over light intensity throughout the material, affecting crosslink density and photopolymer solidification. This control significantly influences the mechanical properties and dimensions of the printed components. In vat photopolymerization, besides grayscale values of the mask, it is crucial to recognize that the resin's curing process is also influenced along the thickness and on curing plane by two other key controllable parameters: layer thickness and exposure time.

In this dissertation, the relationship between gMSLA process parameters and material properties is examined, which results in the development of parametric constitutive models that are dependent on process parameters. A unified parameter, exposure intensity, that combines process parameters to enhance gMSLA for parametric constitutive models is introduced. Depending on the specific application of interest, parametric hyperelastic, visco-hyperelastic, and elasto-visco-plastic constitutive models, all in terms of exposure intensity, are developed and validated through experiments. Subsequently, the study systematically investigates the influence of user-controllable process parameters on geometrical deviations due to overcuring and undercuring. The constitutive parameters and geometrical deviations are represented using hyperbolic tangent functions in terms of exposure intensity. The optimized choice of process parameters enables the engineering design of parts with controllable and graded mechanical behaviors, as well as reliable geometric dimensions using gMSLA. Remarkably, selecting an appropriate parameter set significantly reduces the print time while maintaining identical mechanical behavior. Furthermore, the developed constitutive models are used to analyze energy dissipation in graded shell lattice structures at various strain rates, including the establishment of complementary functions for approximating viscoelastic material dissipation. The observations of material behavior regarding applications in energy absorption show that the tough photosensitive resins suffer from limitation of small failure strain and low plastic deformation. To overcome this limitation the tough resin is blended with a flexible resin to

enhance the structure's flexibility for energy absorption applications significantly, and these systematic studies establish essential relationships for determining constitutive parameters in resin mixtures.

The framework proposed in this dissertation extends the capabilities of photopolymerization-based additive manufacturing, allowing for the creation of intricate structures with customized material behaviors, including mechanical properties, flexibility, and precise geometric dimensions. During the development of this framework, a remarkable consistency is observed between experimental findings and numerical models, suggesting that the obtained results can be transferred to similar material systems and 3D printing technologies.

Zusammenfassung

Vat Photopolymerisationsbasierte additive Fertigungsmethoden, wie Stereolithografie und Digital Light Processing, verwenden in der Regel ein einziges Material zur Herstellung von Strukturen, was eine Einschränkung dieser Druckmethode darstellt. Eine potenzielle Lösung für diese Beschränkung besteht in der Verwendung der grauskalierten maskierten Stereolithografie (gMSLA) zum Zweck des 3D-Drucks funktional abgestufter Materialien unter Verwendung der Vat-Photopolymerisation. Die Anpassung der Grauwerte der Masken ermöglicht eine präzise Kontrolle über die Lichtintensität im gesamten Material, was die Vernetzungsdichte und die Aushärtung des Photopolymers beeinflusst. Diese Kontrolle hat einen erheblichen Einfluss auf die mechanischen Eigenschaften und Abmessungen der gedruckten Bauteile. Bei der Vat-Photopolymerisation ist es neben den Grauwerten der Maske entscheidend zu erkennen, dass der Aushärteprozess des Harzes auch entlang der Dicke und auf der Aushärteebene von zwei weiteren wichtigen steuerbaren Parametern beeinflusst wird: der Schichtdicke und der Belichtungszeit.

In dieser Dissertation wird die Beziehung zwischen den Prozessparametern des gMSLA-Verfahrens und den Materialeigenschaften untersucht. Dabei werden parametrische konstitutive Modelle entwickelt, die von den Prozessparametern beeinflusst werden. Ein vereinheitlichter Parameter, die „Belichtungsintensität“, der Prozessparameter kombiniert, um gMSLA für parametrische konstitutive Modelle zu optimieren, wird vorgestellt. Je nach spezifischem Anwendungsbereich werden parametrische hyperelastische, viskohyperelastische und elasto-visko-plastische konstitutive Modelle, alle in Bezug auf die Belichtungsintensität, entwickelt und durch Experimente validiert. Anschließend untersucht die Studie systematisch den Einfluss von benutzersteuerbaren Prozessparametern auf geometrische Abweichungen aufgrund von Überhärtung und Unterhärtung. Die konstitutiven Parameter und geometrischen Abweichungen werden in Bezug auf die Belichtungsintensität mithilfe hyperbolischer Tangensfunktionen dargestellt. Die optimale Auswahl von Prozessparametern ermöglicht es, Bauteile so zu gestalten, dass ihre mechanischen Eigenschaften genau gesteuert und abgestuft werden können. Gleichzeitig werden zuverlässige geometrische Abmessungen durch den Einsatz von gMSLA erreicht. Bemerkenswerterweise führt die Auswahl eines geeigneten Parameter-Sets zu einer signifikanten Reduzierung der Druckzeit bei gleichbleibendem mechanischem Verhalten. Darüber hinaus werden die entwickelten Materialmodelle dazu verwendet, die Energiedissipation

in abgestuften Schalengitterstrukturen bei verschiedenen Dehnungsraten zu analysieren. Hierbei werden ergänzende Funktionen festgelegt, um die Dissipation viskoelastischer Materialien anzunähern. Die Beobachtungen des Materialverhaltens in Bezug auf Anwendungen im Bereich der Energieabsorption zeigen, dass die zähen photosensitiven Harze unter einer Einschränkung bezüglich kleiner Versagensdehnungen und geringer plastischer Verformung leiden. Um diese Einschränkung zu überwinden, erfolgt die Vermischung des zähen Harzes mit einem flexiblen Harz. Dies dient dazu, die Flexibilität der Struktur erheblich zu steigern, insbesondere im Hinblick auf Anwendungen in der Energieabsorption. Die durchgeführten systematischen Studien etablieren wesentliche Zusammenhänge zur Bestimmung der konstitutiven Parameter in Harzmischungen.

Der in dieser Dissertation vorgeschlagene Rahmen erweitert die Möglichkeiten der photopolymerisationsbasierten additiven Fertigung und ermöglicht die Erstellung von komplexen Strukturen mit maßgeschneiderten Materialeigenschaften, einschließlich mechanischer Eigenschaften, Flexibilität und präziser geometrischer Abmessungen. Während der Entwicklung dieses Rahmens wurde eine bemerkenswerte Übereinstimmung zwischen experimentellen Ergebnissen und numerischen Modellen beobachtet, was darauf hindeutet, dass die erzielten Ergebnisse auf ähnliche Materialsysteme und 3D-Drucktechnologien extrapoliert werden können.

Contents

1. Introduction

1.1. Motivation

Additive manufacturing[1], is rapidly gaining popularity as a favorable manufacturing technology. This innovative approach allows for the creation of intricate 3D structures with remarkable precision and efficiency. Numerous studies have highlighted the potential and diverse applications of 3D printing in various fields. Notably, in the realm of bioengineering, it has proven to be promising [1–6]. The utilization of 3D printing in bioengineering opens up new possibilities for advanced tissue engineering and regenerative medicine. The significant advancements in 3D bioprinting technology and its applications in various fields, particularly regenerative medicine, are studied [2]. The research emphasizes the practical applications of 3D bioprinting, such as generating transplantable tissues and organs and developing tissue models for research, drug discovery, and toxicology studies. Furthermore, 3D printing has made significant contributions to the food production industry, where the relationship between process parameters and the properties of printed food products is investigated, and an efficient and precise food manufacturing process using 3D printing technology is established [7]. High-performance materials have also benefited from the advancements in 3D printing technology [8, 9]. The capability to precisely control the microstructure and composition of printed materials has enhanced mechanical, thermal, and chemical properties, opening doors to developing advanced materials with exceptional performance characteristics. The development of microarchitected materials with consistent stiffness per unit mass density, even at ultralow density levels, through additive manufacturing techniques is investigated and demonstrated [8]. The research [8] aims to achieve this goal by exploring the design, production, and mechanical properties of micro-lattices produced through projection micro stereolithography, allowing for the creation of ultra stiff materials across a wide range of densities and constituent materials using additive manufacturing processes. The integration of 3D printing with robotics has brought about remarkable advancements in the field [10, 11]. This combination has led to the creation of complex robotic structures and components, thereby enhancing the capabilities and versatility

[1] Throughout this dissertation, the terms 'additive manufacturing' and '3D printing of polymers' refer to additive manufacturing using photopolymerization of photosensitive resin. Extending this concept to other additive manufacturing methods, as mentioned in the text, would require related investigations.

of robotic systems. A novel ink suitable for 3D printing of highly stretchable elastomers with shape memory and self-healing properties using UV-light-assisted direct-ink-write printing is developed [11]. The functional properties and potential applications of these 3D-printed materials in soft robotics, 4D printing, and biomedical devices, specifically in the context of vascular repair devices, are studied in the research [11]. Moreover, 3D printing has played a significant role in the emergence of 4D printing and functional materials [12–17]. By incorporating smart materials that can change shape or exhibit specific functionalities in response to external stimuli, 4D printing opens up exciting possibilities for dynamic and adaptive structures. A desktop digital light processing (DLP) 3D printer capable of fabricating multiple-sized soft pneumatic actuators with high precision and speed using the projection micro stereolithography method is developed [17]. Additionally, the printer's capability to create and test various pneumatic actuators and a soft pneumatic gripper, highlighting the convenience and efficiency of integral fabrication for micro-sized soft pneumatic actuators through DLP 3D printing, is demonstrated in the study. The world of electronic devices has also undergone the significant effect of 3D printing [18–20]. The ability to fabricate intricate electronic components and devices using 3D printing techniques has led to advancements in flexible electronics and personalized electronic devices. Fully 3D printed lithium-ion batteries with thick semisolid electrodes that possess a high areal capacity are designed, fabricated, and evaluated [18]. The aim is to develop semisolid cathode and anode inks, along with ultraviolet (UV) curable packaging and separator inks, to enable the direct printing of lithium-ion batteries in arbitrary geometries, showing their potential for integration within 3D printed objects while maintaining excellent electrochemical performance.

The production and fabrication of 3D printed polymers include three distinct additive manufacturing concepts: filament, powder based, and resin based [21]. Filament based contains the extrusion and fusion of solid filaments, namely Fused Deposition Modeling (FDM), see Figure 1.1 (a). This method is generally slower and offers decent surface quality but it exhibits good mechanical properties and is economically efficient to construct. The second concept is the Laser sintering of solid powders, referred to as Powder Bed Fusion (PBF), which is another technique. This method is faster than filament-based methods and offers enhanced mechanical properties. However, the build cost is higher than filament-based methods [21]. Finally, there is the photocuring of liquid resins using vat photopolymerization methods, commonly known as stereolithography. Laser-based stereolithography (SLA) tends to be slower due to the movement of a single laser beam across the printing area, while digital light processing (DLP) and masked stereolithography (MSLA) provide faster alternatives, see Figure 1.1 (b) and (c). MSLA utilizes the photocuring of liquid, photosensitive polymer resin. In MSLA, a layer of liquid resin is selectively exposed to UV light, filtered by a liquid crystal display (LCD), resulting in the crosslinking of polymer molecules and the fabrication of solid objects in a layer-by-layer manner. This technique allows for the production of complex geometries with

high accuracy on different scales [22]. MSLA and DLP have similar procedures; however, DLP utilizes a light projector, while MSLA relies on LED arrays in conjunction with LCD photomasks. As a result, DLP and MSLA are better suited for large-scale applications.

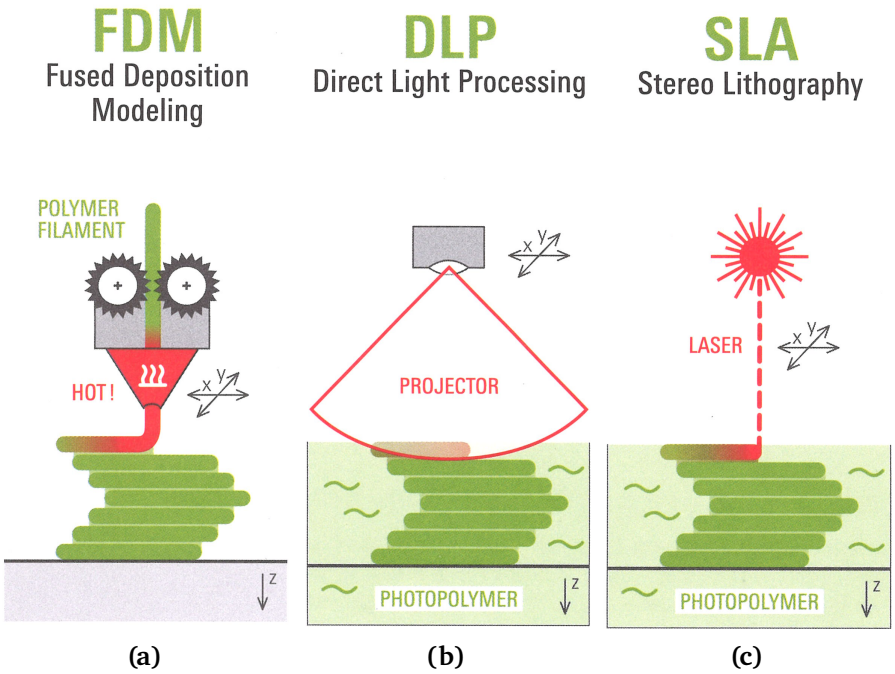

Figure 1.1. Schematic of (a) Fused Deposition Modeling printer, (b) Digital Light Processing, and (c) Stereo lithography with laser. The plot is adapted from [23].

In the vat photopolymerization processes, which is the focus of this research, the influence on the crosslinking process of a polymer under exposure to UV light, as well as the resulting crosslink density, is generally affected by several factors. These factors include light intensity, exposure time, layer thickness, curing temperature, oxygen inhibition, and post-curing temperature [24–28]. In the case of grayscale masked stereolithography (gMSLA), the incident light intensity can be controlled by the user using masks. These masks are not limited to black and white but also allow for intermediate grayscale pixel values [15, 29, 30]. Adjusting the grayscale values of the mask results in a controlled degree of photopolymerization within the resin, thereby enabling precise customization of mechanical properties at individual material points [15]. Moreover, the process parameters of layer thickness and exposure time per layer are readily adjustable.

Recent studies have uncovered that the manipulation of these process parameters has a notable impact on the ultimate mechanical characteristics [31–33]. Consequently, by utilizing grayscale values of pixels, as well as adjusting the exposure time and layer thickness, it becomes possible to regulate the mechanical properties at specific points within each layer. Additionally, this approach enables the control of mechanical properties across multiple layers. As a result,

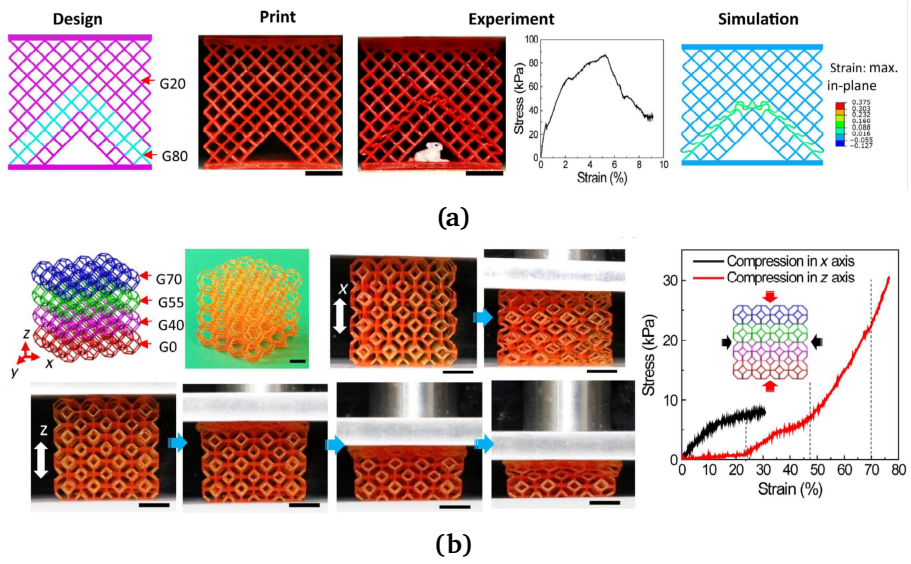

Figure 1.2. The utilization of graded metamaterials created through gMSLA for multifunctional applications. (a) Controlled deformation: designing, printing, conducting compression tests, and FEM analysis of a 2D lattice and cellular metamaterial for controlled buckling. (b) 3D Lattice metamaterial: designing and printing parts for a 3D lattice metamaterial with desired properties and functionalities. The example is adapted from [15].

gMSLA offers the capability to fine-tune mechanical properties throughout a structure, thereby overcoming the limitation associated with vat photopolymerization's single-material printing. An example of fabrication of graded structures is shown in Figure 1.2.A newly developed two-dimensional lattice architecture matrix was fabricated using a grayscale pattern [15]. This pattern consists of a triangular region (G80) and a blank region underneath in Figure 1.2 (a). During the compression experiment, it was observed that the deformation predominantly occurred within the soft material present in the triangular region, while the area underneath remained relatively unaffected. This deliberate buckling phenomenon served as a protective shield, effectively safeguarding the material located beneath the triangular region. This distinctive design played a crucial role in enhancing energy absorption, as evidenced by the consistent decline in stress observed in the stress-strain curve, indicating a stable stress drop. A 3D lattice structure Figure 1.2 (b) was designed with different grayscales assigned to each layer. Compression tests revealed that when compressed along the graded layer direction, the lattice exhibited high initial stiffness but quick failure. In contrast, compression perpendicular to the soft layer resulted in sequential deformation, allowing for lower initial stiffness but a significantly larger reversible strain. This multilayer structure demonstrated the potential of sequential deformation for energy absorption.

Recognition of the physical behavior under loading and the mechanical properties of 3D printed polymer materials play a fundamental role in determining their functionality and

suitability for various applications. A thorough understanding of the constitutive behavior of these materials is essential for purposes such as design, optimization, and simulation. Therefore, it is essential to develop a comprehensive constitutive model that encompasses the diverse typical behaviors exhibited by polymers. Polymers can generally be categorized as rubber-like elastomers, characterized by a nonlinear stress-strain relationship and have nearly incompressible behavior. Moreover, it is necessary to account for different mechanical behaviors, including the elasticticy, the viscoelastic behavior (resulting from energy dissipation), and plastic deformations. Modifying process parameters such as light intensity, exposure time, and layer thickness have a significant impact on the degree of monomer conversion within the liquid resin, consequently leading to variations in mechanical properties. Therefore, it is essential to investigate their influence on the mechanical properties of the printed polymers. Understanding the correlation between process parameters and mechanical properties is critical, as it facilitates process optimization and enables control over the performance of the printing process. Additionally, it is necessary to establish a link between mechanical behavior and process parameters, which can be accomplished by developing parametric constitutive models that incorporate these variables. From this perspective, it is crucial to study the impact of process parameters on the ultimate mechanical properties. Finally, the limitations of 3D printed polymers using MSLA, e.g. single material printing and low strain to break, have to be improved. The motivation behind this dissertation is to discover suitable solutions and address the challenges associated with the design and modeling of 3D printed polymers using gMSLA through systematic comprehensive numerical and experimental investigations.

1.2. State-of-the-art

One disadvantage commonly associated with vat photopolymerization methods, in comparison to FDM and material jetting techniques, is their inherent limitation of printing only a single material at any given instance [34–37]. This constraint imposes restrictions on the fabrication of multi-material objects featuring heterogeneous properties and functionally graded material characteristics [38–40]. Inkjet 3D printing of photopolymers, in particular, has successfully demonstrated the creation of such objects, despite with limitations associated with small strains and stresses [38–40]. Developing systems that incorporate multiple vats and materials presents a complex challenge [41, 42]. Nevertheless, gMSLA offers a solution by allowing the control of the photopolymer's curing degree through the regulation of light intensity using grayscale masks [15, 43–45]. As a result, functionally graded objects can be achieved not only via vat photopolymerization with digitally defined masks that generate microstructures [45–48], but also through the intentional underexposure of the material using grayscale pixels. It should be noted that this approach generally leads to reduced stiffness due to the lower cross-linking density [13, 15, 29, 49]. Hence, by manipulating the light intensity using grayscale masks, it becomes feasible to regulate the mechanical properties of individual material points or pixels. This capability opens up opportunities for fabricating graded structures with adjustable mechanical material properties, as well as the creation of high-performance and meta-materials [13, 16, 50].

While previous studies have demonstrated the tunability of mechanical properties in printed materials through grayscale values and variations in printing time [15, 29, 31], there have been limited efforts in developing constitutive models that incorporate grayscale values and process parameters for both small and finite deformations. Notably, a recent investigation proposed a physically-based visco-hyperelastic model to describe the influence of light intensity on a photocured polymer [51]. Similarly, constitutive models, including (visco-) hyperelastic formulations, have been developed for FDM-printed thermoplastic elastomers (TPEs) [52] and inkjet-printed photopolymers [53, 54]. The viscoelastic properties of a commercial photopolymer resin used in DLP 3D printing has been further investigated employing experimental tests and model equations to predict material behavior based on the degree of cure and temperature [55]. Moreover, experiments conducted in the research by [56] aimed to establish a relationship between viscoelastic material properties and crosslinking density in photopolymerized materials. In a comprehensive study conducted by [57], an extensive review of constitutive modeling approaches for soft materials, including polymers, is provided.

Previous researches have focused on developing microscopic models to estimate mechanical properties during the curing process [31, 51, 58–61]. Recent studies have explored the detailed investigation of how the formation of polymer chains during the photopolymerization process impacts mechanical properties [31, 62, 63]. However, modeling the complete kinetics of

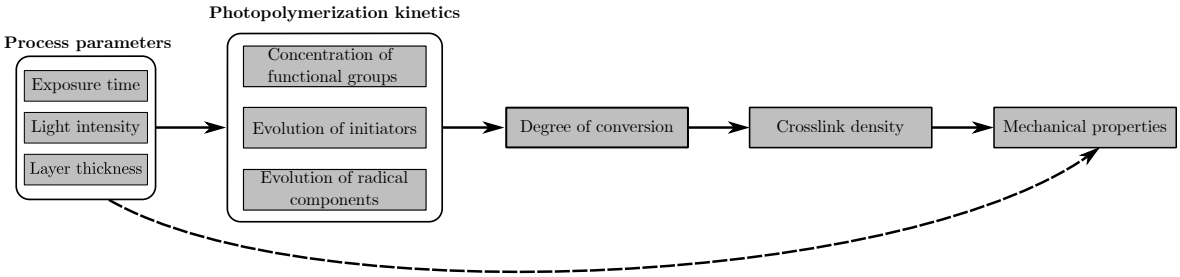

Figure 1.3. Relationship between process parameters and final mechanical properties of a photopolymer material. The dashed line represents the proposed pathway in this thesis, connecting the essential process parameters to the resulting mechanical properties. The solid lines represent typical constitutive modelling path using physically-based models. Similar diagram is shown in [82].

photopolymerization is a complex task that demands extensive experimental characterization of the chemical reaction parameters. Additionally, in the existing literature, the relationship between the degree of conversion and resulting mechanical properties is understood to be only capable of being modeled in a phenomenological manner [31, 64–67]. Therefore, in applications where the emphasis is placed on the final mechanical properties of a specific polymer material fabricated via SLA, it is believed that the characterization of the mechanical behavior in terms of the fundamental parameters, is considered to be the most effective approach. These parameters include the light intensity, the exposure time per layer, and layer thickness, as illustrated in Figure 1.3, and they have a significant influence on the polymerization process and can be easily controlled and adjusted during fabrication. In addition, implementing macroscopic models can offer greater simplicity and numerical efficiency, making them more practical for industrial applications. This concept is demonstrated in Figure 1.3.

In general, elastomers undergoing finite deformations are commonly modeled using constitutive equations of (visco-) hyperelasticity, where a scalar valued energy function describes the material response to deformation and is often expressed in terms of invariants of the right Cauchy-Green tensor [68–72]. The generalized Rivlin model, a three-parameter polynomial hyperelastic material model formulated based on the invariants, is widely employed to characterize elastomers and rubber-like materials [68, 73–75]. Additionally, viscoelastic models [76–78] have been developed to predict and model the mechanical behavior of printed materials. Recent studies have shown that these viscoelastic models exhibit superior accuracy compared to other hyperelastic constitutive models in the modeling of hydrogels [79]. Furthermore, it has been successfully applied to the modeling of 3D printed soft metamaterials [80] and extended to the modeling of 4D printed shape memory polymers [81].

Moreover, the process parameters in gMSLA printing, including light intensity, exposure time, and layer thickness, also affect the geometric accuracy of the printed parts. While previous studies have explored the influence of light intensity on geometrical deviations [29], and the use of grayscale printing methods to control and enhance print quality [45, 83], a systematic

study on the influence of exposure time, grayscale, and their combined effect on geometrical deviations is still needed.

The developed material models mentioned earlier are employed to address practical engineering challenges, including the design and simulation of graded structures. One of the primary objectives in the design of multi-material and graded polymeric structures lies in their capacity for energy absorption applications. Therefore, the examination of energy absorption and dissipation within these materials is essential, particularly in industries such as aerospace, automotive, and packaging. By understanding the underlying mechanisms and properties, the design of materials and structures can be optimized to enhance safety, impact resistance, and overall performance in various applications. By emerging additive manufacturing methods, complicated structures can be explicitly fabricated as polymeric structures. New materials and structures are designed to increase the absorption properties using lattice structures [84–88], multistable structures [89–92] and meta structures [93–96]. Lattice structures, valued for their lightweight and flexible geometry, are investigated for energy absorption. Variation of unit cell topology at different strain rates [84] and hybrid unit cells [88] improve absorption performance. A grading strategy, changing unit cell height and diameter [86], and graded lattice structures with diverse topologies [85] also enhance energy absorption. Lightweight structures exploit element instability to reduce strain peaks [91], while artificial structures with bi-stable units absorb energy through stable configurations. Dual-material auxetic meta-sandwiches fabricated through 4D printing are introduced in [90], which exhibit non-linear stiffness and dissipate energy through mechanical hysteresis. Dual-material auxetic meta-sandwiches, which display non-linear stiffness and dissipate energy through mechanical hysteresis, are introduced through 4D printing [93]. These reversible structures, utilizing the hyperelastic and elasto-plastic properties of polymers, hold promise for 4D printing applications in tunable energy absorption systems.

Upon comparing the literature, it becomes apparent that the establishment of constitutive models is crucial for accurately modeling 3D printed materials in the vat photopolymerization 3D printing method, particularly phenomenological constitutive models that account for large and small deformations. These models should not only encompass the elastic and hyperelastic behavior of the material but also incorporate inelastic behavior, specifically visco-hyperelasticity and plasticity. Furthermore, it is important to investigate the influence of process parameters on the photopolymerization process and express the constitutive relations in terms of these parameters. Additionally, a systematic study needs to be conducted on the geometric deviations that arise from undercuring and overcuring, with a specific focus on the impact of process parameters. The resulting models should not only be theoretically sound but also applicable for practical applications. They should be capable of being implemented within numerical frameworks to facilitate design, optimization, and simulations.

1.3. Aims, Scope, and Structure of this Thesis

The aim of this research is to develop and validate parametric constitutive models to describe the mechanical behavior of gMSLA 3D printed materials. Specifically, it involves the development of a grayscale-dependent hyperelastic model in the initial phase, followed by the investigation and modeling of inelastic behavior under finite deformations, considering the influence of exposure time, light intensity, and layer thickness as process parameters. Furthermore, the study aims to explore the correlation between these process parameters, optimize the fabrication process, establish a strain rate-dependent relationship for energy dissipation, and investigate the potential enhancement of flexibility in 3D printed materials for energy absorption applications.

The scope of this research includes the following key aspects:

- **Hyperelastic Constitutive Modeling**: This study will focus on the development of a hyperelastic constitutive model for gMSLA 3D printed materials in the initial phase. It involves determining constitutive parameters through curve fitting and expressing them as functions of grayscale values. The scope will include the calibration of a parameterized Mooney-Rivlin model based on experimental data, highlighting the grayscale-dependent nature of constitutive and physical parameters.
- **Visco-Hyperelastic Constitutive Modeling**: This research aims to extend the investigation of the inelastic behavior of 3D printed polymers using gMSLA, with a primary focus on materials undergoing finite deformations in the context of viscoelasticity. A parametric visco-hyperelastic constitutive model will be developed. The study will explore the influence of process parameters, including exposure time and light intensity, on material properties and investigate their correlation through a systematic study to unify them into a single design parameter.
- **Linear Elasto-Visco-Plastic Model**: This study includes also the development of an Elasto-Visco-Plastic constitutive model to describe material behavior from initial loading to failure, incorporating layer thickness as process parameter into exposure intensity. It will explore the correlation between process parameters, aiming to optimize the fabrication process for enhanced performance.
- **Geometrical Deviations**: The investigation will also address geometric deviations arising from process parameter variations leading to overcuring and undercuring in the material.
- **Rate Dependent Dissipation of Viscoelastic Materials**: This thesis will analyse energy dissipation in graded structures under different strain rates using the developed parametric constitutive model implemented in Ansys.
- **Flexible 3D Printed Materials**: The thesis will investigate the combination of tough and flexible resins to increase the flexibility of 3D printed materials, especially in the context

of energy absorption applications. The scope extends to examining the feasibility and potential benefits of such combinations.

This dissertation is outlined as follows: Chapter 2 introduces the photopolymerization process and methodology, detailing the experimental setup. Chapter 3 focuses on constitutive modeling in small and large deformations, covering rate-independent and rate-dependent constitutive models. Moving on to Chapter 4, the influence of process parameters on mechanical properties and the validation of parametric constitutive models are discussed. The impact of process parameters on geometrical properties and techniques for correcting geometrical deviations are presented in Chapter 5. Furthermore, Chapter 6 investigates rate-dependent energy dissipation in 3D printed graded structures, examining their mechanical characterization and energy absorption behavior. Chapter 7 focuses on enhancing the flexibility of tough resins by incorporating flexible resins to investigate their impact on key mechanical properties, aiming to find the ideal resin proportion for energy-absorbing applications. Finally, Chapter 8 summarizes key findings, field contributions, and suggests future research.

The research presented in this dissertation has resulted in the following journal publications, oral and poster presentations, and student's thesis:

- Journal Manuscripts:
    1. *Valizadeh, I., Weeger, O. "Rate-dependent energy dissipation of 3D printed graded viscoelastic structures" Preprint submitted to Smart Materials and Structures, (2023).*
    2. *Valizadeh, I., Tayyarian, T., Weeger, O. "Influence of process parameters on geometric and elasto-visco-plastic material properties in vat photopolymerization" In: Additive Manufacturing, 72 (2023), DOI: 10.1016/j.addma.2023.103641.*
    3. *Valizadeh, I., Weeger, O. "Parametric visco-hyperelastic constitutive modeling of functionally graded 3D printed polymers" In: International Journal of Mechanical Sciences, 226 (2022), DOI: 10.1016/j.ijmecsci.2022.107335.*
    4. *Valizadeh, I., Al Aboud, A., Dörsam, E., Weeger, O. "Tailoring of functionally graded hyperelastic materials via grayscale mask stereolithography 3D printing" In: Additive Manufacturing, 47 (2021), DOI: 10.1038/s41467-023-36909-y.*

- Conference Presentations:
    1. *XVII International Conference on Computational Plasticity. Fundamentals and Applications, Barcelona, Spain, September 5-7, 2023.*
    2. *International Design Engineering Technical Conferences & Computers and Information in Engineering Conference, Boston, USA, August 20-23, 2023.*

3. *The Fourth International Conference on Simulation for Additive Manufacturing, Munich, Germany, July 26-28, 2023.*
4. *93rd GAMM Annual Meeting, Dresden, Germany, August 30-2 June, 2023.*
5. *4D Materials Design and Additive Manufacturing Conference , Virtual, September 1-2, 2022.*
6. *92nd GAMM Annual Meeting, Aachen, Germany, August 15-19, 2022.*
7. *15th World Congress on Computational Mechanics & 8th Asian Pacific Congress on Computational Mechanics, Yokohama, Japan, July 31 - August 5, 2022.*
8. *18th European Mechanics of Materials Conference, Oxford, United Kingdom, April 4-6, 2022.*
9. *The 6th European Community on Computational Methods in Applied Sciences Young Investigators Conference, Valencia, Spain, July 7-9, 2021.*
10. *91st GAMM Annual Meeting, Kassel, Germany, March 15-19, 2021.*

- Poster Presentations:
  1. *Graduate School Annual Retreat , Grasellenbach , Germany, May 9-10, 2023.*
  2. *International Conference on Programmable Materials, Berlin, Germany, July 12-14, 2022.*
  3. *Graduate School Annual Retreat, Grasellenbach , Germany, May 2-3, 2022.*

- Master's, Bachelor's & Project Theses:
  1. A Collection and Comparison of Yield Strength Models and Viscoelastic Analysis in Large Deformation, 2023, Author: M. Newton.
  2. Finite element implementation of material models for graded, 3D-printed structures, 2022, Author: A. Kohlstetter.
  3. Experimentelle Untersuchung des Einflusses der Prozessparameter auf die geometrischen Eigenschaften beim Stereolithographie-3D-Druck-Verfahren, 2022, Author: C. Hammes.
  4. Finite cell implementation of finite deformation hyperelasticity with a parametric material model for the analysis of graded structures, 2022, Author: S. Qian.
  5. Experimentelle Untersuchung des Einflusses Lichtintensität auf das Energieaufnahmevermögen des Materials beim Stereolithographie-Verfahren, 2021, Author: D. Tiraspolski.

6. Experimental characterization of minimum feature sizes in grayscale stereolithography 3D printing, Master project, 2020, Author:W. An.
7. Experimental investigation of the influence of process parameters on the material properties in the stereolithography 3D printing method, 2020, Author: N. Hogen.

2. Vat photopolymerization

This chapter provides an explanation of the research methodologies employed, including photopolymerization process and 3D printing, experimental setup, and analytical methods. An introduction to photopolymerization process regarding 3D printing MSLA method is given in Section 2.1. Section 2.2 focuses on the concept of unification of process parameters. Subsequently the experimental methodology, which includes sample preparation, testing procedures, and data analysis, is explained in Section 2.3.

2.1. Introduction to Photopolymerization

This section provides an overview of the theory of photopolymerization and its relationship to the mechanical properties of materials fabricated through masked stereolithography (MSLA).

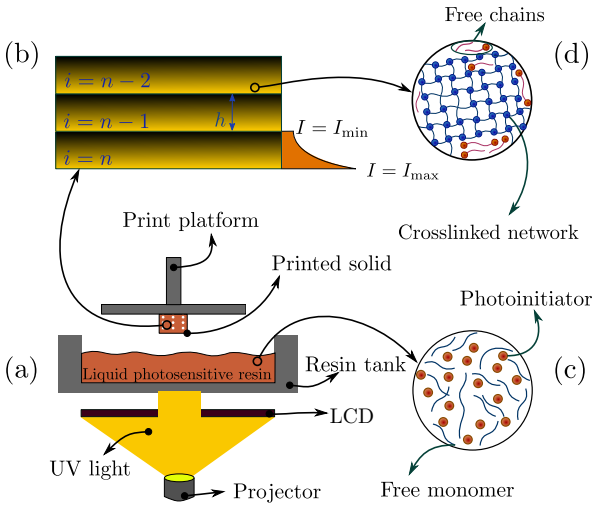

Figure 2.1. The process of vat photopolymerization is depicted schematically. (a) The structure of the printer. (b) The distribution of light intensity within the layers. (c) The constituents of the liquid resin prior to the photopolymerization process. (d) The constituents of the solidified resin following photopolymerization. The representation is adapted from [97].

A typical MSLA printer, as depicted in Figure 2.1 (a), comprises a vat filled with photosensitive polymer, a platform, and projection equipment. The printing process begins with the creation

of the desired objects using computer-aided design (CAD) software, which are then exported as STL file format. These STL files are subsequently imported into slicer software, where grayscale image files, known as masks, are generated for each printing layer. Each mask represents a layer with the desired thickness. Within the slicer software, various printing parameters such as exposure time, layer thickness, and initial exposure time for initial layers are configured. Figure 2.2 provides a more detailed schematic illustration of the MSLA 3D printer architecture, including components such as a UV light source, an LCD module, projection and zoom lenses, a resin tank with a transparent bottom, the printing platform, and grayscaled masks.

In this particular printer, the transmission of light onto the LCD chips is facilitated by the UV light source. This UV light source radiates ultraviolet rays that are directed toward the LCD chips, where masks are uploaded to adjust the light intensity. These masks are designed to selectively block or allow the passage of light based on the desired pattern.

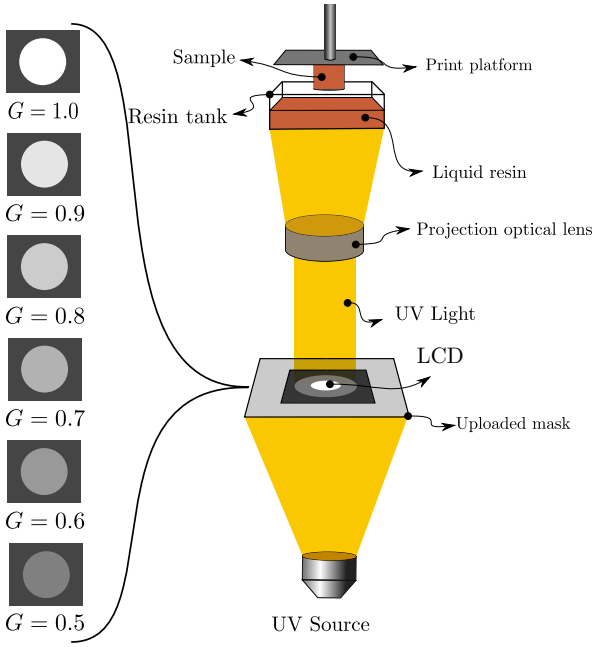

Figure 2.2. A schematic diagram of a projection-based Masked Stereolithography (MSLA) printer. The printer setup typically includes: a UV light source, an LCD module comprising liquid crystals, zoom and projection lenses, and a printer platform. In this setup, the grayscale value G regulates the intensity of light transmitted through the LCD mask, which enables precise control over the curing process during printing. A similar representation is shown in [82].

Afterwards, the light is filtered by the masks and reflected towards the optic lenses. Once the digital mask is uploaded to the LCD, the alignment of the liquid crystals changes based on the color of the pixels in the mask. This determines whether the respective pixel is either fully irradiated or remains uncured. Once the light passes through the filters, it is directed towards the optic lenses, which further concentrate and shape the light beams. The regulation

of the transmitted area is accomplished through optic lenses, whereby the incident light is concentrated onto the liquid photopolymer resin tank. The optic lenses play a crucial role in focusing the light onto a specific area within the resin tank. By carefully controlling the position and intensity of the light, the printer can determine the exact location where the photopolymerization process will occur.

From the bottom interface of the transparent tank, the light penetrates the liquid resin, leading to photopolymerization and subsequent solidification of the resin. Once the concentrated light passes through the bottom of the transparent resin tank, it interacts with the liquid photopolymer resin. The photopolymerization process is triggered, causing the resin to solidify and transform from a liquid state into a solid object.

To capture the solidified material, a platform is immersed in the tank, enabling the first layer of polymer to adhere to the platform. As the resin solidifies layer by layer, the platform is incrementally lifted to allow the formation of the next layer. During this process, the first layer of the polymer adheres to the platform, providing a stable foundation for subsequent layers. Hence, the exposure time for the initial layers is a distinct parameter from the layer exposure time, which needs to be configured in the slicer software.

By repetitively raising the platform and activating the light source, layer-by-layer construction of 3D structures is achieved, see Figure 2.1 (b). After each layer solidifies on the platform, the platform is raised, and a new layer of liquid resin is spread across the previous layer. The light source is then activated again, causing the photopolymerization process to occur for that specific layer. This layer-by-layer process is repeated until the entire 3D structure is completed, resulting in a fully formed and solid object. It has to be noticed that, as the layer thickness increases, the bonding between the layers decreases as a result of light attenuation along the thickness [58, 60].

Figure 2.1 (c) schematically illustrates the principal chemical constituents of a photopolymer resin. A photopolymer resin is fundamentally composed of two main components: monomers and photoinitiators. Monomers are the building blocks of the polymer, while photoinitiators play a crucial role in initiating the polymerization process upon exposure to light. When light penetrates the photopolymer resin, the photoinitiators undergo a process of decomposition, generating active radicals. These active radicals then initiate reactions with the monomers present in the resin, transforming them into active monomers. These active monomers are highly reactive and undergo further reactions with other monomers in the resin.

As the reactions between the active monomers progress, polymeric chains begin to form. These chains undergo a process known as crosslinking, where the chains become interconnected through chemical bonds. This crosslinking process occurs throughout the entire volume of the resin, resulting in the formation and propagation of polymeric chains. The initiation and propagation of radicals in a broader region enable the synthesis of long-chain molecules, further increasing the crosslinking density within the resin. This process ultimately leads to

the production of a solid-state material with enhanced rigidity, see Figure 2.1 (d). The reaction mechanism of photopolymerization, particularly in the context of photopolymerization, is a complex and well-studied area of research. For a more in-depth understanding of the reaction mechanisms involved in photopolymerization refer to the additional references such as [31, 65, 98].

In the context of the photopolymerization procedure, the extent of monomer conversion plays a vital role. The degree of monomer conversion refers to the percentage of monomers that have undergone polymerization and transformed into polymer chains. Higher monomer conversion results in a greater crosslinking density within the resin, thereby enhancing the rigidity and mechanical properties of the final fabricated material. It is important to mention that the influx of light energy into the photoinitiators directly influences the degree of monomer conversion. When a higher amount of light energy is applied to the photopolymer resin, more photoinitiators undergo decomposition, leading to a higher concentration of active radicals and ultimately increasing the degree of monomer conversion. This relationship highlights the importance of controlling the light energy during the photopolymerization process to achieve the desired properties in the final printed material. More information on evolution of mechanical properties in photopolymerization can be found in [15, 51, 97, 99].

2.2. Unification of Process Parameters: Exposure Intensity

As previously mentioned, the objective of this research is to study the impact of the process parameters on the material and geometric properties of gMSLA-printed parts. In commercial MSLA 3D printers, the exposure time t and layer thickness h can typically be adjusted within the slicer or print job preparation software, enabling precise adjustments of the printing process.

To control the light intensity incident on each pixel of the printing layer, RGB or grayscale values G are utilized in the form of masks, as described in Section 2.1. These masks, commonly generated by slicer software and stored as image files, play a crucial role in determining the amount of light that reaches each pixel during the printing process [15, 99]. It is important to note that the relationship between the RGB or grayscale value G and the corresponding light intensity is generally nonlinear [11, 16, 82]. The specific characteristics of the printer structure and the UV light source influence this relationship. For the printer under consideration in this study, the light intensity is measured on the LCD using various grayscale masks. It has been determined in this work that a quadratic correlation exists between the grayscale value G and the irradiance I_e, as illustrated in Figure 2.3. This relation is expressed as

$$I_e(G) = I_e^{\max} \cdot G^2 \,. \tag{2.1}$$

Here, $I_e^{\max}$ represents the maximum irradiance achieved when $G = 1.0$. This quadratic relationship captures the behavior of the specific LCD used in the printer being studied. However, it is important to recognize that the relationship between grayscale values and light intensity may vary for other types of 3D printers, as different printer structures and UV light sources can yield distinct characteristics and response patterns. Therefore, it is necessary to consider the specific characteristics of each printer type when investigating the relationship between grayscale values and light intensity.

As mentioned in the previous section, the crucial factor in the photopolymerization process is the degree of monomer conversion, as it directly impacts the crosslinking density and, consequently, the stiffness of the fabricated material. It is evident that a higher degree of monomer conversion is achieved as more light energy penetrates the photoinitiators. In the stereolithography method, the radiant energy absorbed by the polymer resin, or the local radiant energy density, is primarily influenced by three key parameters: irradiance $I_e(G)$ (also referred to as light intensity), duration of irradiation per layer t, and layer thickness h. For constant layer thickness, increasing the light intensity and exposure time leads to a greater degree of monomer conversion and subsequently enhances the mechanical properties, specifically the stiffness of the final material. The correlation between light intensity regulated through grayscale, and exposure time is schematically depicted in Figure 2.4. This relation between light intensity and duration of irradiation is described by the concept of exposure

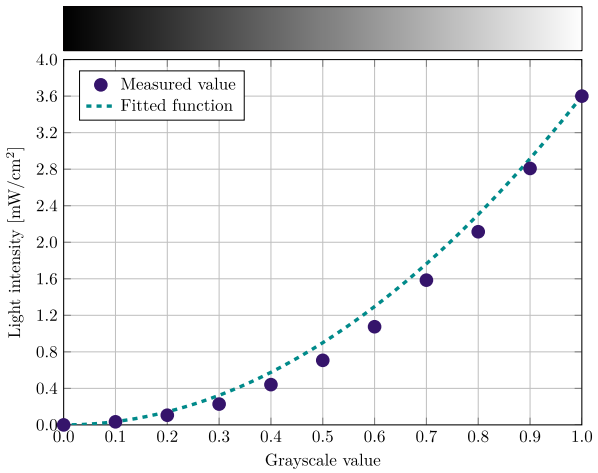

Figure 2.3. The relationship between the surface light intensity I_e on the printer LCD and the grayscale value G of the masks. Through these measurements a quadratic function is determined between light intensity and grayscale values. Similar diagram is shown in [97].

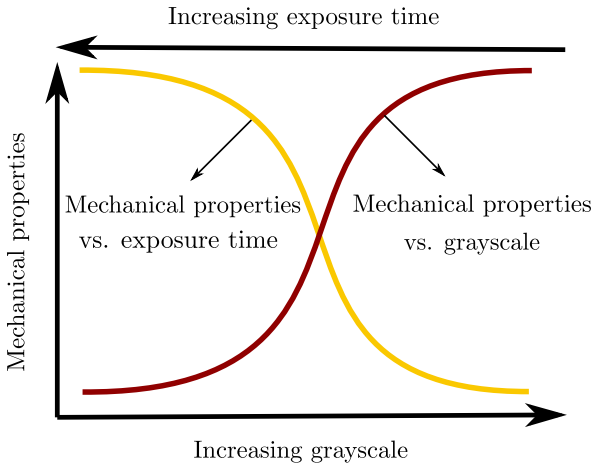

Figure 2.4. Schematical illustration of the correlation of grayscale and exposure time in grayscale Masked Stereolithography. Similar Figure is shown in [82].

intensity, denoted as H_v. To comprehensively capture the interdependence of grayscale value, exposure time, and layer thickness, the concept of exposure intensity is formulated as

$$H_v(G,t,h) = I_e^{\max} \cdot G^2 \cdot \frac{\ln(t/t_0)}{\ln(h/h_0)}\,. \tag{2.2}$$

Here, a logarithmic relationship with respect to layer thickness and exposure time is adopted, inspired by previous investigations [15, 27, 49, 65] and based on experimental observations. In this equation, t_0 and h_0 are model constants that need to be determined. The inclusion of a minimum exposure time $t_0 \leq t$ acknowledges the needed time for radical activation, chain formation, and network development during the photopolymerization process. Similarly, the

minimum layer thickness $h_0 \leq h$ ensures that excessive light penetration through layers is prevented. Exposure intensity is a type of energy density that represents the amount of radiant energy per unit volume absorbed by the polymer resin during the irradiation process. This single unified parameter is calculated based on the process parameters under study, which serve as design parameters.

The maximum irradiance $I_e^{\max}$ plays a critical role in determining the absolute value of H_v and is influenced by factors such as the printer model, UV light source, and LCD type employed. It is important to recognize that the maximum irradiance can vary over the lifespan of a 3D printer and may experience degradation with prolonged operation. As a result, it is highly recommended to conduct regular measurements of the maximum irradiance during practical applications. This helps ensure the reliability, accuracy, and consistency of the obtained results.

Establishing a correlation that captures the geometrical deviations and constitutive parameters, such as coefficients of the material model for different exposure intensity values is crucial for designing parts with graded or optimized properties. To achieve this, a hyperbolic tangent function is employed to approximate a generic parameter Φ as

$$\Phi(H_v) = \Phi_{max} \tanh\left(a\, H_v^2 + b\, H_v + c\right). \tag{2.3}$$

In Equation (2.3), Φ_{max}, a, b, and c are model coefficients that can be determined by fitting the hyperbolic tangent function to experimental data for each specific parameter Φ. This allows for the characterization and prediction of various material and geometrical properties based on the exposure intensity parameter.

2.3. Experimental Methodology

Sample preparation

The specimens were manufactured using the commercial MSLA-printer "Original Prusa SL1s", see Figure 2.5 (a). The printer properties and the print parameters utilized are listed in Table 2.1. Additionally, the commercially available UV-sensitive "Orange Tough Resin" by Prusa Research a.s. was used, see Figure 2.5 (b). The manufacturer provides the material composition as consisting of epoxy resin (40%-50%), monomer (20%-40%), color pigment (2%-5%), and photoinitiators (3%-5%). For the flexible resin the commercially available flexible resin "Siraya Tech Tenacious -Flexible Resin" by Siraya Tech was used, see Figure 2.5 (c). The test samples undergo a design process using CAD software, and are then exported as Standard Tessellation Language (STL) files. These files are subsequently imported into the "PrusaSlicer" software, which generates PNG images of desired layer thickness to be used as masks. This software is also used to set printing parameters, such as the initial layer exposure time and the number of initial layers, as well as the default exposure time for subsequent layers. The initial layers are printed with initial exposure time facilitating a robust adhesion of the layers to the platform substrate. It has been shown that the light intensity, regulated either through grayscale values or exposure time, can have an identical influence on the curing of photopolymers when exposed to UV light [45, 100]. However, while changing the exposure time affects a whole layer, changing the grayscale value affects the curing of each pixel separately. Therefore, in order to control the degree of polymerization at each material point, the exposure time is fixed and the grayscale values of the pixels are varied. In the study of the influence of exposure time and layer thickness, the other two parameters are held constant, and the samples are printed with variations in only one parameter. Since all samples are printed in the center region of the platform, it is assumed that all material points with a certain assigned grayscale value are subject to the same dose of light and exhibit the same degree of cure, even for samples with graded grayscale values.

As previously mentioned, the masks generated by the slicer software contain only black and white pixels, where the white pixels illustrate the shape of the geometry to be printed at the respective layer. Theoretically, the light illuminates through the white pixels at full intensity. Tailoring of material properties is carried out by changing the RGB grayscale values of the pixels, which reduces the light intensity during the printing process [15, 99]. In general, the images used in this study are 8-bit bitmaps, where the full light intensity is represented by white pixels with RGB $= (255, 255, 255)$, resulting in maximal curing of the material at the respective point. On the other hand, black pixels with RGB $= (0, 0, 0)$ cause the liquid resin at the corresponding material point to remain uncured by blocking the light exposure. Furthermore, intermediate levels of curing can be achieved by specifying grayscale RGB values with R $=$ G $=$ B. Here, the grayscale value G corresponds to the light intensity and is used in

(a) **(b)** **(c)**

Figure 2.5. Printer and resins: (a) Commercial MSLA-printer Original Prusa SL1s (picture taken from [101]), (b) Tough resin: UV-sensitive "Orange Tough Resin" by Prusa Research a.s. (c) Flexible resin: UV-sensitive Tenacious-Flexible Resin by Siraya Tech.

this study. Subsequently, MATLAB (version R2020a, The MathWorks Inc.) is used for image processing and adjusting the grayscale values of white pixels. The details of a simple grading code, which alters the color of pixels, are explained in Appendix A.1.

In gMSLA printing, it is important to ensure that the process parameters fall within certain minimum and maximum ranges, which are specific to the printer and material being used. On one hand, if the resin is undercured, it fails to solidify adequately, resulting in poor adhesion between layers and the platform, leading to unpredictable geometric deviations. On the other hand, if the resin is overcured, the printed part may adhere excessively to the glass surface of the resin tank, causing defects and other issues e.g. extensive geometrical deviations. Furthermore, it will be shown in this thesis, that the material's mechanical behavior no longer undergoes additional changes once a certain degree of over-curing is reached. The research conducted in different parts of this study involves variations in grayscales, exposure time, and layer thickness, which are influenced by factors such as the resin, printer projector, and other fundamental parameters that impact the degree of cure and final results. The specific details regarding these variations and their corresponding values can be found in the respective sections of the dissertation, where the effects and implications of these parameter changes are thoroughly discussed and analyzed.

Mechanical testing and measurements

The constitutive model for each grayscale value G is characterized by conducting three mechanical tests: uniaxial tension, uniaxial compression, and volumetric compression. The uniaxial tensile test is conducted in accordance with the ASTM D638 standard, using sample type IV and a test speed of 5 mm/min. The compression and volumetric tests are carried out in accordance with the ISO 7743 standard, using test type A and method A on a cylindrical specimen with a diameter of 29±0.5 mm and a height of 12.5±0.5 mm. The volumetric compression test is conducted using test type B and method B on a cylindrical test specimen with a diameter of 17.8±0.15 mm and a height of 25±0.25 mm. The length changes of the test specimens are measured using a length gauge with 0.2 μm repetition accuracy to calculate the strain in the uniaxial tensile tests.

To perform the tests, a T500-1200-5kN (MFC Sensortechnik GmbH) one column machine according EN ISO 7500-1 is used, which has 1 μm travel resolution accuracy, see Figure 2.6 (a). At least three different test samples, relaxation tests, and cyclic loadings are applied to obtain the elastic, viscoelastic, and elasto–plastic material response. Then, the experimental results from each type of test are averaged for specific G-values, and the averaged value is used for the curve fitting process.

The light intensity $I_e(G)$ is measured on the LCD surface with a slim photodiode power sensor (PM100D with S120VC sensor, Thorlabs Inc., Newton, NJ) with 5% measurement uncertainty Figure 2.6 (b). As can be seen in Figure 2.3, the maximum light intensity[1] of the printer at hand is $I_e^{\max} = 3.6$ mW/cm^2. The geometrical dimensions are measured by optical measurement through image processing. The weight of resin for the mixture is measured using the Foraco Pocket Scales 500 g, a commercial digital scale with a precision of 0.01 grams Figure 2.6 (c).

Data Analysis and Curve Fitting

After collecting data points from the testing machine, the stress and strain values are calculated as follows:

The experimental first Piola-Kirchhoff stress, denoted by $s \in \mathbb{R}$, is calculated using the equation

$$s = \frac{\mathrm{f}}{A_0}\,. \tag{2.4}$$

where $\mathbf{f}$ represents the force vector from the test machine, and A_0 is the cross-sectional area in

[1] The structure of the printer, the LCD, UV light source, and the photosensitive resin have been modified during the course of this thesis. As a result, the absolute values of quantities and results may vary for different parts of this thesis. However, these changes do not impact the core concepts and methodology of this research.

(a)

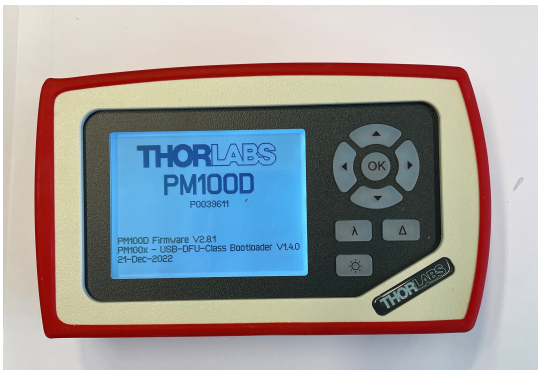

(b)

(c)

Figure 2.6. Test machine and measuring equipment: (a) T500-1200-5kN MFC Sensortechnik GmbH one column machine. (b) Power sensor PM100D with S120VC sensor produced by Thorlabs Inc. (c) Foraco Pocket Scales 500 g, a commercial digital scale with a precision of 0.01 grams.

its initial configuration. The engineering strain, denoted by ε, is calculated using the equation

$$\varepsilon = \frac{\Delta l}{l_0} = \frac{l - l_0}{l_0} = \lambda - 1\,. \tag{2.5}$$

Here, Δl represents the length change, λ is the stretch, and l_0 is the initial length. It should be noted that additional strain measures can be calculated regarding the constitutive model, which will be explained in the next chapter.

After obtaining experimental stress-strain data and numerical results from the constitutive model, the subsequent step involves fitting the numerical data to the experimental data through

Light source	UV LED
Wavelength	405 nm
Light intensity	ca. 3.6 mW/cm^2
Mask	LCD
LCD display size	120×68 mm
Print volume	$120 \times 68 \times 150$ mm
XY-Resolution	0.047 mm
Layer thickness	0.050 mm
Initial exposure time	20 s
Initial exposure layers	10

Table 2.1. Technical data of MSLA 3D printer [101] and the print parameters used.

curve-fitting processes. Briefly, curve fitting is a mathematical technique used to compare experimental stress-strain data with numerical results. It involves adjusting a mathematical curve to closely match the observed data points, aiming to capture the stress-strain relationship accurately. The process begins by selecting a mathematical model that represents the expected stress-strain behavior, which is referred to as a constitutive model within the theory of continuum mechanics. The model's parameters are then iteratively adjusted to minimize the difference between the predicted values and the actual experimental data. Here the least squares method (LS) is employed to optimize the curve fitting process, which involves minimizing the sum of the squared differences between the predicted and actual data points. Once the curve fitting is complete, the fitted curve can be utilized to estimate stress values for untested conditions and analyze the material's behavior under different scenarios, which aids in understanding material properties, validating models, and making predictions for real-world applications.

The curve fitting as non-linear least squares problem is explained briefly in the following. $\boldsymbol{\lambda} = (\lambda_1, \lambda_2, \ldots, \lambda_m)^T$ represents the vector of stretch values ($\lambda_i = l_i/l_0$) for the considered deformation, while $\boldsymbol{s} = (s_1, s_2, \ldots, s_m)^T$ denotes the corresponding stress values, which, depending on the deformation, can be Cauchy or first Piola-Kirchhoff stress. Therefore, $(\boldsymbol{\lambda}, \boldsymbol{s})$ represents the given data pairs.

The material model is defined by the strain-energy function Ψ, which is used to calculate stress as $\boldsymbol{\sigma}(\boldsymbol{\lambda}, \boldsymbol{p}) : \mathbb{R} \times \mathbb{R}^N \to \mathbb{R}$, where $\boldsymbol{p}$ depends on N material parameters denoted by $\boldsymbol{p} = (p_1, p_2, \ldots, p_N)^T$. Further details about stress and the constitutive parameters will be explained in the following sections. To proceed, the objective function is defined as the squared 2-norm

$$SF(\boldsymbol{p}) = \|\boldsymbol{\sigma}(\boldsymbol{\lambda}, \boldsymbol{p}) - \boldsymbol{s}\|_2^2 = \sum_{i=1}^{m} (\sigma(\lambda_i, \boldsymbol{p}) - s_i)^2 \tag{2.6}$$

Thus, the minimization problem is formulated as

$$\min_{\boldsymbol{p}} SF(\boldsymbol{p})\,. \tag{2.7}$$

This problem can be classified as a non-linear least squares problem, if $\boldsymbol{\sigma}(\boldsymbol{\lambda}, \boldsymbol{p})$ exhibits non-linear behavior with respect to $\boldsymbol{p}$ [70]. In this research, **`fmincon`** with 'interior-point' algorithm within MATLAB (version R2020a, The MathWorks Inc.) is utilized for solving the minimization fitting problem.

3. Continuum Mechanical Modeling

This chapter will explore the constitutive modeling of 3D-printed polymers. To begin, fundamental concepts in continuum mechanics, including kinematics and balance laws, will be explained. Subsequently, various material behaviors in finite deformations, such as hyperelasticity, visco-hyperelasticity, and plasticity, will be addressed through constitutive modeling methods. Additionally, the linearized constitutive models will be discussed. This comprehensive discussion will not only clarify these models but also illustrate how they can be parameterized to account for the influence of various process parameters on the material's behavior. A foundational understanding of the construction of parametric constitutive models will be provided, enhancing the comprehension of the relationship between 3D printing parameters and material responses.

3.1. Kinematics

Consider a continuum body denoted as $\mathcal{B}_0 \in \mathbb{R}^3$, which is initially in its material configuration at time $t = 0$, as illustrated in Figure 3.1. Over time, at $t > 0$, the body $\mathcal{B}_0$ undergoes deformation and transfers to a spatial configuration $\mathcal{B}_t \in \mathbb{R}^3$. This deformation is enabled by a deformation map denoted as $\boldsymbol{\varphi}(\mathbf{X}, t)$, which maps points from the material configuration to the spatial configuration, i.e., $\boldsymbol{\varphi} : \mathcal{B}_0 \to \mathcal{B}_t$. The deformation gradient $\mathbf{F}$, defined as the gradient of the deformation map $\boldsymbol{\varphi}$, serves to transform line elements $d\mathbf{X}$ from the material configuration to their counterparts in the spatial configuration, denoted as $d\mathbf{x}$, through the relationship

$$d\mathbf{x} = \mathbf{F}\, d\mathbf{X}\,. \tag{3.1}$$

The concept of volume transformations denoted by J is introduced to account for changes in volume resulting from the deformation. Here, J corresponds to the determinant of the deformation gradient $\mathbf{F}$ and represents the Jacobian of the deformation map. The Jacobian J relates the volume element dV in the material configuration to its corresponding volume element dv in the spatial configuration according to the equation

$$dv = J\, dV\,. \tag{3.2}$$

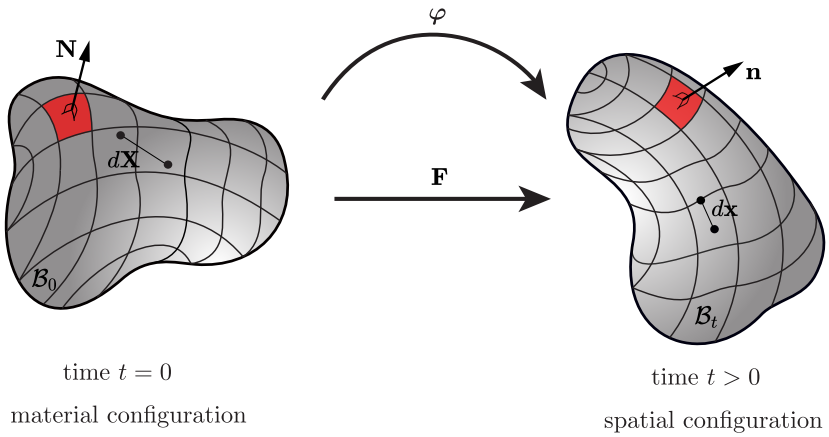

Figure 3.1. The deformation map, denoted as $\boldsymbol{\varphi}$, governs the motion of the body $\mathcal{B}_0$ from its material configuration at $t = 0$ to the spatial configuration $\mathcal{B}_t$ at $t > 0$. Additionally, the linear tangent map $\mathbf{F} := \nabla\boldsymbol{\varphi}$ maps the line element $d\mathbf{X}$ from the material configuration to $d\mathbf{x}$ in the spatial configuration. Similar representation is given in [102].

A displacement vector $\mathbf{u}(\mathbf{X}, t)$ is defined as the difference between the position vectors of the spatial and material configurations.

$$\mathbf{u}(\mathbf{X}, t) = \boldsymbol{\varphi}(\mathbf{X}, t) - \mathbf{X}. \tag{3.3}$$

Now, the deformation gradient can be expressed as

$$\mathbf{F} = \nabla_{\mathbf{X}}[\mathbf{X} + \mathbf{u}(\mathbf{X}, t)] = \mathbf{I} + \nabla_{\mathbf{X}}\mathbf{u} = \mathbf{I} + \mathbf{H}\,. \tag{3.4}$$

Here, the tensor $\mathbf{H}$ is referred to as the displacement gradient and ∇ represents the gradient operator.

In the context of the material configuration denoted as $\mathcal{B}_0$ the first strain tensor is mathematically defined as follows

$$\mathbf{C} := \mathbf{F}^T\mathbf{F}\,, \tag{3.5}$$

which represents the right Cauchy-Green tensor. Here $(\cdot)^T$ represents the transpose operation applied to the deformation gradient tensor. It quantifies the square of the line element $d\mathbf{x}$ in terms of the material line element $d\mathbf{X}$, specifically

$$d\mathbf{x} \cdot d\mathbf{x} = d\mathbf{X} \cdot \mathbf{C} \cdot d\mathbf{X}\,. \tag{3.6}$$

It is important to note that $\mathbf{C}$ is both symmetric and positive definite for every $\mathbf{X}$ belonging to the set $\mathbb{R}^n$.

The other important strain measure in material configuration is defined as follows

$$\mathbf{E} := \frac{1}{2}(\mathbf{F}^T\mathbf{F} - \mathbf{I}) = \frac{1}{2}(\mathbf{C} - \mathbf{I})\,, \tag{3.7}$$

which is commonly known as the Green-Lagrange strain tensor and it is formulated in a manner that its linearization leads to the classical linear strain measure. The Green-Lagrange strain tensor $\mathbf{E}$ can be generalized according to [103] as

$$\mathbf{E}^\alpha = \frac{1}{\alpha}(\mathbf{U}^\alpha - \mathbf{I}), \quad \alpha \in \mathbb{R}\,. \tag{3.8}$$

Notably, when $\alpha = 0$, the strain tensor $\mathbf{E}^{(0)}$ corresponds to the Hencky strain tensor, which is defined as the natural logarithm of the stretch part of the deformation gradient $\mathbf{U}$. This relationship can be expressed mathematically as

$$\mathbf{E}^{(0)} = \ln(\mathbf{U})\,. \tag{3.9}$$

Here, $\ln(\bullet)$ denotes the natural logarithm function, and $\mathbf{U}$ represents the symmetrical stretch tensor. $\mathbf{U}$ can be calculated by the spectral decomposition as

$$\mathbf{U} = \sum_{i=1}^{3} \lambda_i N_i \otimes N_i\,. \tag{3.10}$$

Within these equations, the principal values of the stretch tensors, denoted as λ_i, represent the principal stretches, and N_i is the normal eigenvector in principal direction in material configuration. Consequently, the right Cauchy-Green tensor $\mathbf{C}$ in Equation (3.5) can be written as

$$\mathbf{C} = \mathbf{U}^2 = \sum_{i=1}^{3} \lambda_i^2 N_i \otimes N_i\,. \tag{3.11}$$

In many analytical investigations, the Green-Lagrange strain tensor $\mathbf{E}$ is conventionally expressed using the displacement gradient. However, when employing a numerical approach, this expression becomes dispensable. $\mathbf{E}$ can be derived from Equation (3.4) as shown below

$$\mathbf{E} = \frac{1}{2}(\mathbf{H} + \mathbf{H}^T + \mathbf{H}^T\mathbf{H})\,. \tag{3.12}$$

The presence of the higher-order term $\mathbf{H}^T\mathbf{H}$ highlights the nonlinearity inherent in the Green-Lagrange strain tensor. In the realm of geometrically linear theory, this term is neglected under the assumption that the displacement gradient is of a negligible order ($\mathcal{O}(\|\mathbf{H}\|) \ll 1$).

Under such circumstances, the strain tensor $\mathbf{E}$ simplifies to the linear strain measure $\boldsymbol{\varepsilon}$

$$\boldsymbol{\varepsilon} = \frac{1}{2}(\mathbf{H} + \mathbf{H}^T) = \frac{1}{2}\left(\nabla\mathbf{u} + (\nabla\mathbf{u})^T\right) . \tag{3.13}$$

3.2. Balance Equations

3.2.1. Balance of Mass

In this section, consideration is given exclusively to processes in which the mass within a system is conserved. This requires that the rate of mass change remains at zero ($\dot{m} = 0$). As a result, it is necessary for the infinitesimal mass elements in both the material and spatial configurations to be identical. This requirement leads to the derivation of the following relationship

$$\rho\, dv = \rho_0\, dV . \tag{3.14}$$

Here, ρ_0 and ρ are used to represent the densities in the material and spatial configurations, respectively. By employing Equation (3.2), the volume elements dV and dv can be transformed, resulting in the establishment of the Lagrangian representation of mass balance

$$\rho_0 = J\rho . \tag{3.15}$$

For the sake of completeness, the rate-based form of mass continuity in spatial terms is presented as

$$\dot{\rho}(\mathbf{x}, t) + \rho(\mathbf{x}, t)\,\mathrm{div}\,\mathbf{v}(\mathbf{x}, t) = 0 , \tag{3.16}$$

where $\mathbf{v}(\mathbf{x}, t)$ is the velocity of a material point at spatial configuration and $\dot{\rho}(\mathbf{x}, t)$ is the spatial time derivative of density. This equation is derived from the evaluation of

$$\dot{m} = \frac{D}{Dt}\int_{\mathcal{B}_t} \rho(\mathbf{x}, t)\, dv = 0 . \tag{3.17}$$

3.2.2. Balance of Linear Momentum

The linear momentum is described in both the spatial and material configurations using Equation (3.14) as follows

$$\mathbf{L} = \int_{\mathcal{B}_t} \rho\mathbf{v}\, dv = \int_{\mathcal{B}_0} \rho_0\mathbf{v}\, dV . \tag{3.18}$$

This expression applies to the continuous case. The balance of linear momentum can be stated as follows: The variation in linear momentum $\mathbf{L}$ over time, indicated as the material time derivative, is equal to the summation of all external forces (comprising volume and surface forces) acting upon body $\mathcal{B}$. From a mathematical standpoint, this expression can be

represented as

$$\dot{\mathbf{L}} = \int_{\mathcal{B}_t} \rho \mathbf{b} \, dv + \int_{\partial \mathcal{B}_t} \mathbf{t} \, da \, . \tag{3.19}$$

In this context, $\rho \mathbf{b}$ denotes the volume force, such as gravitational force, and $\mathbf{t}$ signifies the stress vector acting upon the surface of the body $\mathcal{B}$. Cauchy's theorem is employed to establish the relationship between the stress vector $\mathbf{t}$ and the surface normal $\boldsymbol{n}$ through a linear mapping, which is expressed as

$$\mathbf{t} = \boldsymbol{\sigma} \boldsymbol{n} \, . \tag{3.20}$$

This allows the expression of the stress vector in terms of a stress tensor $\boldsymbol{\sigma}$. Subsequently, the local balance equation for linear momentum is derived from Equation (3.19) by applying the divergence theorem. This results in the following local relationship, with respect to the spatial configuration

$$\operatorname{div} \boldsymbol{\sigma} + \rho \mathbf{b} = \rho \dot{\mathbf{v}}. \tag{3.21}$$

In this context, the stress tensor $\boldsymbol{\sigma}$ is referred to as the Cauchy stress tensor, while inertial forces, represented by $\rho \dot{\mathbf{v}}$, can be disregarded in purely static investigations.

3.2.3. Balance of Angular Momentum

The angular momentum with reference to a point O defined by $\mathbf{x}_0$ with position vector $\boldsymbol{r}$ is expressed concerning both the spatial and material configurations using Equation (3.14) as follows

$$\mathbf{M} = \int_{\mathcal{B}_t} (\boldsymbol{r} - \mathbf{x}_0) \times \rho \mathbf{v} \, dv = \int_{\mathcal{B}_0} (\boldsymbol{r} - \mathbf{x}_0) \times \rho_0 \mathbf{v} \, dV. \tag{3.22}$$

The balance of angular momentum can be expressed as: The time rate of change (material time derivative) of angular momentum $\mathbf{M}$ with respect to a point O is equivalent to the summation of all moments originating from external volume and surface forces concerning point O. This can be mathematically expressed as

$$\dot{\mathbf{M}} = \int_{\mathcal{B}_t} (\boldsymbol{r} - \mathbf{x}_0) \times \rho \mathbf{b} \, dv + \int_{\partial \mathcal{B}_t} (\boldsymbol{r} - \mathbf{x}_0) \times \mathbf{t} \, da \, . \tag{3.23}$$

In this context, $\partial \mathcal{B}_t$ represents the boundary of $\mathcal{B}_t$. Following some algebraic manipulations, this equation leads to the local balance of angular momentum, which essentially demands the symmetry of the Cauchy stress tensor

$$\boldsymbol{\sigma} = \boldsymbol{\sigma}^T. \tag{3.24}$$

3.2.4. First Law of Thermodynamics

Another principle governing the conservation of energy in thermodynamic processes is known as the first law of thermodynamics. It is expressed as: the change of the total energy denoted as E over time corresponds to the summation of the mechanical power P originating from all external loads combined with the supply of heat denoted as Q.

$$\dot{E} = P + \mathcal{Q}\,. \tag{3.25}$$

The mechanical power resulting from volume and surface loads is represented as

$$P = \int_{\mathcal{B}_t} \rho \mathbf{b} \cdot \mathbf{v}\, dv + \int_{\partial \mathcal{B}_t} \mathbf{t} \cdot \mathbf{v}\, da. \tag{3.26}$$

The heat source, denoted as $\mathcal{Q}$, is defined as

$$\mathcal{Q} = \int_{\mathcal{B}_t} \rho r\, dv - \int_{\partial \mathcal{B}_t} \mathbf{q} \cdot \boldsymbol{n}\, da\,. \tag{3.27}$$

This supply comprises heat conduction through the body's surface, characterized by the heat flux vector $\mathbf{q}$ and the surface normal $\boldsymbol{n}$, as well as a distributed inner heat source r (specific heat source).

The total energy consists of kinetic energy

$$K = \frac{1}{2} \int_{\mathcal{B}_t} \rho \mathbf{v} \cdot \mathbf{v}\, dv, \tag{3.28}$$

and internal energy

$$U = \int_{\mathcal{B}_t} e\, dv, \tag{3.29}$$

where e signifies the specific internal energy. Substituting these relationships into the Equation (3.25) and performing various manipulations yields the local form of the first law of thermodynamics in spatial configuration as

$$\dot{e} = \boldsymbol{\sigma} : \mathbf{d} + r - \nabla \cdot \mathbf{q}. \tag{3.30}$$

where $\mathbf{d}$ is the rate of deformation tensor. By using piola transformation $\mathbf{Q} = J\,\mathbf{F}^{-1}\mathbf{q}$, the first law of thermodynamics in material configuration is written as

$$\dot{e} = \mathbf{P} : \dot{\mathbf{F}} + R - \nabla \cdot \mathbf{Q}. \tag{3.31}$$

where $\mathbf{Q}$ and R are heat flux vector and distributed inner heat source in material configuration respectively. The second order stress tensor $\mathbf{P}$ is the first Piola-Kirchhoff stress tensor and the

term $\mathbf{P} : \mathbf{F}$ is referred to as stress power.

In the special scenario where no heat is supplied to an elastic body, and no external forces act on it, the conservation of total energy holds true

$$\dot{E} = \dot{K} + \dot{U} = 0 \Rightarrow E = \text{const.} \tag{3.32}$$

3.2.5. Second Law of Thermodynamics

Another essential constraint for constitutive equations arises from the second law of thermodynamics. According to this law, heat cannot flow itself from a system with lower temperature to one with higher temperature. A crucial observation is that a substance with uniform temperature distribution, free of heat sources, can only receive mechanical energy but cannot release it [104]. These observations result in two inequalities that encompass mathematical expressions concerning both local entropy generation and the production of entropy through heat conduction. A fundamental principle states that within irreversible processes, the entropy η of closed systems always increases, and it is essential to determine the direction of the process. By introducing the absolute temperature θ $(\theta > 0)$, the entropy production is expressed as

$$\Gamma = \frac{d}{dt} \int_{\mathcal{B}_t} \rho\eta \, dv - \int_{\mathcal{B}_t} \frac{\rho r}{\theta} \, dv + \int_{\partial\mathcal{B}_t} \frac{1}{\theta} \mathbf{q} \cdot \boldsymbol{n} \, da \, . \tag{3.33}$$

which is known as the Clausius-Duhem inequality in spatial configuration. By elimination of heat source and substitution and mathematical calculation the local form of the Clausius-Duhem inequality in material configuration is written as

$$\mathbf{P} : \dot{\mathbf{F}} - \dot{e} + \theta\dot{\eta} - \frac{1}{\theta} \mathbf{Q} \cdot \nabla\theta \geq 0 \, , \tag{3.34}$$

where $\dot{\mathbf{F}}$ denotes the rate of the strain tensor, and the final term is entropy production by heat conduction. When a uniform temperature distribution is observed, denoted as $\mathbf{Q} = 0$, it implies that there is no heat flux in the absence of a temperature gradient. As a result, the Clausius-Duhem inequality is transformed into a more robust expression of the second law of thermodynamics, often referred to as the Clausius-Planck inequality as

$$\mathcal{D}_{\text{int}} = \mathbf{P} : \dot{\mathbf{F}} - \dot{e} + \theta\dot{\eta} \geq 0 \, , \tag{3.35}$$

with the internal dissipation or local production of entropy, denoted as $\mathcal{D}_{\text{int}}$, which must be non-negative at any point within a body and at all times. In the context of constitutive theory, the free Helmholtz energy Ψ is often introduced using the relation

$$\Psi = e - \eta\theta \, . \tag{3.36}$$

By applying Legendre transformation and time derivative the so-called reduced form of the second law of thermodynamics can be defined for an isothermal process as

$$\mathcal{D}_{\text{int}} = \mathbf{P} : \dot{\mathbf{F}} - \dot{\Psi} \geq 0\,, \tag{3.37}$$

in which $\dot{\Psi}$ is the material time derivative of the energy function. This inequality asserts that the scalar product of the stress tensor and the rate of strain tensor (stress power) must be greater than (for irreversible process) or equal to (for reversible process) the ratio of the rate of internal energy. This inequality describes the dissipation of energy within the material due to irreversible processes.

The Clausius-Planck form of the second law of thermodynamics in Equation (3.37) is reduced to an equality for the class of perfectly elastic materials. The time derivative of the strain energy function is calculated as

$$\dot{\Psi} = \frac{\partial \Psi(\mathbf{F})}{\partial \mathbf{F}} : \dot{\mathbf{F}}\,. \tag{3.38}$$

Inserting Equation (3.38) in Equation (3.37) results in

$$\mathcal{D}_{\text{int}} = \left(\mathbf{P} - \frac{\partial \Psi(\mathbf{F})}{\partial \mathbf{F}} \right) : \dot{\mathbf{F}} = 0\,. \tag{3.39}$$

As $\mathbf{F}$ and, therefore, $\dot{\mathbf{F}}$ can be selected arbitrarily, the expressions within the parentheses must be reduced to zero, which leads to the first Piola-Kirchhoff stress for a hyperelastic material as

$$\mathbf{P} = \frac{\partial \Psi(\mathbf{F})}{\partial \mathbf{F}}\,. \tag{3.40}$$

This method is mostly called Coleman–Noll procedure [105, 106].

The Cauchy stress tensor can be calculated from the first Piola-Kirchhoff stress using Nanson's formula as

$$\boldsymbol{\sigma} = J^{-1} \mathbf{P} \mathbf{F}^{T}\,. \tag{3.41}$$

3.3. Constitutive Modeling

In the study of deformable bodies, the equations mentioned are insufficient to determine the material response. To address this, additional constitutive laws are required to precisely define the material's behavior under specific conditions. These laws aim to approximate the observed physical behavior of the material, considering both linear and nonlinear regimes. In this context, purely mechanical theories are examined, omitting thermodynamic variables like entropy and temperature.

Here, first, a parametric hyperelastic constitutive model is established to describe the mate-

rial's behavior, which is valid for applications subjected to one-time loading until the failure point and at a constant strain rate. Next, the loading rate-dependent behavior is included, and a visco-hyperelastic constitutive model has been developed. Finally, a comprehensive constitutive model is formulated, which can be used to represent the material behavior within elastic-plastic regions, including rate-dependent behavior. This constitutive model aligns with Ansys, which is employed for finite element simulations in this dissertation.

3.3.1. Hyperelasticity

As previously stated, the classification of printed photopolymers primarily focuses on their inherent nature as elastomers with rubber-like characteristics. These materials show a non-linear correlation between stress and strain and exhibit a near-incompressible behavior when subjected to external loads. It has been observed that these materials possess the ability to undergo finite elastic deformations while maintaining minimal alterations in volume during compression [74]. Additionally, it is often assumed that these materials demonstrate isotropic behavior, meaning their properties are direction-independent [32, 107]. To model the behavior of such incompressible or nearly-incompressible materials under finite deformations, hyperelastic constitutive models are commonly employed. These models depend on an energy function and can be formulated in terms of deformation invariants [68]. One well-established hyperelastic constitutive model for elastomers and rubber-like materials is the generalized Rivlin model, which employs a three-parameter polynomial formulation based on invariants of the right Cauchy-Green tensor [68, 73, 74].

This representation is particularly applicable in cases of isotropy, where only the invariants of the strain tensor are considered. Consequently, the Helmholtz free-energy function can be written as

$$\Psi(\mathbf{C}) = \Psi(I_1, I_2, I_3)\,. \tag{3.42}$$

Here, I_a, with $a = 1, 2, 3$ represents the invariants of $\mathbf{C}$ and can be defined as follows

$$\begin{aligned} I_1 &= \text{trace}(\mathbf{C}) = \lambda_1^2 + \lambda_2^2 + \lambda_3^2, \\ I_2 &= \frac{1}{2}\left[\text{trace}(\mathbf{C})^2 - \text{trace}(\mathbf{C}^2)\right] = \lambda_1^2\lambda_2^2 + \lambda_1^2\lambda_3^2 + \lambda_2^2\lambda_3^2, \\ I_3 &= \det(\mathbf{C}) = \lambda_1^2\lambda_2^2\lambda_3^2\,. \end{aligned} \tag{3.43}$$

Here, $\lambda_i, i = 1, 2, 3$ represents the principal stretches of the material. The incompressibility condition for elastomers is denoted by $J = \det(\mathbf{F}) = \lambda_1\lambda_2\lambda_3 = 1$. This condition implies that the volume ratio of an infinitesimal volume element in the spatial and material configurations, represented by J, remains constant during deformation. The symmetry of the strain energy density function is ensured by its invariant based formulation [108].

In certain cases, materials exhibit distinct behaviors in bulk and shear, and the incompressibility constraint directly relates to volumetric strain. To better capture these characteristics, it is advantageous to express the strain energy function as two separate components: one accounting for volumetric (volume-changing) effects and the other for isochoric (volume-preserving) effects [74, 109]. Thus, for nearly incompressible materials, for which $J \approx 1$ holds, Equation (3.42) can be redefined as

$$\Psi = \Psi(\bar{I}_1, \bar{I}_2, J) = \Psi_{\text{vol}}(J) + \Psi_{\text{iso}}(\bar{I}_1, \bar{I}_2), \tag{3.44}$$

where Ψ_{vol} and Ψ_{iso} represent the dilational and distortional terms, respectively. Furthermore, $\bar{I}_1 = J^{-2/3} I_1,\ \bar{I}_2 = J^{-4/3} I_2$ are the isochoric invariants.

Regarding the first Piola-Kirchhoff stress for a hyperelastic material in Equation (3.40), it can be obtained for a hyperelastic material from the strain energy function in terms of invariants as

$$\begin{aligned} \mathbf{P} &= \frac{\partial \Psi(I_1, I_2, I_3)}{\partial \mathbf{F}} = \sum_{i=1}^{3} \frac{\partial \Psi}{\partial I_i} \frac{\partial I_i}{\partial \mathbf{F}} = \mathbf{P}_{\text{vol}} + \mathbf{P}_{\text{iso}}, \\ &\text{with} \quad \mathbf{P}_{\text{vol}} = \frac{\partial \Psi_{\text{vol}}}{\partial \mathbf{F}} \quad \text{and} \quad \mathbf{P}_{\text{iso}} = \frac{\partial \Psi_{\text{iso}}}{\partial \mathbf{F}} \\ P_{iJ} &= \frac{\partial \Psi(I_1, I_2, I_3)}{\partial F_{iJ}}, \end{aligned} \tag{3.45}$$

where $\mathbf{P}_{\text{vol}}$ and $\mathbf{P}_{\text{iso}}$ are the contributions from the dilational and distortional terms of the first Piola-Kirchhoff stress tensor, respectively. It can be observed from the index notation in Equation (3.45) that P_{iJ} represents a two-point tensor wherein one index signifies the spatial coordinates x_i, while the other denotes the material coordinates X_J. For a more detailed understanding of stress tensors and their derivations, additional information can be found in continuum mechanics references such as [109], where further insights into the mathematical formulations and principles underlying the study of materials' mechanical behavior are provided.

The specific formulation of the energy function, whether in terms of $\mathbf{F}$, $\mathbf{C}$, or the invariants, determines the material behavior under loading within the framework of constitutive theory in finite elasticity. Hence, the choice of a material model depends on its intended application and its inherent behavior observed in experimental tests. To fit the experimental characterization data for the material being studied, it is most appropriate to use the Mooney-Rivlin hyperelastic material model, owing to its well-established suitability for modeling elastomers experiencing significant deformations. However, for different materials, other models may need to be explored and found to be more suitable. The general formulation of the Mooney-Rivlin model for incompressible materials is given [73, 74] as

$$\begin{aligned}\Psi &= \Psi(\bar{I}_1, \bar{I}_2, J) \\ &= \frac{1}{d}(J-1)^2 + \sum_{m=0}^{M}\sum_{n=0}^{N} C_{mn}(\bar{I}_1 - 3)^m(\bar{I}_2 - 3)^n,\end{aligned} \tag{3.46}$$

where d represents the incompressibility parameter, and C_{mn} are additional material coefficients. These material parameters need to be determined through curve fitting using experimental test data. In this thesis, the three- and two-parameter Mooney-Rivlin material model is adopted. Derived from Equation (3.46) by setting $M = N = 1$ and $C_{00} = 0$ for tree-parameter model follows as

$$\begin{aligned}\Psi(\bar{I}_1, \bar{I}_2, J) = \frac{1}{d}(J-1)^2 + C_{10}(\bar{I}_1 - 3) \\ + C_{01}(\bar{I}_2 - 3) + C_{11}(\bar{I}_1 - 3)(\bar{I}_2 - 3).\end{aligned} \tag{3.47}$$

The primary objective here is to develop a material model that can be parameterized based on the process parameters, specifically the exposure intensity H_v. It is assumed that the constitutive parameters are the only variables influenced by the process parameters, and they establish a connection between photopolymerization and the final stiffness of the printed materials. Additionally, these coefficients are assumed to be time-independent, thereby not contributing to the dissipation inequality in Equation (3.37). The parametric expression of the energy function in terms of exposure intensity H_v can be formulated as

$$\begin{aligned}\Psi(\bar{I}_1, \bar{I}_2, J; H_v) = \frac{2}{d(H_v)}(J-1)^2 + C_{10}(H_v)(\bar{I}_1 - 3) \\ + C_{01}(H_v)(\bar{I}_2 - 3) + C_{11}(H_v)(\bar{I}_1 - 3)(\bar{I}_2 - 3)\,.\end{aligned} \tag{3.48}$$

Here, the four material coefficients, d, C_{10}, C_{01}, and C_{11}, become functions of H_v. To achieve this, the constitutive parameters fitted for different discrete values of H_v will be interpolated. Furthermore, these Mooney-Rivlin coefficients can be converted into physical material parameters, also called Lamé parameters, specifically the bulk modulus κ and the shear modulus μ as

$$\begin{aligned}\kappa &= \frac{2}{d} \\ \mu &= 2(C_{01} + C_{10})\,.\end{aligned} \tag{3.49}$$

In the first step of establishing the constitutive model, the degree of compressibility of the material must be determined by measuring the incompressibility variable d. Once the material is confirmed to be incompressible, as will be demonstrated in the results chapter, the constitutive model can be employed in its incompressible formulation.

The first Piola-Kirchhoff stress in Equation (3.45) for incompressible material, for which

$J = 1$ holds, can be written as

$$\mathbf{P} = p\,\mathbf{F}^{-T} + \sum_{i=1}^{2} \frac{\partial \Psi}{\partial I_i} \frac{\partial I_i}{\partial \mathbf{F}}. \tag{3.50}$$

where p represents the hydrostatic pressure. The stress state can be calculated for a given strain state using Equation (3.50)

$$\begin{aligned} \mathbf{P}(\mathbf{F}) &= p\,\mathbf{F}^{-T} + 2\frac{\partial \psi}{\partial I_1}\mathbf{F} + 2\frac{\partial \psi}{\partial I_2}\left(I_1\mathbf{F} - \mathbf{F}\mathbf{C}\right) \\ &= p\,\mathbf{F}^{-T} + 2\left(C_{10} + C_{11}(I_2 - 3)\right)\mathbf{F} + 2\left(C_{01} + C_{11}(I_1 - 3)\right)\left(I_1\mathbf{F} - \mathbf{F}\mathbf{C}\right). \end{aligned} \tag{3.51}$$

The unidentified variables in Equation (3.51) are determined by fitting the stress state $\mathbf{P}(\mathbf{F})$ obtained from the model to the stress state acquired from experimental observations under various loading conditions, with known strain states $\mathbf{F}$ and through fitting process explained in Section 2.3. To completely determine the material parameters, multiple experiments involving diverse loading conditions are required [70, 108]. A volumetric compression test is conducted to determine the incompressibility parameter d, whereas uniaxial tension and compression tests are performed to investigate the material's response along Cartesian directions and determine the material parameters C_{mn}.

During a uniaxial tension experiment conducted on an incompressible material with a value of $J = 1$, the principal stretches exhibit the following characteristics

$$\begin{aligned} \lambda_1 &= \lambda \\ \lambda_2 &= \lambda_3 = \lambda^{-1/2}, \end{aligned} \tag{3.52}$$

where λ is the stretch in tension direction. Consequently, the expression for the right Cauchy-Green tensor, denoted as $\mathbf{C}$ in Equation (3.11), can be written as

$$\mathbf{C} = \begin{pmatrix} \lambda^2 & 0 & 0 \\ 0 & \lambda^{-1} & 0 \\ 0 & 0 & \lambda^{-1} \end{pmatrix}. \tag{3.53}$$

The invariants, which are utilized in the determination of the first Piola-Kirchhoff stress, are expressed as

$$I_1 = \lambda^2 + \frac{2}{\lambda}, \qquad I_2 = 2\lambda + \frac{1}{\lambda^2}. \tag{3.54}$$

3.3.2. Visco-hyperelasticity

In this thesis, the 3D-printed polymers, much like the majority of polymers, display rate-dependent behavior. Consequently, it is important to develop constitutive models that accurately

consider this rate-dependent nature of the material. The fundamental characteristic of inelastic material is the existence of non-equilibrium states that undergo changes over time. Two common instances of irreversible phenomena observed in classical mechanics, which govern these non-equilibrium states, are relaxation and creep. Relaxation denotes the gradual return to an equilibrium state following a disturbance. Generally, stress decreases over time at a fixed strain, process commonly known as relaxation. Conversely, during a creeping process, strain increases over time at a constant stress level, see [109, 110] for further information. For an illustration of relaxation processes refer to Figure 3.2 (a). The viscoelastic behavior of a material is characterized by hysteresis, wherein the loading and unloading curves do not coincide, see Figure 3.2 (b). This reveals the irrecoverable energy dissipated when a material is loaded to a point and then unloaded. In the following the relaxation behavior of materials is discussed and the mathematical formulation within finite deformations is derived.

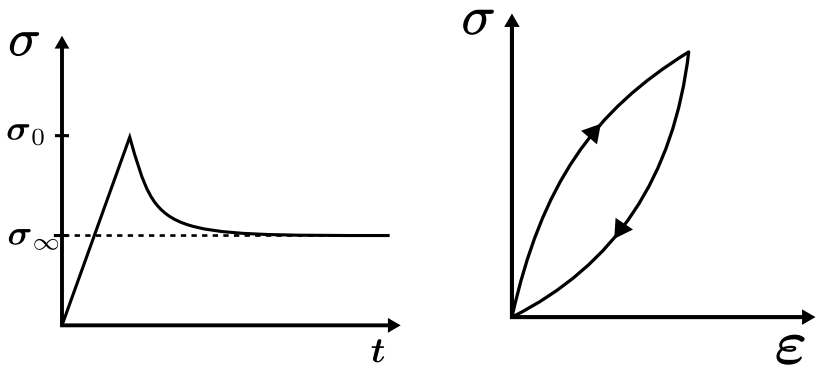

(a) Relaxation **(b)** Hysteresis

Figure 3.2. Schematically illustration of relaxation behavior and hysteresis of a viscoelastic material.

The starting point toward establishing visco-hyperelastic constitutive model is to incorporate an additional tensor-valued internal variable, denoted as $\boldsymbol{\gamma}$, into the formulation of the free energy function for an inelastic process in finite deformations [109, 110]. This internal variable $\boldsymbol{\gamma}$ accounts for the irreversible changes occurring during the inelastic process. Similar to the approach taken in the previous section regarding hyperelasticity, the free energy function can be expressed in terms of the symmetric right Cauchy-Green strain tensor $\mathbf{C} = \mathbf{F}^T\mathbf{F}$ and in the isotropic case by utilizing its invariants in Equation (3.43). Consequently, the expression for the free energy function with a single internal variable, denoted as $\Psi(\mathbf{C}, \boldsymbol{\gamma})$, can be written as follows

$$\Psi(\mathbf{C}, \boldsymbol{\gamma}) = \Psi(I_1, I_2, I_3, \boldsymbol{\gamma})\,. \tag{3.55}$$

As mentioned in hyperelasticity, by formulating the strain energy density function based on these invariants, both objectivity and isotropy can be ensured [108, 109]. Moreover, the

volumetric response of the material can be considered as purely elastic [110]. Therefore, it is advantageous to decompose the strain energy function into two distinct components, following the formulation of hyperelasticity: volumetric and isochoric contributions [74, 109]. Consequently, for nearly incompressible materials, Equation (3.55) can be expressed as

$$\Psi(\bar{I}_1, \bar{I}_2, J, \boldsymbol{\gamma}) = \Psi^{\infty}_{\text{vol}}(J) + \Psi^{\infty}_{\text{iso}}(\bar{I}_1, \bar{I}_2) + \Upsilon^{v}(\bar{I}_1, \bar{I}_2, \boldsymbol{\gamma})\,, \tag{3.56}$$

where $\Psi^{\infty}_{\text{vol}}$ and $\Psi^{\infty}_{\text{iso}}$ represent the elastic volumetric and isochoric terms, respectively, and the viscoelastic contribution Υ^{v} is assumed to be purely distortional.

Similar to hyperelasticity, the first Piola-Kirchhoff stress can be derived from the energy function as shown in Equation (3.45). However, for the energy function $\Psi(\mathbf{C})$ in terms of $\mathbf{C}$, it is advantageous to calculate the symmetrical second Piola-Kirchhoff stress as

$$\mathbf{S} = 2\frac{\partial \Psi(\mathbf{C})}{\partial \mathbf{C}}\,, \tag{3.57}$$

which is related to the first Piola-Kirchhoff stress and Cauchy stress through

$$\mathbf{S} = \mathbf{F}^{-1}\mathbf{P} = J\mathbf{F}^{-1}\boldsymbol{\sigma}\mathbf{F}^{-T}\,. \tag{3.58}$$

The decomposition of the second Piola-Kirchhoff stress is obtained from substituting Equation (3.56) in Equation (3.57) as

$$\begin{gathered} \mathbf{S} = 2\frac{\partial \Psi}{\partial \mathbf{C}} = \mathbf{S}^{\infty}_{\text{vol}} + \mathbf{S}^{\infty}_{\text{iso}} + \mathbf{Q} \qquad \text{with} \\ \mathbf{S}^{\infty}_{\text{vol}} = 2\frac{\partial \Psi^{\infty}_{\text{vol}}(J)}{\partial \mathbf{C}}\,, \qquad \mathbf{S}^{\infty}_{\text{iso}} = 2\frac{\partial \Psi^{\infty}_{\text{iso}}(\bar{I}_1, \bar{I}_2)}{\partial \mathbf{C}}\,, \qquad \mathbf{Q} = 2\frac{\partial \Upsilon^{v}(\bar{I}_1, \bar{I}_2, \boldsymbol{\gamma})}{\partial \mathbf{C}}\,, \end{gathered} \tag{3.59}$$

where $\mathbf{S}^{\infty}_{\text{vol}}$ and $\mathbf{S}^{\infty}_{\text{iso}}$ are volumetric and isochoric parts of the second Piola-Kirchhoff stress, respectively, and $\mathbf{Q}$ represents the non-equilibrium stress contribution of the viscoelastic part. Following [109], $\mathbf{Q}$ is furthermore assumed to be conjugate to $\boldsymbol{\gamma}$, so that

$$\mathbf{Q} = -2\frac{\partial \Psi}{\partial \boldsymbol{\gamma}} = -2\frac{\partial \Upsilon^{v}(\bar{I}_1, \bar{I}_2, \boldsymbol{\gamma})}{\partial \boldsymbol{\gamma}}\,. \tag{3.60}$$

Thus, the model can be formulated by using $\mathbf{Q}$ as a stress-like internal variable, for which the following complementary equation of evolution is employed

$$\dot{\mathbf{Q}} + \frac{\mathbf{Q}}{\tau} = \dot{\mathbf{S}}^{v}_{\text{iso}}\,. \tag{3.61}$$

Here, τ is the relaxation time of the viscous element and $\mathbf{S}^{v}_{\text{iso}}$ is the isochoric second Piola-Kirchhoff stress corresponding to the strain energy $\Psi^{v}_{\text{iso}}(\bar{I}_1, \bar{I}_2)$ related to the relaxation process

of the system, with

$$\mathbf{S}^{v}_{\text{iso}} = 2\frac{\partial \Psi^{v}_{\text{iso}}(\bar{I}_1, \bar{I}_2)}{\partial \mathbf{C}}. \tag{3.62}$$

In this way, an explicit definition of Υ^v in Equation (3.56) is not required. A detailed derivation of non-equilibrium stress contribution and its evaluation can be found in [71, 109, 111, 112].

For the specific problem under consideration, the determination of the required viscoelastic elements for modeling the photocured polymer, as depicted in Figure 2.1 (c) and Figure 2.1 (d), is based on previous research works [31, 51, 113, 114]. The composition of the molecular network comprises fully crosslinked solid sections, partially cured portions, and uncured regions. The equilibrium response of the printed polymer is assumed to be represented by the fully crosslinked part, where the monomers are connected through crosslinkers from both sides. This part demonstrates the system's equilibrium response. However, certain areas of the printed material may remain uncured or partially cured, depending on the exposure intensity H_v, and exhibit distinct behavior compared to the cured parts. These partially cured or uncured regions can be realized as monomers linked to the molecular network from one side or as free from both sides [31, 51]. In this study, the viscous component of the printed material is considered to consist of monomers at the microscopic level with free sides. Consequently, an appropriate expression of material behavior can be achieved through a visco-hyperelastic constitutive model, which encompasses an elastic element parallel to one viscoelastic element to capture the inelastic response of the material. The utilization of this formulation offers simplicity and reduces the number of inelastic elements, thus facilitating its numerical implementation. It should be noted, however, that extending the model to incorporate multiple inelastic branches can be accomplished in a straight forward manner.

Now, the explicit definition of the energy function Ψ should be elaborated. As discussed previously, the response of a material to loading within the context of finite inelasticity is governed by the particular formulation of the energy function Ψ, which is expressed in terms of the tensor $\mathbf{C}$ (or its invariants) and the tensor $\boldsymbol{\gamma}$ (or $\mathbf{Q}$) in the constitutive theory. Consequently, the choice of the constitutive model depends on its intended application and the material's behavior in experimental tests. In accordance with previous section, the Mooney-Rivlin model is selected to describe the hyperelastic constitutive behavior of grayscale 3D printed polymer materials in Equation (3.56), as it is a well-established model for elastomers subjected to large strains [68, 73, 74]. Through the analysis of various formulations in this study, it has been determined that the experimental characterization data of the material at hand can be accurately fitted by this particular material model. However, it should be noted that different materials may require the selection of other more appropriate material models [57].

The Mooney-Rivlin material model with two parameters (or Mooney model [115]) for a

(near) incompressible, visco-hyperelastic material is given [73, 74] as

$$\begin{aligned}\Psi^{\infty}_{\text{vol}}(J) &= \frac{1}{d}(J-1)^2\,,\\ \Psi^{\infty}_{\text{iso}}(\bar{I}_1,\bar{I}_2) &= C^{\infty}_{10}(\bar{I}_1-3)+C^{\infty}_{01}(\bar{I}_2-3)\,,\\ \Psi^{v}_{\text{iso}}(\bar{I}_1,\bar{I}_2) &= C^{v}_{10}(\bar{I}_1-3)+C^{v}_{01}(\bar{I}_2-3)\,,\end{aligned} \tag{3.63}$$

where d is the incompressibility parameter and $C^{\infty}_{10}, C^{\infty}_{01}, C^{v}_{01}$ and C^{v}_{10} represent the further material parameters, which have to be determined through curve fitting of experimental test data. As mentioned previously, the objective of constitutive modeling here is to parameterize the material model as a function of exposure intensity H_v, hence Equation (3.63) can be rewritten as

$$\begin{aligned}\Psi^{\infty}_{\text{vol}}(J;H_v) &= \frac{1}{d(H_v)}(J-1)^2\,,\\ \Psi^{\infty}_{\text{iso}}(\bar{I}_1,\bar{I}_2;H_v) &= C^{\infty}_{10}(H_v)\,(\bar{I}_1-3)+C^{\infty}_{01}(H_v)\,(\bar{I}_2-3)\,,\\ \Psi^{v}_{\text{iso}}(\bar{I}_1,\bar{I}_2;H_v) &= C^{v}_{10}(H_v)\,(\bar{I}_1-3)+C^{v}_{01}\,(H_v)\,(\bar{I}_2-3)\,,\end{aligned} \tag{3.64}$$

where the terms $d(H_v)$, $C^{\infty}_{10}(H_v)$, $C^{\infty}_{01}(H_v)$, $C^{v}_{10}(H_v)$, and $C^{v}_{01}(H_v)$ represent functions of exposure intensity H_v that characterize the Mooney-Rivlin material parameters. Inspired by [31, 51], it is proposed that these material parameters are dependent on their maximum values, which are determined by the maximum exposure intensity denoted as $H_{v,max}$ represented by Φ_{max} in Equation (2.3). The next chapter will provide a detailed discussion on how higher mechanical stiffness can be achieved and its implications.

The second Piola-Kirchhoff stress is determined by substituting Equation (3.64) into Equation (3.59) and using the evolution equation (3.61) for $\mathbf{Q}$ as

$$\begin{aligned}\mathbf{S}^{\infty}_{\text{vol}} &= J\frac{\partial\Psi^{\infty}_{\text{vol}}(\bar{I}_1,\bar{I}_2,J;H_v)}{\partial J}\mathbf{C}^{-1} = \frac{2}{d(H_v)}J(J-1)\mathbf{C}^{-1}\,,\\ \mathbf{S}^{\infty/v}_{\text{iso}} &= J^{-2/3}(\mathbb{I}-\frac{1}{3}\mathbf{C}^{-1}\otimes\mathbf{C}):\bar{\mathbf{S}}^{\infty/v}_{\text{iso}}\,,\end{aligned} \tag{3.65}$$

with

$$\begin{aligned}\bar{\mathbf{S}}^{\infty}_{\text{iso}} &= 2\frac{\partial\Psi^{\infty}_{\text{iso}}(\bar{I}_1,\bar{I}_2,J;H_v)}{\partial\bar{I}_1}\mathbf{I}+2\frac{\partial\Psi^{\infty}_{\text{iso}}(\bar{I}_1,\bar{I}_2,J;H_v)}{\partial\bar{I}_2}\left(\bar{I}_1\mathbf{I}-\bar{\mathbf{C}}\right)\\ &= 2C^{\infty}_{10}(H_v)\,\mathbf{I}+2C^{\infty}_{01}(H_v)\,(\bar{I}_1\mathbf{I}-\bar{\mathbf{C}})\,,\\ \bar{\mathbf{S}}^{v}_{\text{iso}} &= 2\frac{\partial\Psi^{v}_{\text{iso}}(\bar{I}_1,\bar{I}_2;H_v)}{\partial\bar{I}_1}\mathbf{I}+2\frac{\partial\Psi^{v}_{\text{iso}}(\bar{I}_1,\bar{I}_2;H_v)}{\partial\bar{I}_2}\left(\bar{I}_1\mathbf{I}-\bar{\mathbf{C}}\right)\\ &= 2C^{v}_{10}(H_v)\,\mathbf{I}+2C^{v}_{01}(H_v)\,(\bar{I}_1\mathbf{I}-\bar{\mathbf{C}})\,,\end{aligned} \tag{3.66}$$

where $\mathbb{I}=\delta_{ik}\delta_{jl}$ is the fourth order identity tensor, and the operator $\otimes$ stands for the dyadic product.

Finally, the non-zero tensile component of the first Piola-Kirchhoff stress, comparable to

the experimental results where the measured force is divided by the area in the undeformed configuration, is derived by utilizing the symmetric second Piola-Kirchhoff stress. The equation provides this component is given as

$$P_{11} = \lambda S_{11} \,. \tag{3.67}$$

3.3.3. Elasto-Visco-Plasticity

This section focuses on developing a comprehensive constitutive model that can accurately capture the material behavior within purely elasto-plastic regions, taking into account the rate-dependent behavior of the material, including viscoelasticity. The finite element simulations in the majority of this dissertation are carried out using Ansys. Therefore, the following section will concentrate on constitutive modeling based on the principles of Ansys theory reference [116], which was utilized during the course of this thesis. The presented constitutive model can be used in a pure elastic regime, where the stress in the material is below the yield point, and the strain rate is small enough for viscoelastic effects to be disregarded. Additionally, the viscoelastic component of the constitutive model can account for the rate-dependent behavior of the material below the yield point. Finally, incorporating the plastic part of the model enables the description of the material's behavior beyond the yield point.

Kinematics

Inspired by the model of single crystal for metals' plasticity, an alternative approach to the conventional additive splitting of strain rates into elastic and plastic components [104, 110] is proposed. This alternative approach employs a multiplicative decomposition of the deformation gradient, as expressed by the equation

$$\mathbf{F} = \mathbf{F}^e \mathbf{F}^p \,. \tag{3.68}$$

Here, an additional intermediate configuration is introduced, complementing the initial and spatial configurations, as depicted in Figure 3.3. This intermediate configuration, referred to as the incompatible configuration, is assumed to be free of any internal stresses. In the case of axisymmetric deformations, the multiplicative decomposition can be described using principal stretches as follows

$$\lambda_i = \lambda_i^e \lambda_i^p \,. \tag{3.69}$$

With the inclusion of logarithmic strains, which correspond to the eigenvalues of the Hencky tensor, as referenced in Equation (3.9), the following relationship emerges

$$\varepsilon_i = \ln \lambda_i \,. \tag{3.70}$$

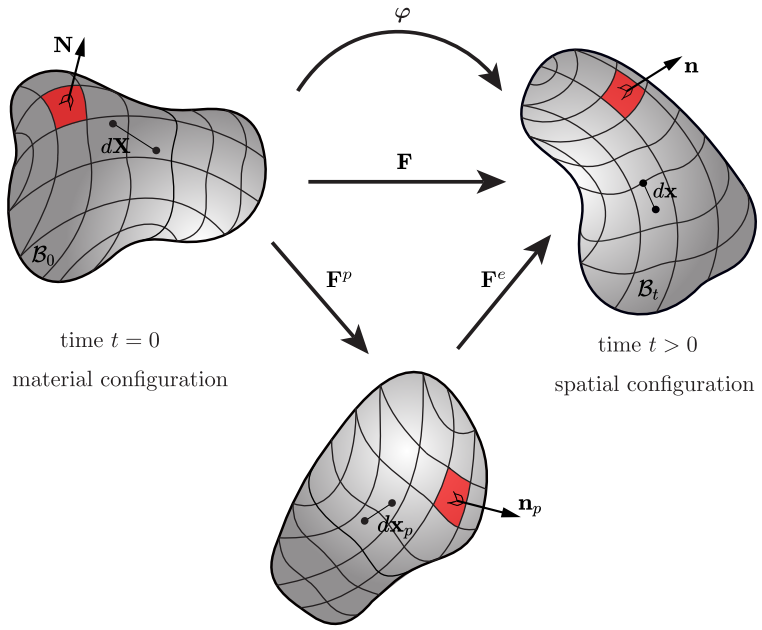

Figure 3.3. Kinematics of plasticity with multiplicative decomposition of deformation gradient into elastic $\mathbf{F}^e$ and plastic $\mathbf{F}^p$ parts. The plastic part $\mathbf{F}^p$ maps the body $\mathcal{B}_0$ into an intermediate configuration, which is in general incompatible, and the elastic part of the deformation gradient maps the body $\mathcal{B}_p$ into a stressed spatial configuration $\mathcal{B}_t$. Similar representation is given in [102].

One can rephrase the multiplicative decomposition discussed in Equation (3.69) as an additive decomposition

$$\varepsilon = \varepsilon^e + \varepsilon^p \,. \tag{3.71}$$

where ε is the Hencky strain. More detailed information about phenomenological plasticity models based on the notion of an intermediate stress-free configuration can be found in [104, 110, 117].

Constitutive model

In the elastic-plastic regime, the material reaches a critical point beyond which it can no longer sustain additional loads and thus experiences plastic deformation. A one-dimensional rheological model is depicted in Figure 3.4, where a linear elastic spring is in parallel with a Maxwell viscoelastic element, incorporating a frictional component, which represents an elasto-visco-plastic material model. In this system, when a constant strain rate is applied, the stress increases until it reaches certain values known as the yield stress $\sigma_y = Y_0$. At this point, the elastic element is no longer able to sustain additional loads, resulting in the occurrence of plastic irreversible strain within the frictional element. In addition, the viscoelastic behavior of

the material before the yielding point can be described using the rheological model in Figure 3.4. It is assumed that the model possesses standardized dimensions of unit area and unit length, enabling the interpretation of stresses as forces and strains as extensions, respectively [109, 110, 118]. A set of springs, which respond elastic, is assumed to model the solid behavior. The stiffnesses of the free spring on one end and the spring for the Maxwell element are determined by positive Young's modulus, denoted as E_∞ and E_i, respectively, where i takes values from 1 to n and represents the number of Maxwell elements. The flow behavior is represented by a Newtonian viscous fluid that acts like a dashpot. The viscosity of the fluid in the ith-Maxwell element is adequately specified by a positive material coefficients denoted as η_i. All these parameters, based on physics, are confirmed to be positive.

Empirical evidence often justifies the assumption of incompressible plastic deformations [71, 104]. In such cases, the volumetric behavior of the material is considered purely elastic, and consequently, the bulk modulus κ does not contribute to the plastic behavior of the material [109]. Hence it is appropriate to use the isochoric strain measure. Regarding the reological model in Figure 3.4, the elastic strain can be determined from Equation (3.71) as

$$\boldsymbol{\varepsilon}^e = \boldsymbol{\varepsilon} - \boldsymbol{\varepsilon}^p \,. \tag{3.72}$$

By incorporating the plastic behavior in the material, the assumption of a Helmholtz free energy potential can be written as

$$\Psi(\boldsymbol{\varepsilon}, \boldsymbol{\varepsilon}^p, \gamma_1, \ldots, \gamma_n, \alpha) = \Psi^e(\boldsymbol{\varepsilon}^e) + \sum_{i=1}^{n} \Psi_i^v(\boldsymbol{\varepsilon}, \gamma_i) + \Psi^h(\alpha) \,, \tag{3.73}$$

which is defined in terms of the total strain $\boldsymbol{\varepsilon}$, as well as internal variables denoting the plastic strain $\boldsymbol{\varepsilon}^p$, the viscous strains $\boldsymbol{\gamma}_i$ in a generalized Maxwell rheological model with n branches, and the isotropic hardening variable α. Using a rate-independent von Mises plasticity model, the plastic strains and the hardening variable α are governed by the associated flow rules

$$\dot{\boldsymbol{\varepsilon}}^p = \lambda^p \frac{\partial \Phi}{\partial \boldsymbol{\sigma}} \,, \quad \dot{\alpha} = \lambda^p \frac{\partial \Phi}{\partial \beta} \,, \tag{3.74}$$

which depend on the yield function

$$\Phi(\boldsymbol{\sigma}, \beta) = \|\boldsymbol{\sigma}\| - \sqrt{\frac{2}{3}}(\sigma_y - \beta), \tag{3.75}$$

where $\beta = -H\alpha$ with isotropic hardening modulus H. The plastic multiplier λ^p describes the amount of plastic strain in the system and can be determined by the following Kuhn-Tucker conditions

$$\lambda^p \geq 0, \qquad \lambda^p \Phi = 0, \qquad \Phi \leq 0. \tag{3.76}$$

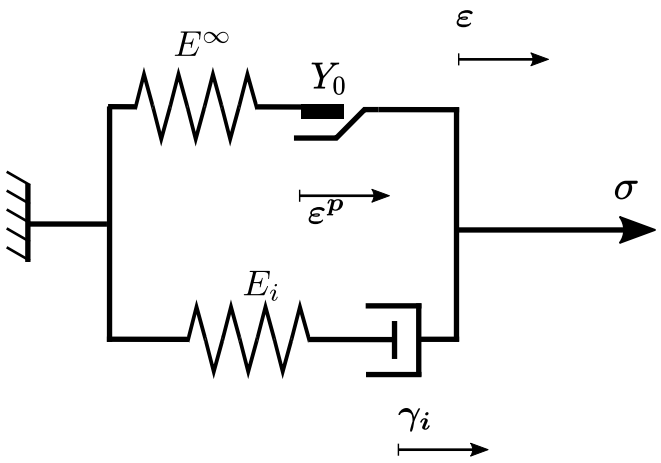

Figure 3.4. One-dimensional rheological model representing elasto-visco-plastic material behavior.

The Cauchy stress tensor $\boldsymbol{\sigma}$ can be expressed within a generalized Maxwell rheological model comprising n viscoelastic branches for elasto–visco–plastic system shown in Figure 3.4 as

$$\boldsymbol{\sigma} = p\,\mathbf{I} + \mathbb{C}^e : (\boldsymbol{\varepsilon}^{\text{iso}} - \boldsymbol{\varepsilon}^p) + \sum_{i=1}^{N} \mathbb{C}_i^v : (\boldsymbol{\varepsilon}^{\text{iso}} - \gamma_i)\,, \tag{3.77}$$

where $\mathbb{C}^e$ and $\mathbb{C}^v$ are fourth-order elastic and viscoelastic stiffness tensors, respectively. In consideration of the observation that only the isochoric component of an incompressible material contributes to viscoelastic deformation [104, 110], the material's behavior can be described using (isochoric) fourth-order stiffness tensors as

$$\mathbb{C}^e = 2\mu^e\,\mathbb{I}, \qquad \mathbb{C}_i^v = 2\mu_i^v\,\mathbb{I} = \beta_i\,\mathbb{C}^e, \tag{3.78}$$

where μ^e represents the elastic shear modulus, $\mu_i^v = \beta_i \mu^e$ corresponds to the viscoelastic shear modulus, and $\mathbb{I}$ denotes the fourth-order identity tensor. The total shear modulus, denoted as μ, can be defined as

$$\mu = \mu^e + \sum_{i=1}^{N} \mu_i^v\,. \tag{3.79}$$

It worth noting that in case of finite plastic deformation but small elastic strains a linear energy function can be used [104, 116, 119]. In Equation (3.77) the isochoric strain component $\boldsymbol{\varepsilon}^{\text{iso}}$ is defined as

$$\boldsymbol{\varepsilon}^{\text{iso}} = \boldsymbol{\varepsilon} - \frac{1}{3}\,\text{trace}(\boldsymbol{\varepsilon})\mathbf{I} \tag{3.80}$$

The total strain in Maxwell elements in the rheological model shown in Figure 3.4 is equal to the strain in the elasto-plastic element. Hence, the strain in the spring in ith-Maxwell element is

$$\varepsilon_i = \varepsilon - \gamma_i \,. \tag{3.81}$$

The complementary equation of evolution of the viscous strains $\boldsymbol{\gamma}_i^v$ is governed by the following linear equations

$$\dot{\boldsymbol{\gamma}}_i = \frac{1}{\tau_i}(\boldsymbol{\varepsilon} - \boldsymbol{\gamma}_i), \quad \text{with} \quad i = 1, 2, ..., n \,. \tag{3.82}$$

The material parameters Young's modulus and Poisson's ratio can be written in terms of Lamé parameters κ and μ using the Lamé parameter conversion formulas

$$\begin{aligned} E &= \frac{9\kappa\mu}{3\kappa + \mu}, \\ \nu &= \frac{3\kappa - 2\mu}{6\kappa + 2\mu} \,. \end{aligned} \tag{3.83}$$

Furthermore, in addition to the investigation of the exposure intensity of the Mooney-Rivlin coefficients, the exposure intensity of these physical material parameters will also be explored in this thesis. Further information regarding the theory of elasticity can be found in references [118, 120–123].

4. Influence of Process Parameters on Mechanical Properties

In this section, the influence of process parameters on mechanical properties is studied. The main process parameters, as mentioned previously, are grayscale values, exposure time, and layer thickness. The grayscale value regulates the light in each pixel on the LCD, the exposure time changes the degree of monomer conversion throughout the entire layer, and the layer thickness changes the mechanical properties at intersections horizontal to the print direction. Changes in the process parameters result in variations in the degree of monomer conversion, thereby impacting the elastic, visco-hyperelastic, and plastic behavior of the printed material.

In Section 4.1, a thorough investigation is conducted to analyze the impact of grayscale on the hyperelastic constitutive model, followed by the validation of the parametric constitutive model through experimental cases. Furthermore, Section 4.2 explores the study of the influence of exposure time and grayscale value on the visco-hyperelastic constitutive model. In Section 4.3, a detailed examination is carried out to assess the influence of the unified process parameter, exposure intensity, on the elasto-visco-plastic constitutive model. Lastly, the acquired findings are utilized to optimize the process specifically for a lattice structure in Section 4.4.

4.1. Rate Independent Parametric Constitutive Modeling

4.1.1. Hyperelastic Constitutive Parameters

In real-world applications, different scenarios exist in which exposure intensity in Equation (2.2) can be modified and utilized. While determining the optimal values for exposure time and layer thickness, grayscale remains the only parameter that can customize mechanical properties at each point within the material. This section focuses on a case in which grayscale is the sole parameter influencing the degree of monomer conversion in the resin. Additionally, this section demonstrates how a hyperelastic material model can be employed to describe the material's behavior under one-time loading and constant strain rate.

When exposure time and layer thickness remain constant, the only process parameter considered as a design parameter is light intensity. Therefore, the exposure intensity can be

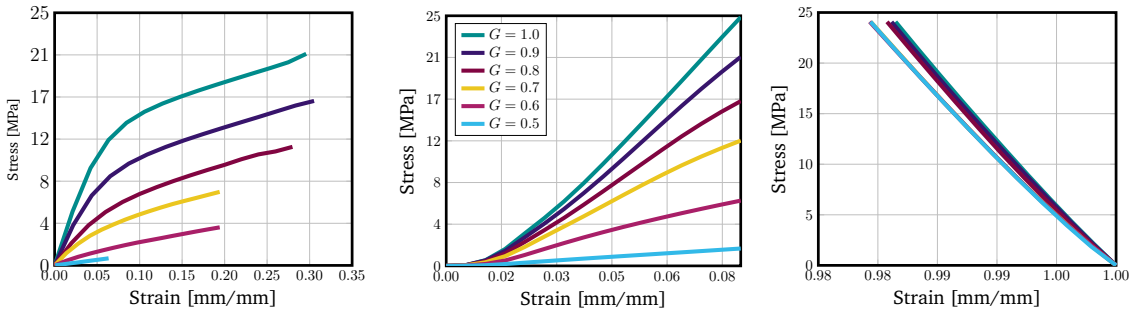

(a) Uniaxial tension **(b)** Uniaxial compression **(c)** Volumetric compression

Figure 4.1. The stress-strain curves obtained from (a) uniaxial tension, and (b) uniaxial compression, and (c) volumetric compression experimental tests for variation of grayscales ranging from $G = 1.0$ to $G = 0.5$. Similar results are shown in [99].

expressed as

$$H_v(G,t) = I_e(G) = I_e^{\max} \cdot G^2 \,. \tag{4.1}$$

As it was mentioned previously, the light intensity can be controlled in each point of material by changing the grayscale value of the mask. This method facilitates fabrication of graded structure by controlling degree of monomer conversion in resin. To achieve this goal, the material response must first be determined for various values of exposure intensities using Equation 4.1. As mentioned earlier, the light intensity may vary for different types of 3D printers. Therefore, the relationship between material properties and exposure intensity is expressed in terms of grayscale value G. To characterize the mechanical response of grayscale 3D printed materials under different deformation states, samples are printed with $G = 1.0, G = 0.9, G = 0.8, G = 0.7, G = 0.6$, and $G = 0.5$ and tests were conducted to measure volumetric compression, uniaxial tension, and uniaxial compression. Here the exposure time is $t = 10$ s, and the thickness is $h = 0.05$ mm, resulting in exposure intensity values from $H_v = 1.1$ to $H_v = 0.28$. The resulting stress-strain curves are presented in Figure 4.1 (a) for uniaxial tension, Figure 4.1 (b) for uniaxial compression, and Figure 4.1 (c) for volumetric compression. The uniaxial tension test presented in Figure 4.1 (a) reveals that the materials demonstrate a nonlinear behavior with noticeable softening at higher strains. Additionally, there is a correlation between the grayscale value and stiffness, where an increase in grayscale value generally corresponds to a higher stiffness and consequently higher stress levels. Moreover, as the grayscale value increases, both failure strains and stresses also increase. Similarly, the volumetric compression responses, as illustrated in Figure 4.1 (c), show a close similarity due to the nearly incompressible characteristics of the materials.

In order to establish a parametric constitutive model, the Mooney-Rivlin coefficients in Equation (3.48) have to be determined as a function of grayscale values, namely $d, C_{ij} = f(G)$. The determination of Mooney-Rivlin coefficients is performed by fitting the numerical stresses

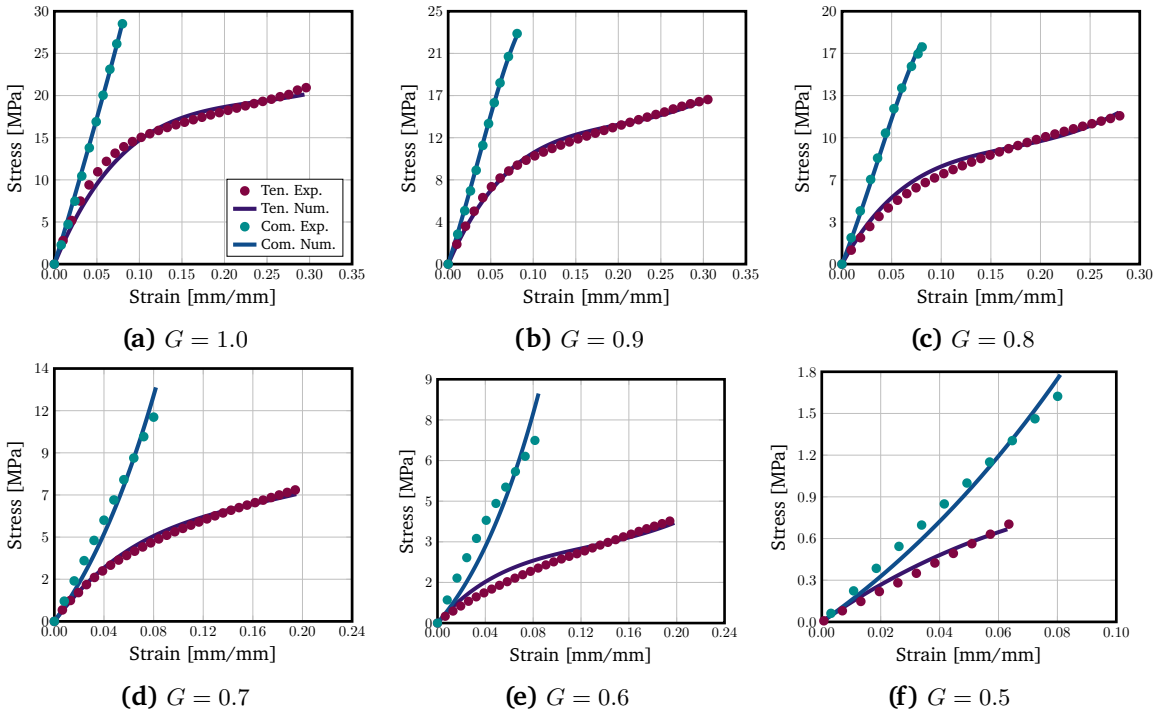

(a) $G = 1.0$ **(b)** $G = 0.9$ **(c)** $G = 0.8$

(d) $G = 0.7$ **(e)** $G = 0.6$ **(f)** $G = 0.5$

Figure 4.2. The stress-strain curves obtained from experimental tests were compared to the hyperelastic material model that was fitted, specifically for uniaxial tension and uniaxial compression tests conducted on grayscales ranging from $G = 1.0$ to $G = 0.5$. Similar results are shown in [99].

obtained from the material model Equation (3.51) to the experimental averages of the stress-strain curves for each grayscale G. This fitting process utilizes a least-squares optimization technique for (nearly) incompressible hyperelastic material models, as described in Section 2.3. First the volumetric compression test data are used to determine the incompressibility parameter d. Then, the remaining parameters C_{10}, C_{01}, C_{11} are determined by fitting the numerical stress to the uniaxial tension and compression tests. Figure 4.2 shows the results of the curve fitting process, revealing a significant alignment between the experimental average curves for uniaxial tension and compression and the Mooney-Rivlin models across all grayscales G. The constitutive parameters d, C_{01}, C_{10}, and C_{11} obtained from the fitting process are presented in Figure 4.3 and detailed in Table 4.1.

As it can be seen in Figure 4.3, there is a non-linear relationship between material parameters and grayscale values G. The parameters d and C_{01} exhibit a positive monotonic increase with G, while C_{10} displays a negative trend, resulting in an increase in magnitude as G decreases. Regarding C_{11}, which also shows a positive value, the trend is less evident but generally shows an increasing pattern with G. However, despite this behavior, these parameters can be reasonably approximated based on linear or quadratic fits utilizing the experimentally obtained data points for various grayscale values G.

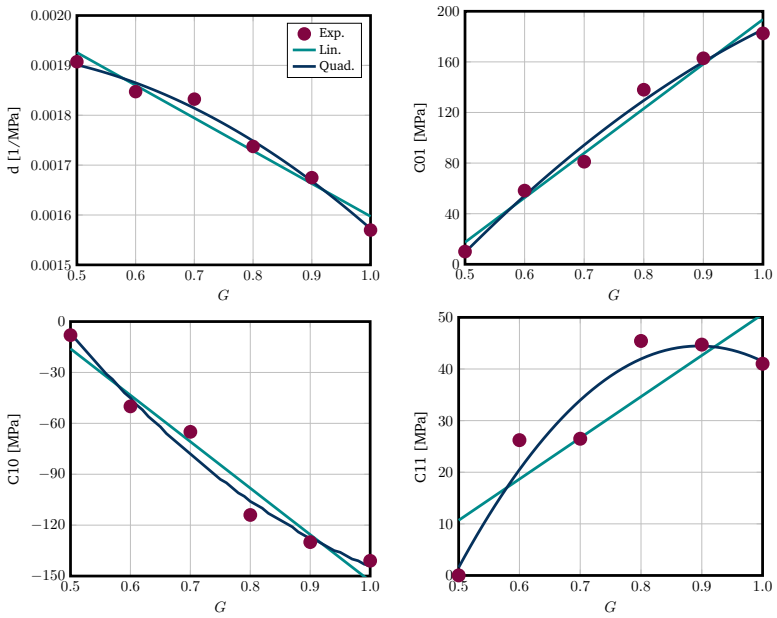

Figure 4.3. The Mooney-Rivlin coefficients $d, C_{01}, C_{10}, C_{11}$ were obtained through curve fitting of the experimental results corresponding to each grayscale. Linear and quadratic approximations were employed to parameterize the grayscales between the experimental data points. Similar results are shown in [99].

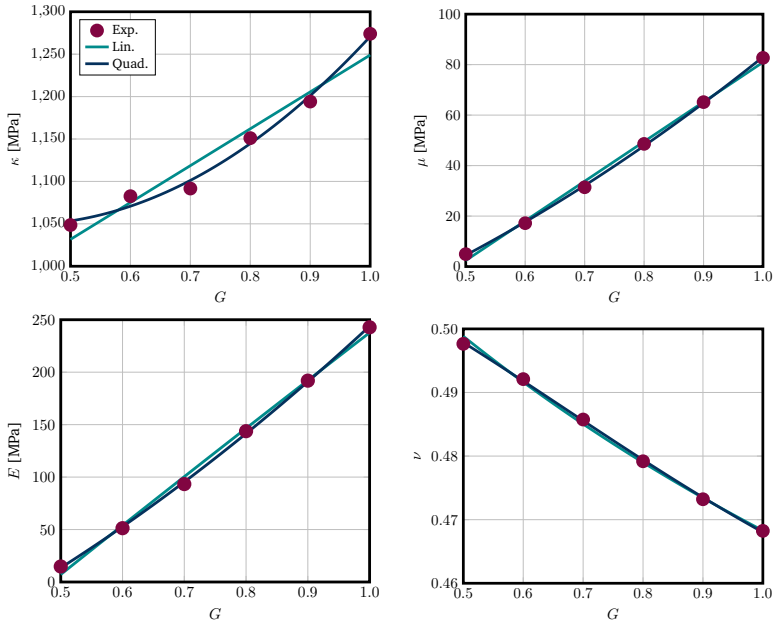

Figure 4.4. The physical material parameters, namely the bulk modulus κ, shear modulus μ, Young's modulus E, and Poisson's ratio ν, were derived by curve fitting the experimental results for each grayscale. In order to capture the variations within the grayscales between the experimental data points, linear and quadratic approximations were employed. Similar results are shown in [99].

G	d [1/MPa]	C_{10}	C_{01}	C_{11}	κ	μ	E	ν [·]
1.0	$1.57 \cdot 10^{-3}$	-141.1	182.5	41.02	1274	82.68	242.8	0.4682
0.9	$1.67 \cdot 10^{-3}$	-130.2	162.8	44.72	1194	65.14	191.9	0.4732
0.8	$1.74 \cdot 10^{-3}$	-113.8	137.9	45.43	1151	48.60	143.8	0.4791
0.7	$1.83 \cdot 10^{-3}$	-65.29	81.08	26.49	1091	31.41	93.34	0.4857
0.6	$1.85 \cdot 10^{-3}$	-50.71	58.25	26.22	1082	17.19	51.30	0.4921
0.5	$1.91 \cdot 10^{-3}$	-7.587	10.07	0.014	1048	4.936	14.79	0.4976

Table 4.1. The obtained Mooney-Rivlin coefficients and physical material parameters (all measured in MPa, except for d and ν) were derived through the process of curve fitting applied to the experimental results for each grayscale.

The physical material parameters, including Young's modulus E, bulk modulus κ, shear modulus μ, and Poisson's ratio ν, which are derived from the provided relations in Equation (3.83) are shown in Figure 4.4 and are also presented in Table 4.1. Although the Mooney-Rivlin material model parameters, namely $d, C_{01}, C_{10}, C_{11}$, exhibit distinct behavior, the Lamé parameters show a more consistent trend. Specifically, Young's modulus, shear modulus, and bulk modulus demonstrate almost linear growth as grayscale ranges from $G = 0.5$ to $G = 1.0$, while Poisson's ratio decreases with increasing G. The relationship between these Lamé parameters and G is effectively captured by fitting linear and quadratic approximations, as demonstrated in Figure 4.4.

The increase in stiffness with higher grayscale values can be attributed to the increased cross-linking density. Consequently, this contributes to the observation of elevated failure strains and stresses during the uniaxial tension tests shown in Figure 4.1 (a). Furthermore, lower cross-linking density implies a more liquid state of the material, which explains the convergence of the Poisson's ratio toward 0.5 as G decreases. It has to be noticed that for $G < 0.5$, the cross-linking density is significantly low, leading to the material remaining in a liquid state.

4.1.2. Verification and Validation of the Parametric Constitutive Model

A finite element method can incorporate the parametric material model along with its coefficients and parameters, obtained in the previous section, to predict and analyze the behavior of printed structures at different grayscale values under arbitrary loading conditions. The grayscale printing technique offers a significant advantage by enabling the tailoring of material properties throughout a structure through arbitrary variation and grading of grayscale values. Hence, the Mooney-Rivlin coefficients obtained for different grayscale values are currently parameterized using linear and quadratic approximations, as depicted in Figure 4.3. The

computation of the Lamé parameters from the interpolated constitutive parameters displays a consistent trend, as illustrated in Figure 4.4. While there are various possible interpolations or approximations, the behavior of the Lamé parameters is not highly sensitive to these changes, and the combinations of coefficients result in similar overall constitutive responses of the material. Therefore, for the remainder of this chapter, the quadratic parametrization in terms of G is employed. For instance, the curve for $G = 0.95$ lies between the curves for $G = 1.0$ and $G = 0.9$.

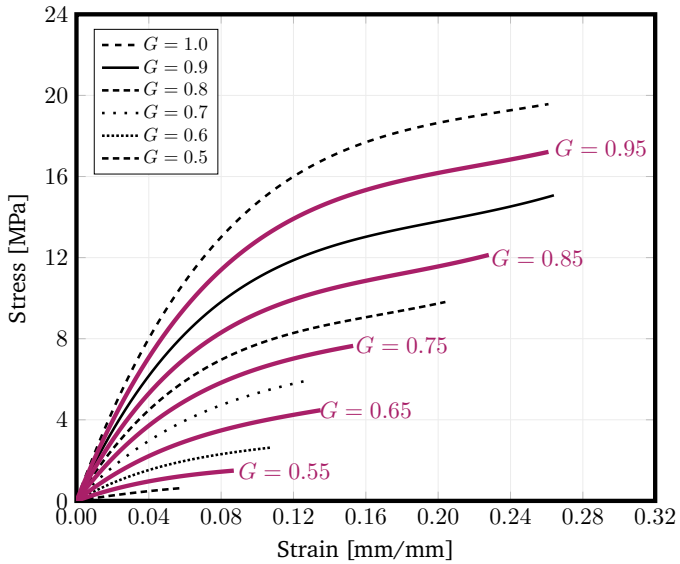

Figure 4.5. The stress-strain curves acquired through experimental fitting for different grayscale values, $G = 1.0, G = 0.9, G = 0.8, G = 0.7, G = 0.6$, and $G = 0.5$, were compared with the interpolated models representing $G = 0.95, G = 0.85, G = 0.75$, and $G = 0.65$. Similar curves are plotted in [99].

Now, the verification of the constitutive model is desired to ensure that the interpolated Mooney-Rivlin coefficients produce reasonable stress–strain curves for any $0.5 \leq G \leq 1.0$. In other words, it needs to be determined whether the parametric hyperelastic constitutive model can be applied to arbitrary grayscale values as they may appear in functionally graded objects. Thus, a comparison is made between the stress-strain curves obtained for uniaxial tension. The curves are derived for the experimentally fitted and validated grayscale values of $G = 1.0, G = 0.9, G = 0.8, G = 0.7, G = 0.6$, and $G = 0.5$, which were utilized to calibrate the constitutive models. Additionally, the arbitrary values of $G = 0.95, G = 0.85, G = 0.75$, and $G = 0.65$ are considered, for which the curves are generated by interpolating the coefficients for the given G (as depicted in Figure 4.3) and subsequently numerically evaluating the Mooney-Rivlin model using Equation (3.51). It can be observed from Figure 4.5 that the stress-strain curves for the interpolated grayscales assume reasonable values, with each curve lay between the range of the calibrated models.

To validate the parametric hyperelastic constitutive model for grayscale MSLA-printed mate-

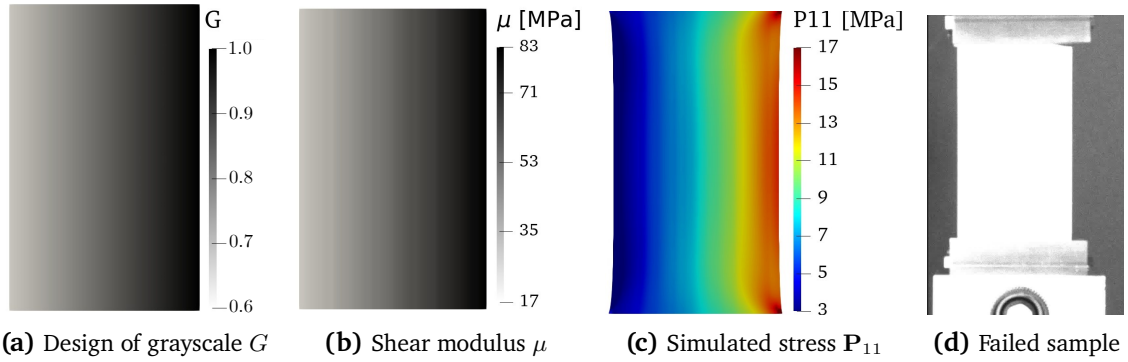

(a) Design of grayscale G **(b)** Shear modulus μ **(c)** Simulated stress $\mathbf{P}_{11}$ **(d)** Failed sample

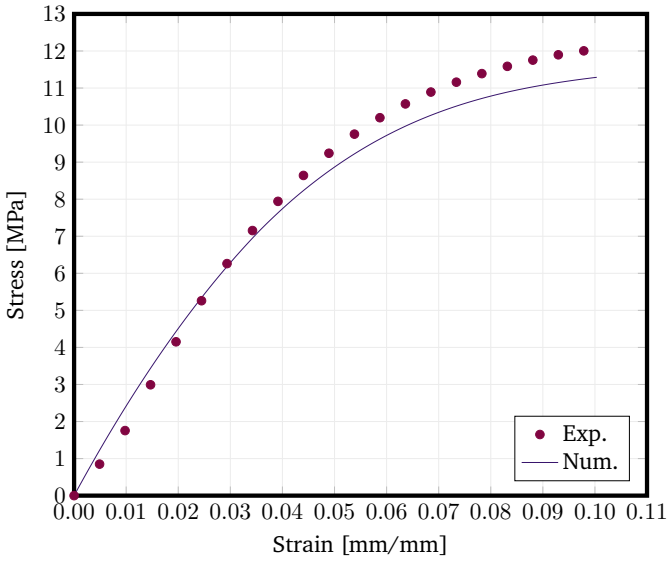

(e) Stress–Strain curves: Experimental vs. Simulation

Figure 4.6. A rectangular structure with a gradient in grayscale, ranging linearly from $G = 0.6$ to $G = 1.0$, is considered. Additionally, the material properties vary orthogonally to the direction of tension. This configuration is illustrated in (a) and (b). The simulated distribution of stress and deformation is depicted in (c). The shape of the structure after failure in the experimental setup is presented in (d). Finally, a comparison between the experimental and numerical stress-strain curves is shown in (e). Similar plot is shown in [99].

rials in practical applications, three examples with continuously graded grayscale designs are being investigated. Tension tests are chosen to minimize the impact of geometrical nonlinearities and instabilities and to capture the material behavior until failure. These tests allow for a comprehensive assessment of the material's performance and enhance the reliability of the model for predicting the mechanical properties of grayscale MSLA-printed materials in real applications. The numerical simulations are carried out using MOOSE (Multiphysics Object Oriented Simulation Environment) open-source software [124].

Graded rectangular plate In Figure 4.6, a rectangular plate with dimensions 50 mm (width), 120 mm (height), and 2 mm (thickness) is shown. The grayscale value of the plate linearly varies from $G = 0.6$ to $G = 1.0$ from left to right, as shown in Figure 4.6 (a). Consequently, the material properties also change accordingly, as shear modulus μ is illustrated in Figure 4.6 (b). The plate is clamped in a tensile testing machine and subjected to stretching in the direction perpendicular to the material variation.

Simulation results of the grayscale material model for the sample at an applied strain of 9.5% are displayed in Figure 4.6 (c) , where the stress component $\mathbf{P}_{11}$ is visualized. Figure 4.6 (d) shows the sample after material failure at 10% strain. A comparison between the failed sample and the simulation indicates the presence of stress concentrations in the right corners, where the grayscale value is $G = 1.0$, indicating the highest stiffness. However, the failure stress is already reached in this region due to the stress state being between uniaxial tension and compression states, as depicted in Figure 4.2 (a). Additionally, the comparison of the numerical and experimental stress-strain curves in Figure 4.6 (e) demonstrates a good agreement. To obtain the numerical stress, the stress at the boundary of the geometry is averaged, while the experimental stress is calculated by dividing the reaction force measured by the tensile test machine by the cross-sectional area of the sample. The strain is determined by dividing the displacement prescribed by the tensile testing machine by the height of the sample. The same evaluation methodology is applied to subsequent test cases. For higher strain values, some deviations are observed, resulting in maximum and average absolute errors of approximately 0.78 MPa and 0.47 MPa, respectively. Nevertheless, this corresponds to a maximum relative error of 6.5%, indicating a reasonably accurate approximation.

Graded plate with hole The subsequent validation involves the examination of a classical example: a rectangular plate with a hole. Similar to the previous case, this configuration is subjected to tensile loading, as depicted in Figure 4.7. The geometric parameters remain the same as in the previous example, with the addition of a centrally located hole with a diameter of 22.5 mm. The grading follows a linear pattern orthogonal to the tension, ranging from $G = 1.0$ to $G = 0.6$, as shown in Figure 4.7 (a). Consequently, the material properties of the printed sample vary from left to right, as shear modulus is demonstrated in Figure 4.7 (b).

Figure 4.7 (c) displays the simulation of the sample using the grayscale material model at an applied strain of 5.3%, with the stress component $\mathbf{P}_{11}$ visualized. A picture of the printed sample in Figure 4.7 (d) shows the sample after material failure at 5.6% strain. Additionally, the stress distribution in the simulated sample highlights stress concentrations in the failed area during the experiments, where $G \approx 90\%$ and $\mathbf{P}_{11} \approx 15$ MPa. Furthermore, Figure 4.7 (e) compares the stress-strain curves obtained from numerical and experimental calculations, revealing a satisfactory alignment between the two sets of results. Similarly, for higher strain values, certain deviations are observed, resulting in maximum and average absolute errors of

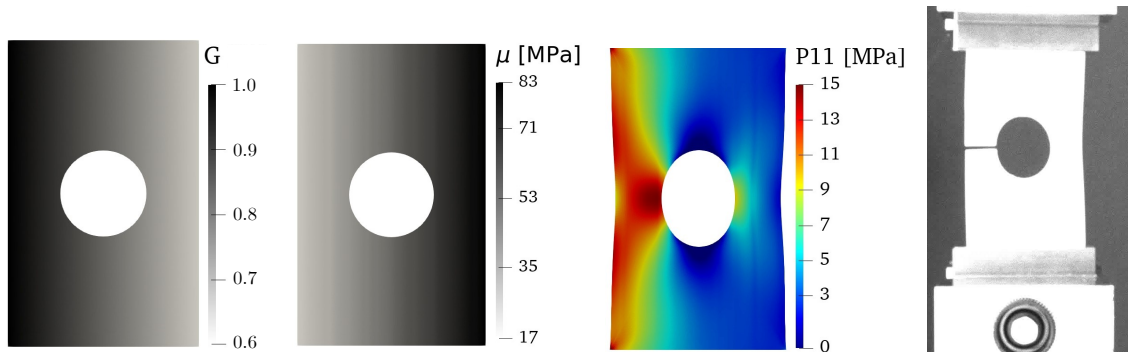

(a) Design of grayscale G **(b)** Shear modulus μ **(c)** Simulated stress $\mathbf{P}_{11}$ **(d)** Failed sample

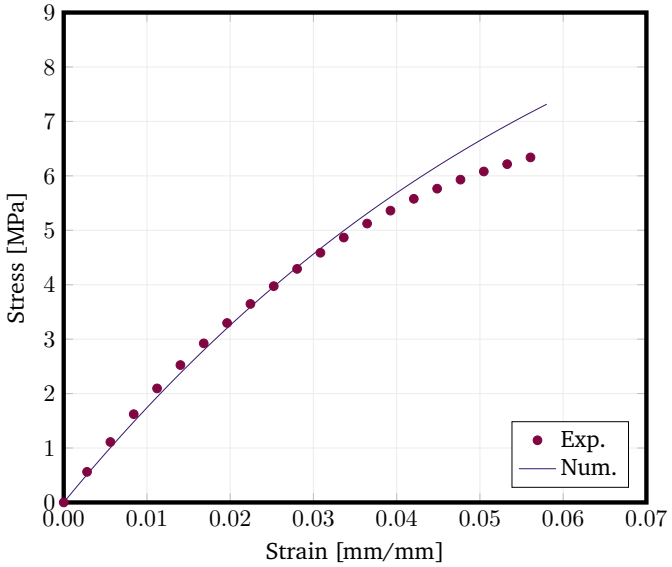

(e) Stress–Strain curves: Experimental vs. Simulation

Figure 4.7. A graded rectangle with hole with a gradient in grayscale, ranging linearly from $G = 0.6$ to $G = 1.0$, is considered. Additionally, the material properties vary in the direction of tension. This configuration is illustrated in (a) and (b). The simulated distribution of stress and deformation is depicted in (c). The shape of the structure after failure in the experimental setup is presented in (d). Finally, a comparison between the experimental and numerical stress-strain curves is shown in (e). Similar plot is shown in [99].

approximately 0.8 MPa and 0.24 MPa, respectively, along with a maximum relative error of about 12%.

Graded trapezoidal structure The final case for validation involves a trapezoidal structure with grading, as illustrated in Figure 4.8. The trapezoid has a height of 120 mm, a bottom width of 60 mm, a top width of 20 mm, and a thickness of 2 mm. In this configuration, the grayscale value varies linearly from bottom to top, ranging from $G = 0.6$ to $G = 1.0$, as shown in Figure 4.8 (a). Consequently, the material properties change along the tensile

direction, as shear modulus μ is depicted in Figure 4.8 (b). Figure 4.8 (c) displays the simulated deformation at 5.3% strain. Interestingly, the failure in Figure 4.8 (c) does not occur at the point of maximum stress but rather towards the bottom, where the softer material is more prone to failure. Comparing the stress-strain curves obtained from numerical and experimental calculations in Figure 4.8 (e) reveals a very good agreement between the numerical model and experimental results. The maximum and average absolute errors are approximately 0.24 MPa and 0.17 MPa, respectively, resulting in a maximum relative error of 2.5%. This indicates a close approximation to the experimental results and demonstrates the reliability of the numerical model in capturing the behavior of the graded trapezoidal structure.

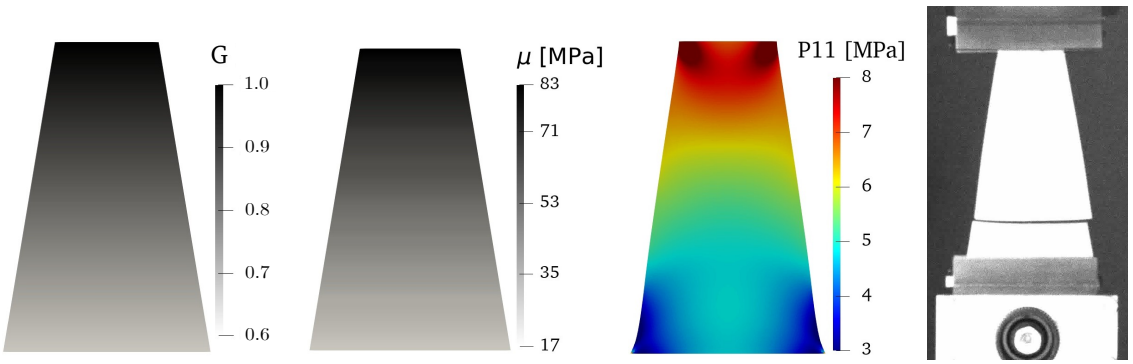

(a) Design of grayscale G **(b)** Shear modulus μ **(c)** Simulated stress $\mathbf{P}_{11}$ **(d)** Failed sample

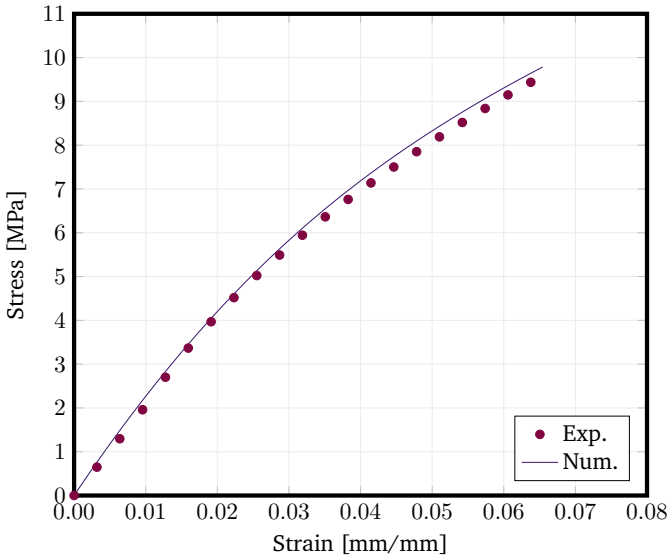

(e) Stress–Strain curves: Experimental vs. Simulation

Figure 4.8. A trapezoidal structure with a gradient in grayscale, ranging linearly from $G = 0.6$ to $G = 1.0$, is considered. Additionally, the material properties vary parallel to the direction of tension. This configuration is illustrated in (a) and (b). The simulated distribution of stress and deformation is depicted in (c). The shape of the structure after failure in the experimental setup is presented in (d). Finally, a comparison between the experimental and numerical stress-strain curves is shown in (e). Similar plot is shown in [99].

4.2. Rate Dependent Parametric Constitutive Modeling

In this section, the concepts of constitutive modeling from previous section are extended to develop a phenomenological visco-hyperelastic constitutive model for grayscale masked stereolithography printed materials undergoing finite deformations. The focus of this section is on the relationship between the constitutive parameters and the grayscale values of the mask, as well as the exposure time. The correlation between exposure time and grayscale is systematically investigated, specifically their influence on the rate-dependent mechanical properties of MSLA printed materials at large deformations. This analysis provides a comprehensive understanding of the relationship between these parameters. To simplify the design process, grayscale and exposure time, which are the two main process parameters in MSLA, were unified into a single, easily adjustable design parameter exposure intensity, as explained in Section 2.2. This unification aimed to ensure consistent and predictable mechanical properties of the final manufactured material. A parametric visco-hyperelastic constitutive model is developed to express the rate-dependent material behavior as a function of the exposure intensity. This model allowed for the design of functionally graded structures with spatially varying material behavior by appropriately parametrizing the constitutive parameters. The developed constitutive model is valid for scenarios in which plasticity is not considered (as in the case of one-time loading) and for situations where the material behavior displays rate-dependent characteristics. Then, these parameters of the developed model are experimentally identified and verified, ensuring its accuracy and applicability in practical scenarios. Through this chapter, a comprehensive understanding of the influence of process parameters, exposure time and grayscale, on the mechanical properties of MSLA printed materials is achieved. The unified design parameter and parametric visco-hyperelastic constitutive model contribute to advancements in the design of functionally graded structures with customizable material behavior in additive manufacturing.

The characterization of the printed material with varying exposure times and grayscales is conducted as the initial step, and the experimental results for different strain rates are presented in Section 4.2.1. Following this, the constitutive parameters are obtained by fitting the mathematical formulation to the experimental data across all ranges of grayscale and exposure time. Subsequently, the proposed concept of exposure intensity is validated, and the constitutive model is established for all exposure intensity ranges in Section 4.2.2. Finally, the constitutive model is validated for different exposure intensity values and at varying strain rates, as outlined in Section 4.2.2.

4.2.1. Visco-hyperelastic Constitutive Parameters

In the previous chapter, three distinct mechanical tests were conducted to determine the material's mechanical response under various loading conditions. The material's incompressibility

$G \setminus t$	20 s	15 s	10 s	8 s	6 s
1.0	1.86	1.68	1.43	1.29	1.11
0.9	1.51	1.36	1.16	1.05	0.90
0.8	1.19	1.08	0.92	0.83	0.71
0.7	0.91	0.82	0.70	0.63	0.55
0.6	0.67	0.61	0.52	0.47	—

Table 4.2. Values for exposure intensity H_v, Equation (2.2), by variation of grayscale G and time t for constant layer thickness $h = 0.05$ mm.

was established through a volumetric compression test. Consequently, for the remainder of this study, the material will be treated as incompressible, and the volumetric compression test will not be reiterated. The objective of this work is to examine the impact of process parameters on the final mechanical properties and develop parametric constitutive models. Therefore, conducting only a uniaxial tension test is adequate to demonstrate the dependence of mechanical properties on the process parameters. However, it is important to note that in practical applications, different mechanical tests are necessary to fully characterize the material being studied. The uniaxial tension tests in this section aim to assess the mechanical response of the materials with varying grayscale levels, including $G = 1.0, G = 0.9, G = 0.8, G = 0.7$, and $G = 0.6$, while exposing them to different exposure time intervals such as $t = 6$ s, $t = 8$ s, $t = 10$ s, $t = 15$ s, and $t = 20$ s. The layer thickness is considered to be $h = 0.05$ mm throughout this section. A summary of the resulting exposure intensity, Equation (2.2), can be found in Table 4.2. Additionally, in order to explore the viscoelastic behavior, tension tests are conducted at different strain rates: $\dot{\varepsilon} = 0.002$ s^{-1} (quasi-static), $\dot{\varepsilon} = 0.02$ s^{-1}, and $\dot{\varepsilon} = 0.2$ s^{-1}. In general, the outcomes exhibit a broad range of maximum stress values, ranging from approximately 1.5 MPa for the softest printed material ($G = 0.7$ and $t = 6$ s) to nearly 50 MPa for stiff material ($G = 1.0$, $t = 20$ s), and $\dot{\varepsilon} = 0.2$ s^{-1}. These findings demonstrate the feasibility of manufacturing graded materials with a diverse range of stiffness.

The average stress-strain curves obtained from the quasi-static tests are depicted in Figure 4.9 and Figure 4.10, showing the influence of grayscale and exposure time variations, respectively. Figure 4.9 demonstrates that increasing grayscale value leads to a corresponding increase in the stiffness of the material. Similarly, Figure 4.10 illustrates that an increase in exposure time value results in an enhanced stiffness of the material. Analysis of Figure 4.9 (a) indicates that, regardless of whether $G = 0.9$ or $G = 1.0$ is employed, the material appears to be fully cured when the exposure time is $t = 20$ s. Consequently, the grayscale variation does not considerably impact the mechanical behavior. However, for shorter exposure times, the stiffness becomes more sensitive to grayscale variation. This can be observed by comparing the curves for $G = 1.0$

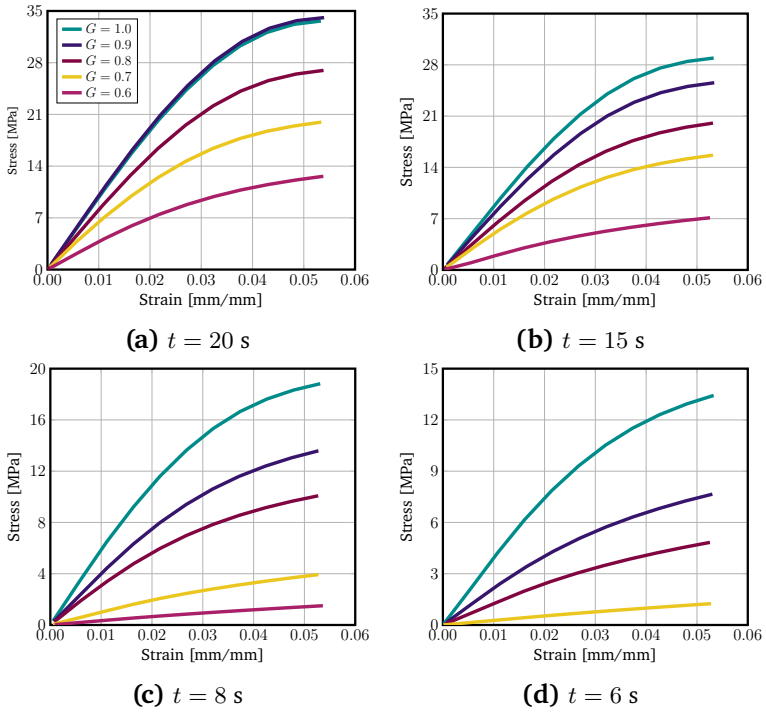

(a) $t = 20$ s **(b)** $t = 15$ s

(c) $t = 8$ s **(d)** $t = 6$ s

Figure 4.9. The experimental stress-strain curves were averaged for quasi-static uniaxial tension tests, considering a grayscale variation with constant exposure times ranging from $t = 20$ s to $t = 6$ s. Similar results are shown in [82].

and $G = 0.9$ in Figure 4.9 (a) with those in Figure 4.9 (d). Additional experimental results are accessible in Appendix A.3. A similar trend is evident when examining the exposure time variation for constant grayscales in Figure 4.10. The changes in stiffness are less sensitive to exposure time variation for higher grayscale values. Notably, increasing the exposure time of UV light for lower light intensity values enhances the degree of curing in the material. As a result, the duration of exposure significantly affects the polymeric network due to insufficient light energy. Figure 4.11 displays the stress-strain curves obtained from the experiments conducted for some selected combination of grayscale and exposure time at the three different strain rates. It is observed that as grayscale and exposure time increase, the curves for various strain rates converge, indicating a reduction in viscous properties due to increased crosslinking of the polymer chains.

The determination of the Mooney-Rivlin parameters involves fitting the material model presented in Equation (3.65) to the experimental data obtained from the tension tests. This fitting process allows for the identification of the coefficients necessary to establish the material model and subsequently compute the numerical stresses, specifically the first Piola-Kirchhoff stress tensor by Equation (3.67). Initially, the curve fitting procedure focuses on the quasi-static strain rate $\dot{\varepsilon} = 0.002$ s^{-1}. Similar to previous chapter, this is accomplished through

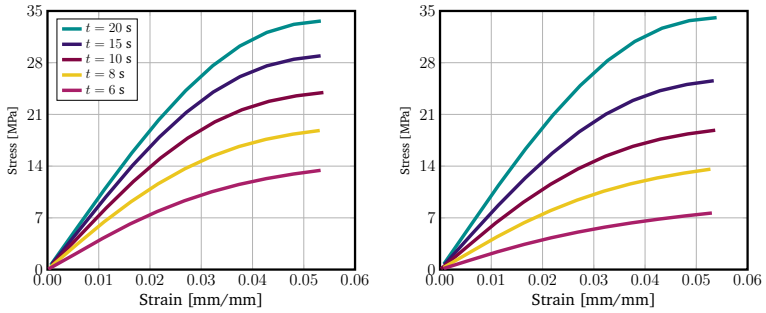

(a) $G = 1.0$ **(b)** $G = 0.9$

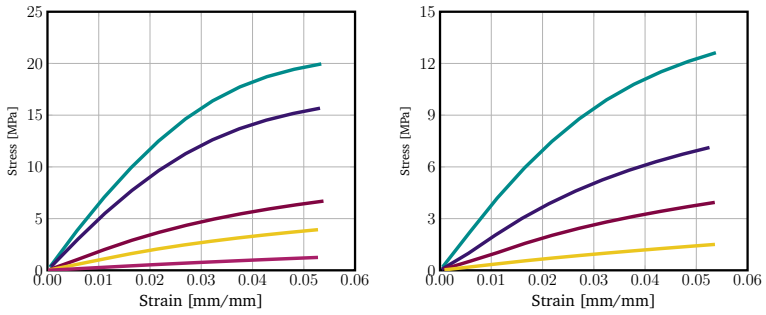

(c) $G = 0.7$ **(d)** $G = 0.6$

Figure 4.10. The experimental stress-strain curves were averaged for quasi-static uniaxial tension tests, considering an exposure time variation with constant grayscale values ranging from $G = 1.0$ to $G = 0.6$. Similar results are shown in [82].

a least-squares optimization technique, aiming to optimize the parameters of the (almost) incompressible hyperelastic material model Ψ^{∞}, as described in Section 2.3. Furthermore, this technique is extended to fit the experimental data to the visco-hyperelastic material model, with simultaneous parameter optimization for the other strain rates, $\dot{\varepsilon} = 0.02$ s^{-1} and $\dot{\varepsilon} = 0.2$ s^{-1}, as discussed in [51, 54]. The numerical first Piola-Kirchhoff stress resulting from the fitting process is then compared with the experimental data, as depicted in Figure 4.11. Additional experimental results are accessible in Appendix A.3.

The Mooney-Rivlin parameters C_{01}^{∞} and C_{10}^{∞}, which are obtained through fitting the equilibrium part of the material model, are depicted in Figure 4.12. It is evident that the magnitudes of these constitutive parameters increase as grayscale and exposure time increase. As previously mentioned in Equation (3.49), the shear modulus μ can be calculated from the Mooney-Rivlin material parameters using the relationship $\mu = 2(C_{01} + C_{10})$. Consequently, the shear modulus also increases with grayscale and exposure time, indicating an increase in material stiffness. Figure 4.13 illustrates the variation of the shear modulus with respect to grayscale and exposure time. Initially, it exhibits low values for $t = 6$ s and $G = 0.7$, then experiences a rapid increase towards higher values, and eventually converges at approximately 380 MPa in Figure 4.13 (a). Beyond this point, further increasing the exposure time has minimal impact on the shear

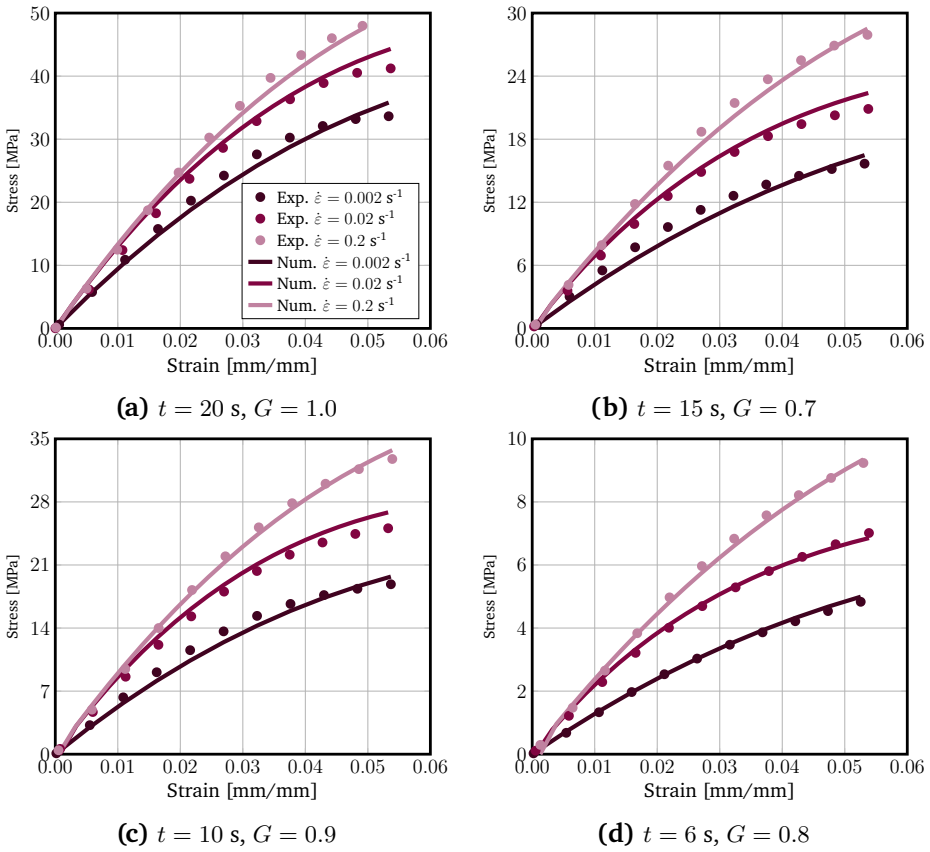

(a) $t = 20$ s, $G = 1.0$ **(b)** $t = 15$ s, $G = 0.7$

(c) $t = 10$ s, $G = 0.9$ **(d)** $t = 6$ s, $G = 0.8$

Figure 4.11. Experimental stress-strain curves were averaged and combined with a fitted material model of visco-hyperelastic for the purpose of uniaxial tension tests. The grayscales varied from $G = 1.0$ to $G = 0.6$, while the exposure time ranged between $t = 20$ s to $t = 6$ s. Additionally, different strain rates were considered, including $\dot{\varepsilon} = 0.002$ s^{-1} (quasi-static), $\dot{\varepsilon} = 0.02$ s^{-1}, and $\dot{\varepsilon} = 0.2$ s^{-1}. Similar results are shown in [82].

modulus, as the polymerization process is already fully completed.

An important finding, as depicted in Figure 4.13 (a), is that various combinations of grayscales and exposure times can yield identical stiffness values. This observation is further supported by Figure 4.13 (b), which displays the iso curves representing constant shear modulus values across different grayscale and exposure time combinations. Quantitatively, it can be concluded that higher grayscale values combined with shorter exposure times exhibit equivalent stiffness compared to lower grayscale values paired with longer exposure times. This significant result opens up possibilities for manufacturing graded structures with varying stiffness by manipulating the grayscale and exposure time, ultimately reducing the overall printing duration. As previously mentioned, however, that while the exposure time influences the curing of the entire printed layer, altering the grayscale impacts the curing of individual material points within the layer.

After evaluating the shear modulus using the Mooney-Rivlin material parameters through

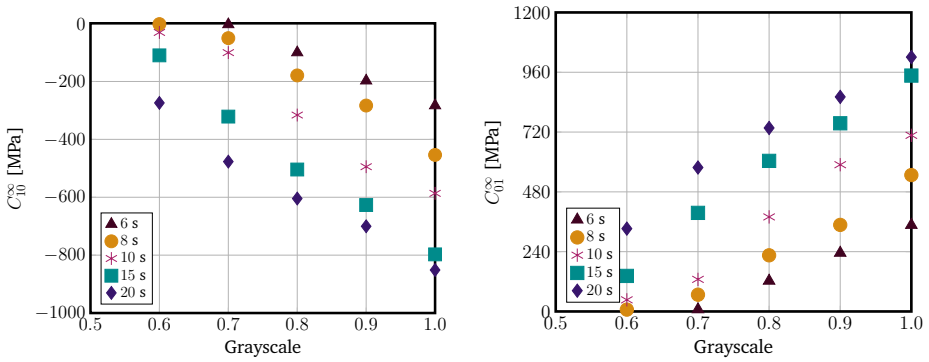

(a) **(b)**

Figure 4.12. The Mooney-Rivlin coefficients C_{01}^{∞} and C_{10}^{∞} were derived by performing a fitting process between the hyperelastic part of the material model Ψ^{∞} and the experimental data. This fitting was conducted considering various grayscales ranging from $G = 1.0$ to $G = 0.6$, as well as exposure times ranging from $t = 20$ s to $t = 6$ s. Similar results are shown in [82].

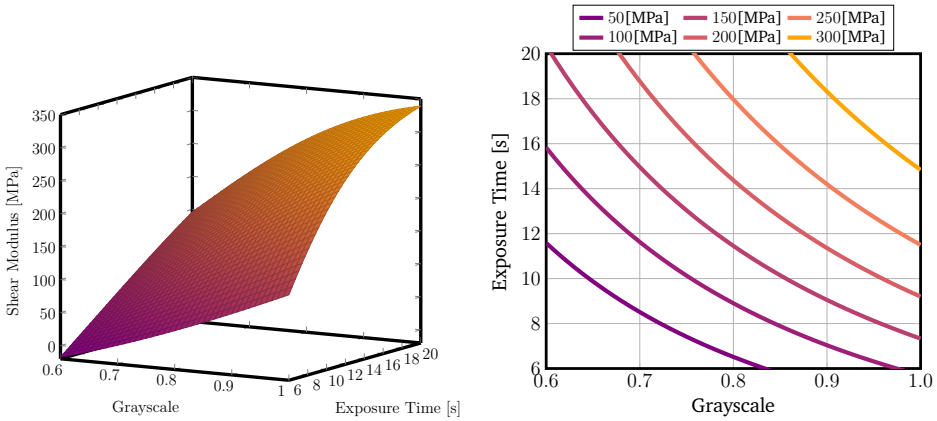

(a) 3D demonstration of shear modulus over exposure time and grayscale.

(b) Grayscale and exposure time variation resulting in identical shear modulus.

Figure 4.13. A correlation was established between grayscale, exposure time, and shear modulus. Similar plots are shown in [99].

fitting the visco-hyperelastic model, it becomes apparent that longer exposure times and higher grayscale values result in increased polymer chain conversion, leading to a stiffer printed material. The values corresponding to exposure intensity for varying exposure times and grayscales, can be found in Table 4.2. Additionally, for a visual representation of the correlation, please refer to Figure 4.14.

The Mooney-Rivlin material parameters corresponding to the equilibrium and non-equilibrium parts of the constitutive model are displayed in Figure 4.15 for different exposure intensity values. For lower grayscale values, such as $G = 0.6$, where the light intensity is relatively low, a gradual chemical reaction takes place. Consequently, the impact of increasing the exposure

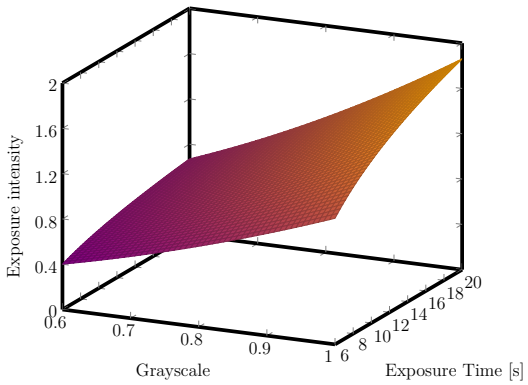

Figure 4.14. An illustration of exposure intensity in three dimensions is presented. Similar plots are shown in [99].

time on the reaction is minimal compared to higher grayscale values, for example, $G = 1.0$, where the liquid resin can rapidly solidify upon curing.

As it has been previously mentioned, the determination of the constitutive parameters C_{10}^{∞} and C_{01}^{∞} for the equilibrium part of the constitutive model, through fitting the experimental data at a quasi-static strain rate of $\dot{\varepsilon} = 0.002\ \text{s}^{-1}$. These parameters are showed in Figure 4.15 (a) and Figure 4.15 (b), corresponding to different values of exposure intensity. Additionally, the shear modulus μ^{∞} for the equilibrium part of the material model is calculated based on C_{10}^{∞} and C_{01}^{∞}. The relationship between μ^{∞} and exposure intensity is depicted in Figure 4.15 (c). The values of C_{10}^{∞}, C_{01}^{∞}, and μ^{∞} exhibit rapid growth for lower values of exposure intensity. This behavior arises from the initiation of polymerization and a high degree of monomer conversion [31]. Conversely, for higher exposure intensity values, where the uncured phase is reduced, further curing becomes challenging, leading to minimal changes in the shear modulus. This trend is particularly evident in Figure 4.15 (d) to Figure 4.15 (f), which represent the non-equilibrium part of the material model. With increasing exposure intensity, the constitutive parameters related to the non-equilibrium part undergo rapid increments compared to the equilibrium parameters until they reach a maximum value. This can be attributed to the rise in monomer conversion, resulting in fewer free monomers within the printed polymer's polymeric chains that can transform into a viscous solid. Consequently, the material properties associated with the non-equilibrium part cannot be further enhanced by increasing exposure intensity. Instead, higher exposure intensity values lead to an enhanced crosslinking density in the equilibrium state.

In relation to the constitutive parameters presented in Figure 4.15, it is predicted that these parameters vary based on their maximum value, which is attained when the material is completely cured. Consequently, a material parameter denoted as Φ in Equation (2.3) can be used as a function of exposure intensity to fit to the experimental constitutive parameters in Figure 4.15 in order to determine the parameters for any arbitrary exposure intensity

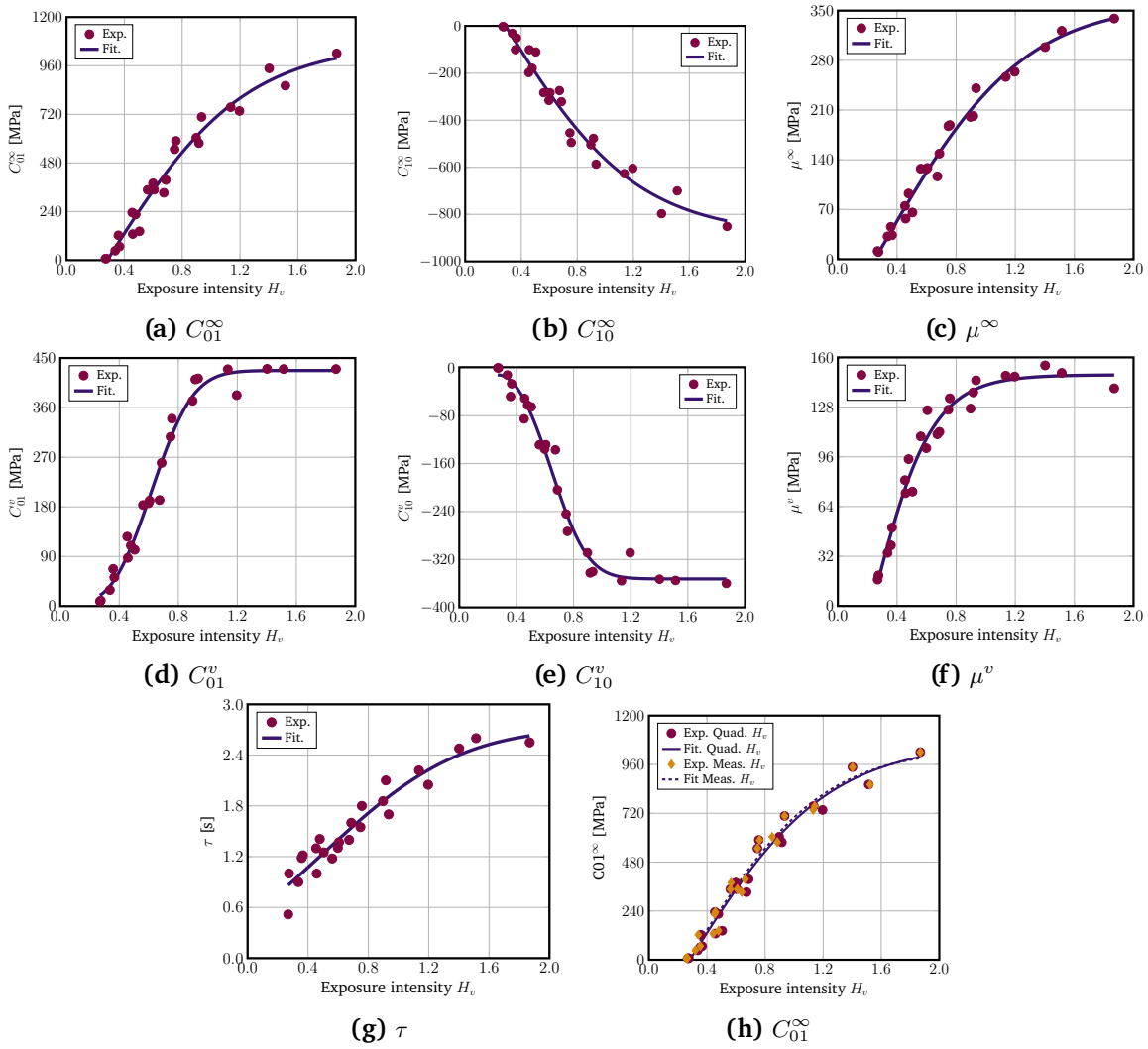

(a) C_{01}^{∞} **(b)** C_{10}^{∞} **(c)** μ^{∞}

(d) C_{01}^{v} **(e)** C_{10}^{v} **(f)** μ^{v}

(g) τ **(h)** C_{01}^{∞}

Figure 4.15. The experimental constitutive parameters of various exposure intensity values were subjected to fitting procedures using hyperbolic functions. Similar results are shown in [99].

values. The hyperbolic tangent function in Equation (2.3) is utilized for approximation of all Mooney-Rivlin coefficients, as provided in Equation (3.64), as well as for the relaxation time τ. It should be noticed that the exposure time was extended to 20 s, with the assumption that this duration of UV light would be sufficient to obtain the maximum crosslinking density for each layer, which is evident in Figure 4.15. Nevertheless, it is worth noting that the exposure time could potentially be further increased, taking into account considerations such as printer capacity, technology, and resin properties.

Correspondingly, the hyperbolic tangent function of H_v in Equation (2.3) is utilized to fit each constitutive parameter, enabling the determination of their respective maximum values and variables a, b, and c. The results of this fitting process are presented in Table 4.3. It is

	Φ_{max}	a	b	c
C_{01}^{∞}	1070	0.351	0.269	-0.188
C_{10}^{∞}	-889.1	0.351	0.274	-0.197
μ^{∞}	359.4	0.364	0.229	-0.139
C_{01}^{v}	440.7	0.615	0.336	-0.270
C_{10}^{v}	-381.3	0.536	0.319	-0.275
μ^{v}	154.9	-0.307	2.145	-0.822
τ	2.792	0.161	0.381	0.107

Table 4.3. Hyperbolic tangent function coefficients are determined through fitting to experimentally derived constitutive parameters. Similar table is shown in [99].

important to note that the maximum value derived from the fitting procedure coincides with the maximum values observed in the constitutive parameters curves illustrated in Figure 4.15. Attention should be given to the fact that the accuracy of the fitting results is dependent on the initial guess for the parameters. Thus, it is essential to select appropriate initial values that have physical significance. Specifically, when considering the Mooney-Rivlin material model, special consideration is given to ensure the consistency of the fitting for the parameters C_{10} and C_{01} with the physical properties.

Here, the hyperbolic tangent function is applied to C_{10}^{v} and C_{01}^{v} of the non-equilibrium part of the model. Consequently, the shear modulus μ^{v} can be calculated using the relationship $\mu^{v} = 2(C_{10}^{v}+C_{01}^{v})$. The results are displayed in Figure 4.16 as represented by the dashed-dotted

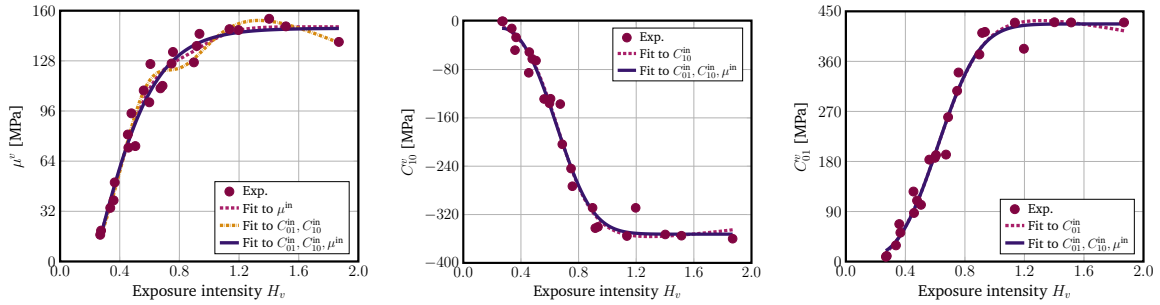

(a) Fit of μ^{v} over H_v **(b)** Fit of C_{01}^{v} over H_v **(c)** Fit of C_{10}^{v} over H_v

Figure 4.16. The material parameters of the Mooney-Rivlin model were subjected to a comparative analysis of various fitting strategies. Similar results are shown in [99].

lines. While the fitting results appear satisfactory upon visual inspection, differences can be observed in the shear modulus. In order to address this issue, a simultaneous fitting approach can be employed to obtain optimal results for both the constitutive parameters (C_{10}^{v}, C_{01}^{v}) and the shear modulus μ^{v}. This simultaneous fitting process ensures a comprehensive optimization of all parameters. The results obtained from the simultaneous fitting, depicted by the solid

H_v	t [s]	G
1.0	8	0.90
0.9	9	0.85
0.9	10	0.80

(a) $H_v \approx 0.9$

H_v	t [s]	G
1.3	8	1.00
1.2	9	0.95
1.2	10	0.90

(b) $H_v \approx 1.2$

H_v	t [s]	G
0.9	12	0.75
1.4	12	0.95
1.5	18	0.90

(c) Further cases

Table 4.4. exposure intensity values, grayscales, and exposure Times for constitutive model verification and validation. Similar tables are shown in [99].

lines in Figure 4.16, are in agreement with the optimum fitted function for the shear modulus, represented by the dashed line in Figure 4.16.

Finally, it is desired to demonstrate that the assumption of a quadratic model for G as defined in Equation (2.2) introduces only a minor error when compared to using the measured light intensities for different grayscales from Figure 2.3. Figure 4.15 (h) shows the coefficients C_{01}^{∞} for different combinations of G and t plotted against H_v. In one case, the analytical relation $H_v = G^2 \cdot \ln(t/t_0)/\ln(h/h_0)$ is employed, while in the other case, the experimentally determined relation $H_v = I_e(G)/I_e^{\max} \cdot \ln(t/t_0)/\ln(h/h_0)$ is utilized. Subsequently, a fitting process is carried out to determine the hyperbolic function representing $C_{01}^{\infty}(H_v)$. As predicted, the markers for H_v in both approaches closely align with each other, and similarly, the fitted curves exhibit a high degree of similarity.

4.2.2. Validation of Parametric Constitutive Model

The obtained results from the previous section are utilized to validate the definition of the exposure intensity denoted as H_v, as stated in Equation (2.2), serving as a unified parameter. Additionally, these results are employed to determine the coefficients of the parameterized constitutive model. It should be noticed that the model constants t_0 and h_0 in the definition of H_v in Equation (2.2) are determined by fitting the H_v model to the constitutive parameters corresponding to different H_v values. In this case, t_0 is found to be 1 s and h_0 is determined as 0.01 mm.

The proposed parametric constitutive model requires further experimental investigations to validate its effectiveness. One significant advantage of the proposed material model for grayscale MSLA is its parametrization based on the exposure intensity as a single design parameter, as indicated in Equation (2.2). This parameterization allows for the unification of grayscale and exposure time dependencies. As a result, the exposure intensity can be adjusted to achieve a balance between different exposure times and grayscales. This balancing is achieved by satisfying the equation

$$H_v(G_1, t_1) = H_v(G_2, t_2) \Leftrightarrow G_1^2 \cdot \ln(t_1) = G_2^2 \cdot \ln(t_2)\,, \tag{4.2}$$

where G_1^2, t_1, G_2^2, t_2 represent arbitrary values whose multiplication yields the same H_v.

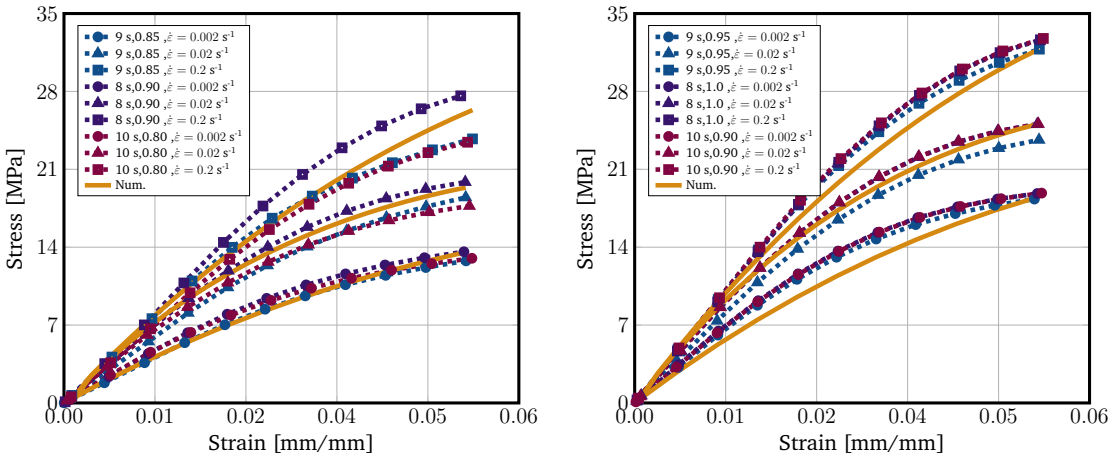

(a) **(b)**

Figure 4.17. The constitutive model is validated using new exposure intensity values, as well as pairs of grayscale and exposure time. Similar plots are shown in [99].

The examination of Table 4.2 reveals that a value of $G = 0.8$ and $t = 10$ s produces an equivalent exposure intensity value as $G = 0.9$ and $t = 8$ s, with $H_v = 0.9$. Consequently, it is anticipated that comparable polymerization and mechanical behavior can be attained due to the similarity in exposure intensity. To verify this assumption, a new combination of grayscale and exposure time, specifically $G = 0.85$ and $t = 9$ s with $H_v = 0.9$, is chosen for the purpose of printing and conducting the uniaxial tension test. Additionally, in order to validate the interpolation functions presented in Figure 4.15, the coefficients of this new grayscale-exposure time pair are interpolated and the first Piola-Kirchhoff stress is plotted as numerical results. The relevant details are given in Table 4.4 (a). The outcomes for these three distinct grayscale-exposure time pairs, all resulting in a similar exposure intensity, are shown in Figure 4.17 (a) for strain rates of $\dot{\varepsilon} = 0.002$ s^{-1}, $\dot{\varepsilon} = 0.02$ s^{-1}, and $\dot{\varepsilon} = 0.2$ s^{-1}. It is evident that there exists a satisfactory agreement among the experimental results for different grayscale-exposure time combinations. Nevertheless, a slight difference is observed at higher strain rates, which may arise from the material's solid nonlinear behavior at higher rates or the inherent experimental uncertainty associated with soft materials, particularly under high-rate conditions. Moreover, a more extensive characterization of the material could be accomplished by employing a greater number of test samples, thereby reducing the uncertainty.

The validation process was repeated for higher values of exposure intensity by comparing three sets of grayscale and exposure time with an approximate value of $H_v \approx 1.2$, as presented in Table 4.4 (b). The corresponding results are displayed in Figure 4.17 (b). Once more, it is evident that the experimental results align well with the numerical model across various strain rates, indicating a consistent agreement between them.

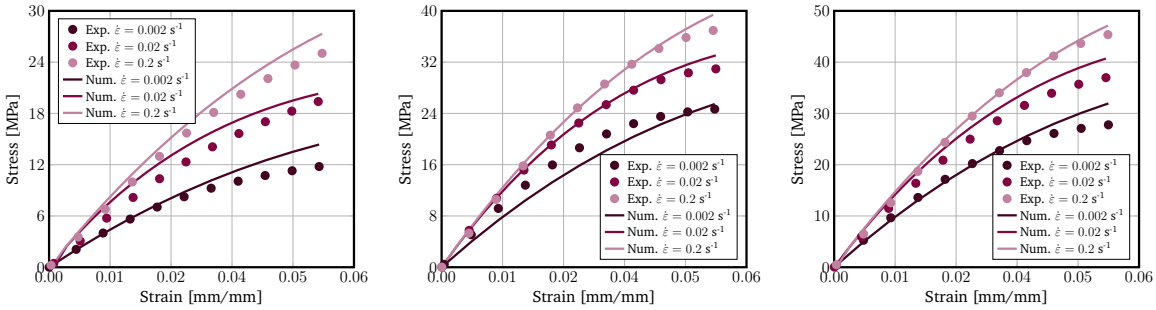

(a) $H_v = 0.9 (G = 0.75, t = 12)$ **(b)** $H_v = 1.4 (G = 0.95, t = 12)$ **(c)** $H_v = 1.5 (G = 0.90, t = 18)$

Figure 4.18. Validating the constitutive model with new exposure intensity values and pairs of grayscale and exposure time. Similar results are shown in [99].

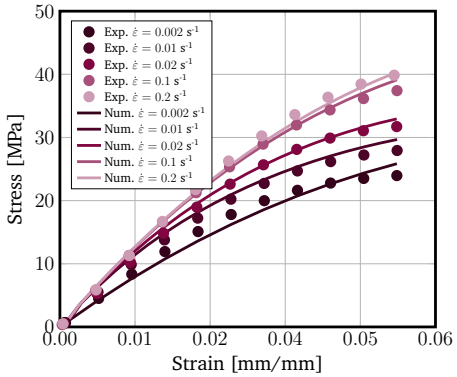

Figure 4.19. Comparison of experimental and numerical stress–strain curves in uniaxial tension test to validate constitutive model with different strain rates. Similar results are shown in [99].

The validation of the constitutive model is now performed, where stress-strain curves are estimated for arbitrary exposure intensity values across various strain rates. To include the complete spectrum of exposure intensity, the selections were made as $H_v = 0.9$, $H_v = 1.4$, and $H_v = 1.5$. Additionally, new combinations of exposure times and grayscales are determined and utilized, as shown in Table 4.4 (c). The results are illustrated in Figure 4.18. It is observable that the numerical stress-strain curves exhibit a good agreement with the experimental counterparts for different strain rates, while maintaining an acceptable margin of error. Overall, there is a better agreement between the numerical and experimental curves observed at higher values of exposure intensity, indicating greater stiffness in the material. In the final phase of the validation process, the constitutive model is compared across different strain rates to encompass the material's inelastic behavior. For this purpose, uniaxial tension tests are performed at the strain rates $\dot{\varepsilon} = 0.01\ s^{-1}$ and $\dot{\varepsilon} = 0.1\ s^{-1}$, while keeping the grayscale $G = 1.0$ and exposure time $t = 10$ s constant. The results are displayed in Figure 4.19. It is evident that the numerical stress-strain curves corresponding to strain rates not included in the model calibration exhibit a strong agreement with the experimental findings. Overall, it can be deduced that the parametric

visco-hyperelastic constitutive model has been effectively verified and validated, demonstrating its capability to accurately predict the mechanical behavior of grayscale MSLA 3D printed polymers in terms of a single parameter, namely the exposure intensity, across a range of strain rates.

4.3. Elasto-Visco-Plastic Constitutive Parameters

In this section, the study focuses on examining how the elasto-visco-plastic behavior of the gMSLA 3D printed parts is affected by the process parameters including layer thickness. In this way, the impact of process parameters on both the elastic and inelastic behavior and the corresponding parameters of the constitutive model outlined in Section 3.3.3 is studied. In the first step, the elasto-visco-plastic material model is characterized through conducting experimental uniaxial tension tests, considering various process parameters. Additionally, a correlation between the exposure intensity as defined in Equation (2.2) and the experimentally derived constitutive parameters is presented, providing evidence that exposure intensity serves as a suitable combination of the process parameters. The results and parametrization utilizing the exposure intensity from this section are employed to shows the potential for reducing printing time in the next section.

Uniaxial tension tests were conducted to failure at a speed of 5 mm/min, following the ASTM D638 standard, for various combinations of grayscale, exposure time, and layer thickness. To validate the relationship expressed by Equation (2.2), test samples are printed by varying one parameter among G, t, and h while keeping the other two constant. The resulting mechanical characterization data obtained for different exposure intensity values are then utilized to determine the constitutive parameters. Figure 4.20 depicts selected stress-strain curves obtained from experimental measurements, representing different process parameters. Additional experimental results are accessible in Appendix A.3. The experimental results consistently demonstrate a high level of reproducibility, with standard deviations ranging from 5.3% for the soft material ($H_v = 0.91$) to 1.98% for the stiff material ($H_v = 5.71$). Moreover, Figure 4.20 also includes the stress-strain curves for the fitted linear elastic and elasto-plastic constitutive model, as described in Equation (3.77). The quality of the fit is excellent, as the elasto-plastic model (represented by solid lines) closely corresponds to the experimental values (indicated by red circles) up to the point of failure. The dashed lines in Figure 4.20 represent the purely elastic part of the constitutive model.

The fitted parameters of the elasto-plastic constitutive model, namely the shear modulus μ, yield stress σ_0, and isotropic hardening modulus A_h, are presented in Figure 4.21. These parameters are shown for different exposure intensities H_v. Additionally, the influence of layer thickness ($h = 0.1$ mm, $h = 0.05$ mm, and $h = 0.02$ mm) on material strength is depicted. It is observed that thicker layers result in weaker material due to light attenuation, as schematically illustrated in Figure 2.1 (b) [58]. The stiffness, represented by the shear modulus, increases as the layer thickness decreases, as shown in Figure 4.21 (a). This variation in layer thickness allows for a wider range of stiffness, however with longer print times. To approximate the shear modulus, the hyperbolic tangent function in Equation (2.3) is employed, and the corresponding coefficients are determined as $\Phi_{max} = 220.6$, $a = -0.027$, $b = 0.476$, and $c = -0.072$.

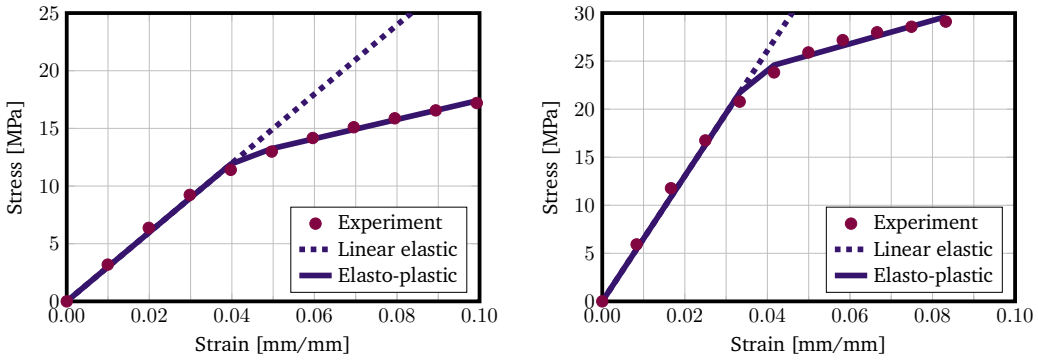

(a) $H_v = 0.91$ $(t = 1.5, G = 1.0, h = 0.05)$ **(b)** $H_v = 5.71$ $(t = 3, G = 1.0, h = 0.02)$

Figure 4.20. Characterization of uniaxial tension behavior of materials through varying grayscale, exposure time, and layer thickness. Averaged experimental stress-strain curves (dots), linear elastic models (dashed), and elasto-plastic models (solid) enable comprehensive analysis and comparison of mechanical properties. Similar results are shown in [97].

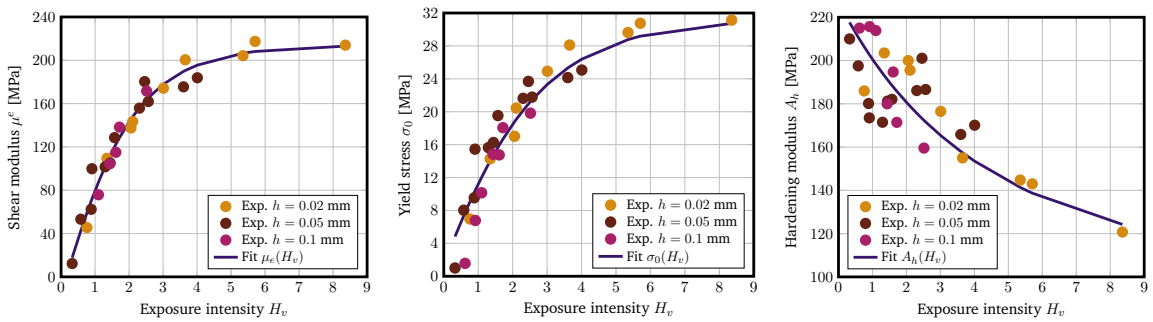

(a) Shear modulus μ^e **(b)** Yield stress σ_0 **(c)** Isotropic hardening modulus A_h

Figure 4.21. Dependencies of (a) shear modulus, (b) yield stress, and (c) isotropic hardening modulus on the exposure intensity. Experimental values for different process parameters are denoted by dots, while the solid lines represent fitted hyperbolic tangent functions $\mu^e(H_v)$, $\sigma_0(H_v)$, and $A_h(H_v)$, respectively. Similar results are shown in [97].

The yield stress σ_0 is plotted against different values of H_v in Figure 4.21 (b). Similar to the shear modulus, the yield stress exhibits an increasing trend with H_v, eventually converging for higher values of H_v. This behavior can be attributed to the fact that higher H_v values lead to increased material stiffness. The yield stress is approximated using a hyperbolic tangent function, as given by Equation (2.3), with coefficients $\Phi_{max} = 33.42$, $a = -0.016$, $b = 0.323$, and $c = 0.042$, which yields a good agreement with the experimental data. The hardening modulus is observed to decrease as H_v increases, as depicted in Figure 4.21 (c). The experimental results are effectively captured by a modified hyperbolic tangent function $\Phi(H_v) = \Phi_{max}/\tanh(a\,H_v^2 + b\,H_v + c)$, with coefficients $\Phi_{max} = 105$, $a = 0.001$, $b = 0.08$, and $c = 0.5$. This fitting demonstrates a satisfactory agreement with the experimental values.

Subsequently, the reliability of the constitutive model is evaluated through a relaxation test,

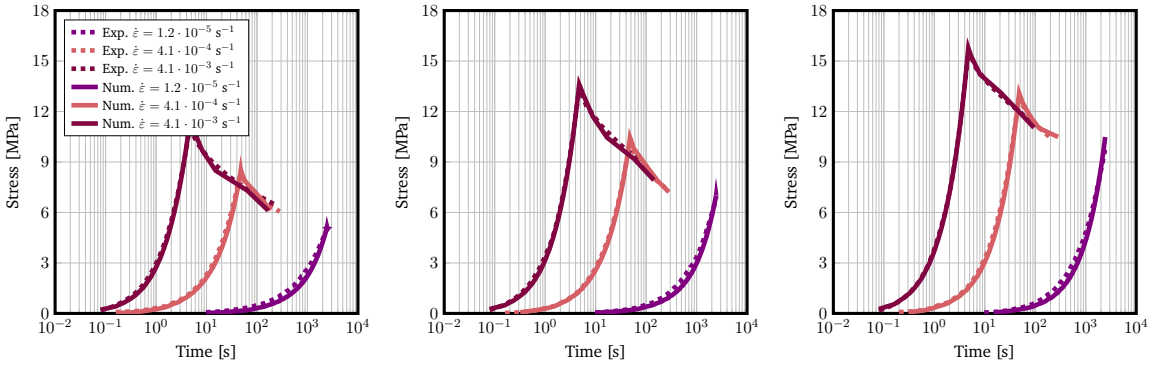

(a) $H_v = 2.4$ ($G = 1.0, t = 3, h = 0.05$) **(b)** $H_v = 3.2$ ($G = 1.0, t = 5, h = 0.06$) **(c)** $H_v = 6.8$ ($G = 0.9, t = 5, h = 0.02$)

Figure 4.22. Materials printed with different H_v values (a) 2.4, (b) 3.2, and (c) 6.8 are characterized for stress relaxation behavior. Experimental stress-strain curves are compared with viscoelastic model predictions for three strain rates:$\dot{\varepsilon} = 1.2 \cdot 10^{-5}$ s^{-1}, $\dot{\varepsilon} = 4.1 \cdot 10^{-4}$ s^{-1}, and $\dot{\varepsilon} = 4.1 \cdot 10^{-3}$ s^{-1}. Similar results are shown in [97].

G	t [s]	h [mm]	H_v	μ [MPa]	β_1	β_2	β_3	$\sum \beta_i$	τ_1 [s]	τ_2 [s]	τ_3 [s]
1.0	3.0	0.05	2.4	226	0.135	0.369	0.135	0.639	4.47	122	182
1.0	5.0	0.06	3.2	259	0.125	0.125	0.308	0.558	4.04	108	109
0.9	5.0	0.02	6.8	314	0.103	0.103	0.237	0.443	1.85	47	47

Table 4.5. Viscoelastic material parameters and process parameters for the relaxation tests shown in Figure 4.22.

and the variation of viscoelastic parameters is examined for different values of H_v. It involves subjecting a material to a constant deformation and subsequently monitoring the phenomenon of stress relaxation, which refers to the gradual decrease in stress over time under a constant strain condition as explained in Section 3.3.2. By analyzing the behavior of stress relaxation, it becomes possible to determine the viscoelastic properties of the material.

In the present study, the chosen strain level for the relaxation tests is set at 2% based on the observed linear elastic behavior in the preceding uniaxial tension tests, as illustrated in Figure 4.20. Notably, no plastic deformation was observed within the tested strain range, indicating that the material exhibited solely elastic behavior up to a strain of 2%. This strain level is considered appropriate for conducting relaxation tests because it allows the material to experience a significant deformation while still remaining within the linear elastic range. However, it is crucial to be conscious that the specific strain chosen for relaxation tests may vary depending on the material under study. Different materials exhibit diverse elastic and viscoelastic responses, necessitating the careful selection of an appropriate strain range for accurate and meaningful determination of viscoelastic parameters from relaxation test results. By conducting uniaxial tension tests at three different strain rates, the influence of strain rate

on the viscoelastic parameters of the constitutive model can be examined. Strain rate is a significant factor affecting the viscoelastic behavior, as the material's response to deformation can differ based on the rate at which the deformation is applied.

In Figure 4.22, the experimental data for three distinct H_v values, along with the corresponding fitted viscoelastic models, are presented. The stress reduction observed during the relaxation test, under constant applied strain, can be attributed to the relaxation process of the non-equilibrium stress contributions, as described by the summation term in Equation (3.77). This relaxation process causes the stress to gradually approach the equilibrium state. It is worth noting that a higher strain rate results in a more rapid reduction in stress due to the presence of greater non-equilibrium stresses within the material. The increased strain rate accelerates the relaxation process, leading to a faster convergence of stress towards the equilibrium state. The experimental data and the fitted viscoelastic models shown in Figure 4.22 provide an understanding into the viscoelastic behavior of the material under different H_v values, highlighting the significance of strain rate on the relaxation process and stress evolution during the relaxation test.

The process of determining the constitutive parameters involves several steps. Firstly, the elastic part of the material is fitted to the purple curve obtained at a low strain rate to minimize the influence of inelastic effects and determine the elastic constitutive parameters [51]. This allows for the characterization of the material's elastic behavior. Subsequently, the inelastic part of the constitutive model is fitted to the stress-strain curves obtained at strain rates of $\dot{\varepsilon} = 4.1 \cdot 10^{-4}$ s^{-1} and $\dot{\varepsilon} = 4.1 \cdot 10^{-3}$ s^{-1}. By comparing the numerical stress-strain curves with the experimental data, a good agreement is observed, indicating that the constitutive model effectively approximates the experimental behavior. The fitting is performed by analyzing the logarithmic scale of stress-strain curves over time. The corresponding constitutive parameters are presented in Table 4.5. Notably, an increase in H_v results in an elevation of the total shear modulus μ and a decrease in the relative modulus β_1, β_2, and β_3. This behavior, similar to the behavior explained in the previous section, can be attributed to the fact that an increase in H_v leads to a higher incorporation of free monomers into the crosslinked network, subsequently increasing the crosslinked density. As a consequence, the shear modulus of the equilibrium part of the material increases, while the shear modulus of the non-equilibrium part decreases. A similar trend is observed for the relaxation times τ_i, which decrease as H_v increases. This can be explained by the fact that an increased H_v corresponds to a higher degree of crosslinking, resulting in shorter relaxation times for the material. Overall, the characterization of constitutive parameters highlights the influence of H_v on the mechanical behavior and viscoelastic properties of the material.

In order to assess the suitability of the elasto-visco-plastic constitutive model for applications involving energy absorption, the material's response under cyclic loading conditions is investigated. Uniaxial tension tests involving loading and unloading up to strains of 3%, 6%, and 8%

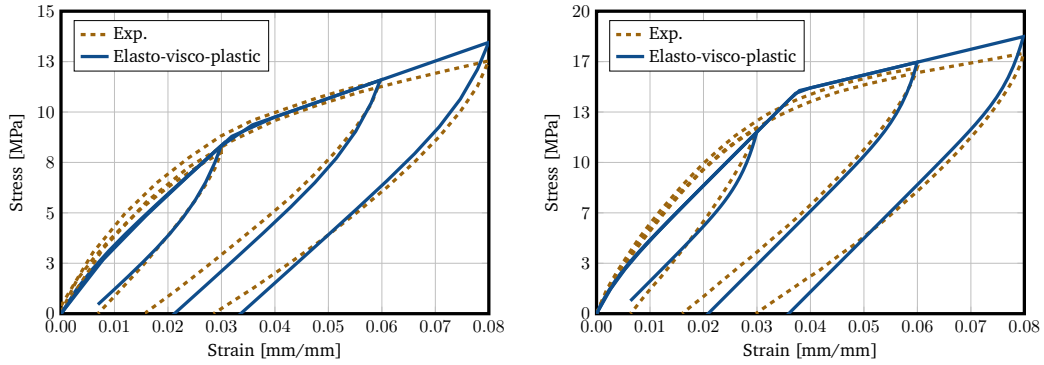

(a) $H_v = 2.4\,(G = 1.0, t = 3.0, h = 0.05)$ **(b)** $H_v = 5.8\,(G = 0.9, t = 4.0h = 0.02)$

Figure 4.23. Materials printed with H_v values of (a) 2.4 and (b) 5.8 are characterized for their cyclic behavior. Experimental stress-strain curves are obtained for loading-unloading conditions at strains of 3%, 6%, and 8%. These experimental curves are then compared with predictions from an elasto-visco-plastic model to analyze and evaluate the material's cyclic response. Similar results are shown in [97].

are conducted, with a strain rate of $\dot{\varepsilon} = 1.2 \cdot 10^{-5}$ s^{-1}. Figure 4.23 presents the experimental results against the model predictions for two different exposure intensities, specifically $H_v = 2.4$ and $H_v = 5.8$. It is evident that as the maximum strain increases, the material exhibits more significant plastic deformation, resulting in an increased deviation between the loading and unloading paths. The elasto-visco-plastic constitutive model effectively captures this behavior, both qualitatively and quantitatively. The model's predictions agree well with the experimental results, accurately representing the observed deviations between loading and unloading paths as the maximum strain increases. This successful correspondence between the model predictions and experimental data demonstrates the applicability of the elasto-visco-plastic constitutive model in scenarios requiring energy absorption. The model's ability to accurately capture the material's response under cyclic loading conditions further supports its potential for various practical applications.

4.4. Process Optimization

As previously stated, the relationship between process parameters within the exposure intensity can be employed to optimize the efficiency of the printing process for a given structure. The underlying principle revolves around the understanding that different combinations of process parameters, resulting in equivalent exposure intensity values, will yield similar mechanical behavior in the final product. This realization opens up opportunities for controlling the printing duration by manipulating three key factors: grayscale G, exposure time t, and layer thickness h.

To illustrate this concept, the manufacturing of a shell lattice structure is considered, as shown in Figure 4.24. The finite element simulations are carried out using Ansys software (2021 R2, 2021, ANSYS Inc., Canonsburg, PA, USA). In this particular example, three different combinations of process parameters are employed to fabricate the structure, while ensuring that each variant possesses an identical exposure intensity value, as outlined in Table 4.6. The dimensions of the lattice structure are set at 30 mm $\times$ 30 mm $\times$ 30 mm, with the shells within the unit cells having a thickness of 1.2 mm. To evaluate the mechanical behavior of the printed samples, force-displacement curves are obtained by subjecting the structures to compressive loading at a strain rate of $\dot{\varepsilon} = 0.002$ s^{-1} until failure. These curves, depicted in Figure 4.24, provide insights into mechanical behavior of structures printed with various parameters. As expected from previous investigations, despite being produced using different process parameters, the samples exhibit remarkably similar mechanical responses when exposed to identical exposure intensities.

G	t [s]	h [mm]	H_v	Print time [min]
1.0	2.0	0.03	2.27	90
1.0	3.1	0.06	2.27	57
1.0	3.4	0.07	2.26	52

Table 4.6. Printing parameters for shell lattice structures can be adjusted to achieve a 42% reduction in printing time without compromising the exposure intensity and mechanical behavior.

Moreover, it is worth noting that the experimental force-displacement curves exhibit a remarkable agreement with the results obtained from a finite element simulation for $H_v = 2.27$. However, upon closer examination of Table 4.6, it becomes evident that this desired mechanical behavior can be achieved with a significant reduction of 42% in printing time by selecting the process parameters $t = 3.4$ s and $h = 0.07$ mm instead of $t = 2.0$ s and $h = 0.03$ mm. This application effectively demonstrates the practical and industrial significance of utilizing the exposure intensity as a single unified process parameter, coupled with parameterized material and geometric models, to optimize printing time, a crucial factor in gMSLA applications.

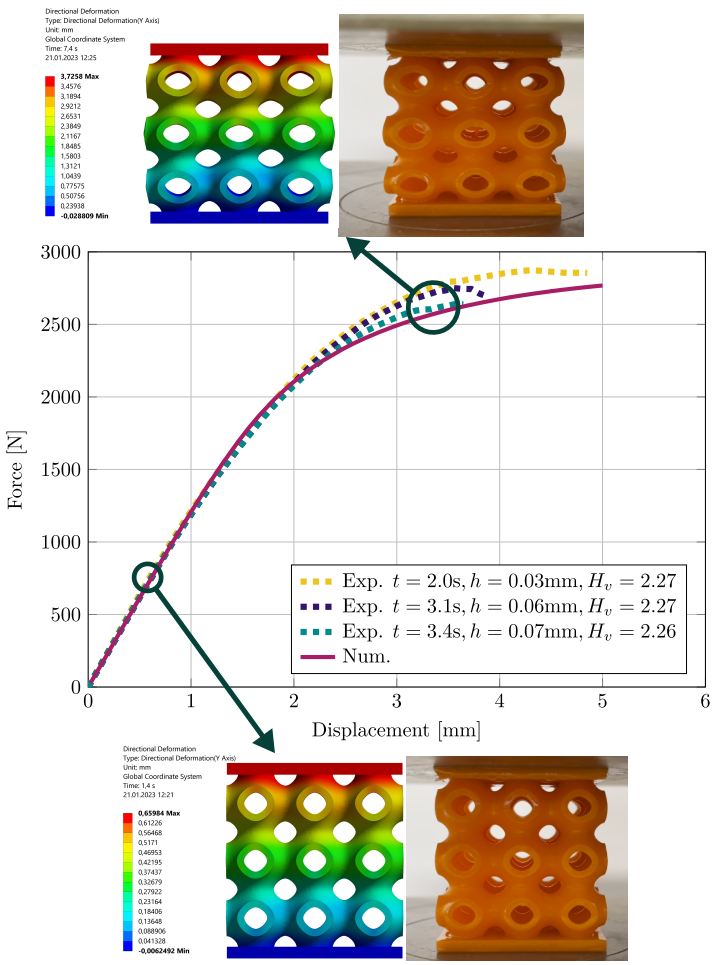

Figure 4.24. The compressive behavior of shell lattice structures was investigated using experimental force-displacement curves. Three sets of process parameters were used to fabricate the structures, all having identical exposure intensity values. The results obtained from the experiments were compared with numerical finite element simulations using an elasto-visco-plastic material model. The agreement between the experimental and numerical data was found to be very good. Similar results are shown in [97].

5. Influence of Process Parameters on Geometric Accuracy

As previously indicated, changes in process parameters influence the degree of cure of the photopolymer resin during the photopolymerization process, which can result in both overcuring and undercuring of the material. These changes have an impact not only on the mechanical characteristics, due to their influence on the density of crosslinking, but also on the ultimate solidified area within each layer. Consequently, the selection of suitable process parameters becomes essential in order to prevent deviations in shape from the initial computer-aided design (CAD). In the subsequent analysis, the effects of exposure time, grayscale, and exposure intensity on the deviation from the originally designed geometry are explored in depth. Finally, it is demonstrated that the geometric precision of a printed component can be enhanced by applying CAD correction.

5.1. Characterization of Geometrical Deviations

In the previous chapter, the influence of process parameters on mechanical properties was studied. Changes in the mechanical properties occur as a result of altering the process parameters, leading to over- and undercuring in the resin. To thoroughly investigate the impact of exposure time and light intensity on geometrical deviations for constant layer thickness, it is necessary first to study and characterize the geometrical changes for different values of process parameters. For this purpose, a lattice structure was specifically designed and printed for characterization, as shown in Figure 5.1. The lattice consists of interconnected trusses, each having a nominal diameter of 1.0 mm. The overall dimensions of the structure were set at 10 mm in length and 6 mm in height. During the printing process, grayscale values ranging from 0.6 to 1.0 were utilized, representing varying levels of light intensity. Moreover, the exposure time, which plays a crucial role in the solidification process, was varied and tested across a range of values between $t = 1.5$ s and $t = 6.0$ s. It is important to note that the layer thickness, denoted as h, was maintained constant at 0.05 mm throughout the experiments. By employing these carefully chosen parameter settings, it became possible to explore a broad spectrum of exposure intensities, denoted as H_v, ranging from 0.4 to 3.3.

To accurately evaluate the geometrical deviations of the printed lattice structures in comparison to the original CAD design, precise optical measurements of pixels were performed on four different sides of the structure. This approach allowed for a comprehensive evaluation of any variations in dimensions. The measurement process was repeated three times for each of the three different lattice samples that were examined, ensuring robust and reliable data collection. The resulting geometrical deviations were then quantified as Δ, representing the difference between the measured diameters and their corresponding nominal values. This quantification enabled a precise analysis of how exposure time and light intensity affected the overall dimensional accuracy of the printed lattice structures. The optimal process parameters required to achieve the desired level of precision in lattice structure fabrication can be obtained by formulating these deviations.

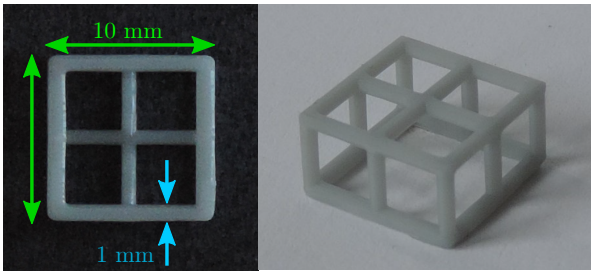

Figure 5.1. The lattice structure was employed in the investigation of the relationship between geometrical deviations and variations in grayscales and exposure times. Similar figure is shown in [97].

The impact of variations in grayscale values and exposure time on the sensitivity of geometric deviations is demonstrated in Figure 5.2. The graph in Figure 5.2 (a) shows that when grayscale values are increased (while keeping exposure time constant) or when exposure time is prolonged (while maintaining a constant grayscale), there is a noticeable increase in deviations. Additionally, it is observed that longer exposure time values lead to a heightened sensitivity of geometrical discrepancies to changes in grayscale values. This phenomenon can be attributed to two factors. Firstly, the prolonged exposure time allows for an extended period of monomer conversion, leading to a more significant increase of the crosslinked network. The additional time enables the monomers to react and form a more extensive network structure, resulting in increased deviations from the original design. Secondly, the increased in amount of light during prolonged exposure contributes to the enhanced crosslinking process, further influencing the geometrical discrepancies.

Moreover, it is evident from Figure 5.2 (a) that larger exposure time values generally lead to overcuring over shorter exposure times, while undercuring dominates for shorter exposure times. In other words, when exposure time is too short, the curing process is incomplete, resulting in deviations from the intended geometry. On the other hand, excessive exposure time can lead to overcuring, causing distortions and deviations from the original design. These

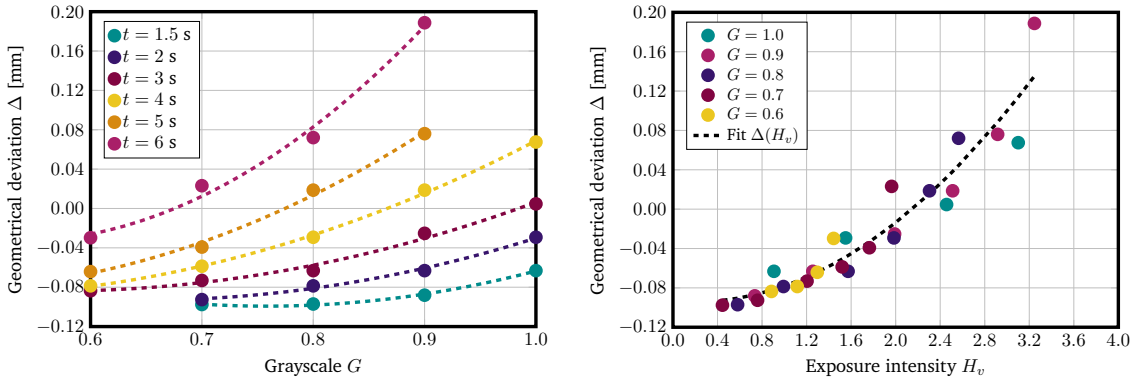

(a) **(b)**

Figure 5.2. The measured geometrical deviations Δ (represented by colored circles) and the fitted function (indicated by dashed lines) under different conditions. In panel (a), the deviations are observed for variation of grayscale and exposure times. In panel (b), the deviations are plotted over the exposure intensity. Similar curves are shown in [97].

patterns are also clearly demonstrated in Figure 5.2 (b), where the measured geometrical deviations are plotted against exposure intensities.

Analyzing Figure 5.2 (b), it can be observed that for smaller exposure intensity values, the geometrical deviations approximate almost -0.1 mm, indicating a shrinkage of 10% from the initial design. However, as the exposure intensity increase, the geometrical deviations also increase, reaching approximately +0.2 mm, which corresponds to a 20% increase from the original design.

To effectively model the experimentally measured deviations, the hyperbolic tangent function, as defined in Equation (2.3), is employed to represent the relationship between the measured deviations and the exposure intensity values. The constants in the hyperbolic function, $\Phi_{max} = -208, a = -0.01208, b = 0.00589$, and $c = 0.04314$, are determined to achieve a acceptable agreement between the model and the experimental data.

5.2. Geometrical Corrections

In practical scenarios, the derived function $\Delta(H_v)$ can prove to be highly beneficial in reducing geometric deviations by enabling adjustments to the geometry based on the selected process parameters. This capability allows for the optimization of 3D printing processes to achieve the desired dimensional accuracy and quality of printed structures. To exemplify the practical application of this concept, a representative structure is presented in Figure 5.3. This structure shows a graded middle truss that spans a range of exposure intensity values from $H_v = 1.6$ to $H_v = 0.4$ by varying the grayscale G from 1.0 to 0.5. Throughout this variation, the exposure time is kept constant at $t = 2.5$ s, and the layer thickness is maintained at $h = 0.05$ mm. The structure's dimensions consist of a height and width of 10 mm and 12 mm, respectively, with a thickness of 1 mm and a circular cross-section of 1 mm in diameter.

Upon printing the representative structure, the impact of reduced exposure intensity values becomes evident in Figure 5.3 (a). This figure illustrates that the printed structure with decreased H_v values exhibits noticeable shrinkage in the middle section of the truss. This shrinkage arises due to the inherent characteristics of the printing process, where lower grayscale values correspond to reduced exposure and, consequently, less complete curing and crosslinking of the material.

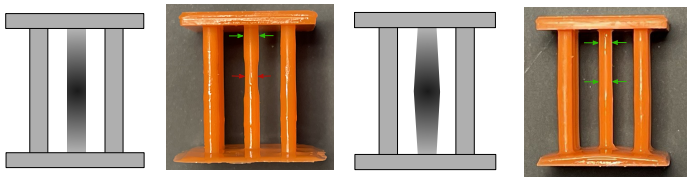

(a) Original design **(b)** With correction

Figure 5.3. Graded structure illustrating (a) geometrical shrinkage in the middle truss during printing of the original design and (b) enhanced accuracy obtained by implementing a geometric correction. Similar plot is shown in [97].

To resolve this issue and achieve the desired geometry, an improved design approach is implemented, as showed in Figure 5.3 (b). In this enhanced design, the cross-sectional area is adjusted by incorporating the $\Delta(H_v)$ function to effectively prevent the deviations associated with decreasing grayscale values. As a direct consequence of these adjustments, the corrected structure exhibits resolution of the shrinkage issues observed in Figure 5.3 (a). By treating for the predicted shrinkage using the $\Delta(H_v)$ function, the design ensures a consistent cross-sectional area throughout the graded truss. Consequently, the printed structure achieves the desired geometry with improved dimensional accuracy.

By employing the function $\Delta(H_v)$ derived from the experimental data, it becomes possible to predict the expected geometrical deviations and adjust the design accordingly. For instance, if a specific level of accuracy is desired, the function can be utilized to determine the appropriate

exposure intensity values needed to achieve the desired geometry. Conversely, if a target grayscale value is predetermined, the function can be utilized to the adjustment of other process parameters, such as exposure time or layer thickness, to compensate for the expected geometrical deviations and achieve the desired output.

This approach allows for more precise and efficient control of the 3D printing process, enabling the production of structurally and dimensionally accurate components. By utilizing the insights gained from the relationship between grayscale values, exposure time, and geometrical discrepancies, manufacturers can optimize their processes and reduce the occurrence of defects or inaccuracies in the printed structures. Ultimately, this contributes to advancing and adopting additive manufacturing technologies in various industries, ranging from aerospace and automotive to healthcare. It should be noted that the geometrical deviations vary among different 3D printers and are influenced by the photosensitive resin. Therefore, the proposed framework needs to be calibrated for practical applications, and the range of deviations must be determined for a specific printer and photosensitive resin.

6. Rate Dependent Energy Dissipation of 3D Printed Graded Structures

Viscoelastic structures possess unique properties that enable them to effectively dissipate and absorb energy, making them valuable in various engineering and materials applications. Energy dissipation refers to the ability of a material or structure to convert mechanical energy into other forms, such as heat or deformation, during loading conditions. Viscoelastic materials exhibit both viscous and elastic behaviors, combining the features of a fluid and a solid as explained in Section 3.3.2. This characteristic allows them to dissipate energy through internal molecular rearrangements, and relaxation processes, making them highly efficient in absorbing and dissipating mechanical energy. As mentioned in Section 3.3.2, the viscoelastic nature of a material is defined by hysteresis, which means that the loading and unloading curves do not overlap, as shown in Figure 6.1. This phenomenon illustrates the energy dissipated irreversibly when a material undergoes loading and subsequent unloading. The area under stress–strain curve is associated with absorbed energy, while the area between two curves in loading and unloading shows dissipated energy. This phenomenon is utilized for the purpose of mitigating vibrational energy. Certain materials, notably certain polymers and soft metals like lead, exhibit a pronounced capacity for damping vibrations [125].

The energy absorption capacity of viscoelastic structures is closely linked to their ability to decrease the effects of dynamic loading. As mentioned previously, when subjected to external loads, viscoelastic structures undergo time-dependent responses that involve both elastic and viscous deformations. The elastic component allows them to store and recover energy, while the viscous component facilitates energy dissipation through evolution of internal variable with time and energy loss mechanisms. This energy dissipation is an effect of energy loss in the material as a result of internal friction and molecular rearrangements during deformation. The combination of these properties enables viscoelastic structures to effectively dampen vibrations, reduce impact forces, and enhance overall structural integrity. This makes them highly desirable in applications such as shock absorbers, noise reduction systems, and structural components subjected to dynamic loading conditions.

In this chapter, the rate-dependent energy dissipation of 3D printed graded materials is investigated. To achieve this, samples with different grayscales are first printed and tested

to characterize their mechanical properties. This step involves repeating the characterization process in terms of grayscales as described in Section 4.1, because the resin has been changed and needs to be recalibrated. Next, a complex graded lattice structure is printed and tested under uniaxial compression. The numerical framework is validated by comparing numerical results from Ansys with experiments. Finally, the influence of different grading strategies and strain rates on energy dissipation is studied.

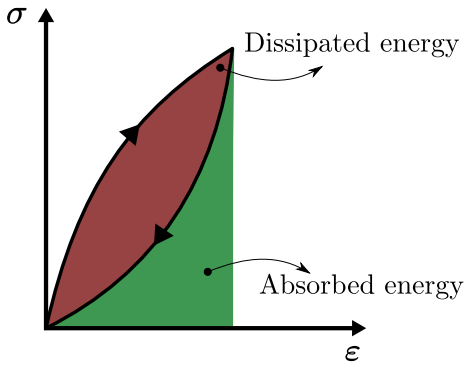

Figure 6.1. Schematic representation of hysteresis as a results of non-recoverable energy in loading–unloading. The absorbed energy is related to the region under the stress-strain curve, whereas the dissipated energy can be determined by the area between the loading and unloading curves.

Mechanical Characterization of Samples

In the previous chapters, the relationship between changes in exposure intensity and the mechanical properties of 3D printed materials was discussed. In this chapter, while layer thickness and exposure time are constant during the print process, grayscale is the only parameter that can be controlled in the production of graded structures. To establish a constitutive model for the materials, four different grayscale values, specifically $G = 1.0$, 0.85, 0.75, and 0.6, were chosen for calibration. The exposure time for calibration process was set to $t = 5$ s, and the layer thickness was maintained at $h = 0.05$ mm. The viscoelastic material model, represented by Section 3.3.3, was fitted to experimental curves obtained under three different strain rates. Initially, the elastic part of the model was calibrated using a uniaxial tensile test conducted at a strain rate of $\dot{\varepsilon} = 2.1 \cdot 10^{-5}$ s^{-1}.This allowed for the determination of the shear modulus μ. Subsequently, the viscoelastic constitutive model was fitted to higher strain rates of $\dot{\varepsilon} = 2.1 \cdot 10^{-3}$ s^{-1} and $\dot{\varepsilon} = 4.2 \cdot 10^{-3}$ s^{-1} to determine the relaxation time τ and relative modulus β. The resulting constitutive parameters for the different grayscale values are presented in Figure 6.2. Notably, the behavior of the constitutive parameters demonstrates nearly linear characteristics across the range of grayscale values. Consequently, a linear function can be employed to approximate the constitutive parameters for arbitrary grayscale values

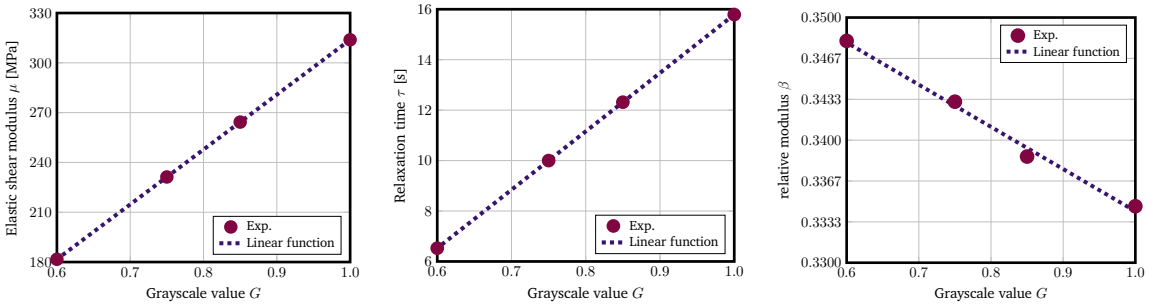

(a) Elastic shear modulus μ **(b)** Relaxation time τ **(c)** Relative modulus β

Figure 6.2. Determination of constitutive parameters as a function of grayscale values with variation of $G = 1.0$ to $G = 0.6$ for constant exposure time and layer thickness.

between $G = 0.6$ and $G = 1.0$ as

$$\Gamma(G) = a\,G + b\,. \tag{6.1}$$

The parameters of fitted linear function in the form of Equation (6.1) are given in Table 6.1. It is worth mentioning that the use of linear interpolation functions does not contradict the utilization of the hyperbolic tangent function Equation (2.3) discussed in previous chapters. This is due to the fact that the only variable affecting the exposure intensity in this case is the grayscale G, while the other parameters, such as the exposure time and layer thickness, remain constant. Therefore, a linear interpolation approach is applicable for predicting the mechanical properties based on grayscale variations within the given range, as demonstrated in Section 4.1.

Parameter	a	b
μ	330.5	-16.55
β	-0.123	0.455
τ	23.16	-7.368

Table 6.1. Coefficients of linear interpolation function to determine constitutive parameters for arbitrary values of grayscale G.

Validation of Numerical Models for Energy Absorption

In order to avoid repeating physical experiments, simulations can be validated and used to study different physical conditions and grading strategies. The primary objective is to validate the framework using a graded 3D printed complex structure. In this case, a shell lattice structure consisting of $5 \times 5 \times 3$ cells, with dimensions of 50 mm $\times$ 50 mm $\times$ 30 mm, was chosen for this purpose, as depicted in Figure 6.3 (a) and (b). To achieve gradation within the lattice, grayscale variation was employed, ranging from $G = 1.0$ to $G = 0.6$. The gradation starts from

the bottom, with the first layer of unit cells printed using $G = 1.0$, followed by the second layer using $G = 0.9$, and finally with $G = 0.6$ in the top layer. The gradation is shown in Figure 6.3 (c). The APDL programming language in Ansys is utilized to implement material grading. The APDL code is presented in Appendix A.2.

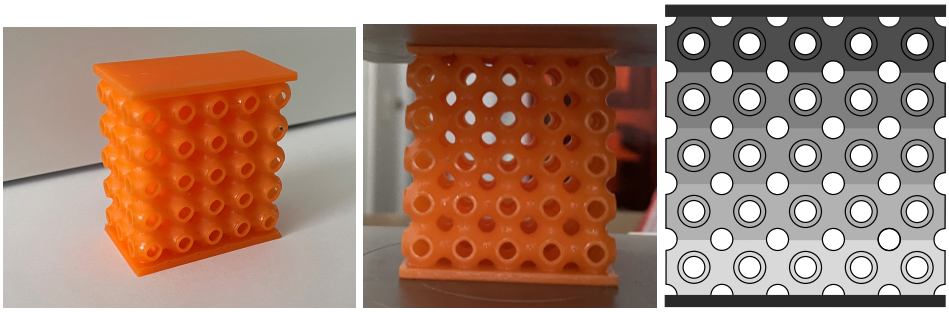

(a) **(b)** **(c)**

Figure 6.3. To establish the numerical framework, a graded 3D complex lattice structure was printed with $5 \times 5 \times 3$ cells, with dimensions of 50 mm $\times$ 50 mm $\times$ 30 mm. (a) and (b) 3D printed graded lattice structure. (c) Linear cell grading of lattice structure from bottom to top.

Two test case scenarios have been considered to validate the finite element simulations. The first scenario involves cyclic loading, where the graded lattice structure is subjected to a 2% strain and then immediately unloaded. The strain rate for this scenario is $\dot{\varepsilon} = 1.56 \cdot 10^{-3}$ s^{-1}.The corresponding force-strain and force-time curves are depicted in Figure 6.4.

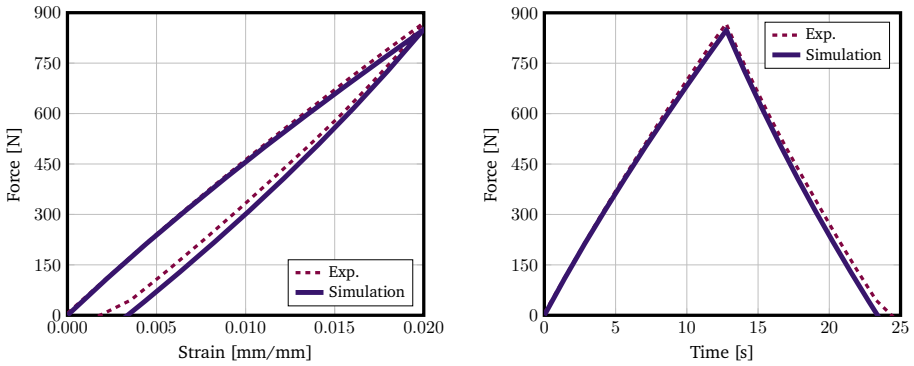

(a) Force–Strain **(b)** Force–Time

Figure 6.4. Validation of numerical simulations in Ansys through experiments in a cyclic loading.

It is evident from the graph that there is a high level of agreement between the experimental results and the numerical simulations conducted using Ansys. Moving on to the second scenario, where the relaxation behavior of the material is examined. In this case, the graded lattice structure is loaded to a 2% strain and held at that strain for a duration of 30 seconds before being unloaded. Once again, a comparison between the numerical and experimental data demonstrates a satisfactory level of agreement in Figure 6.5.

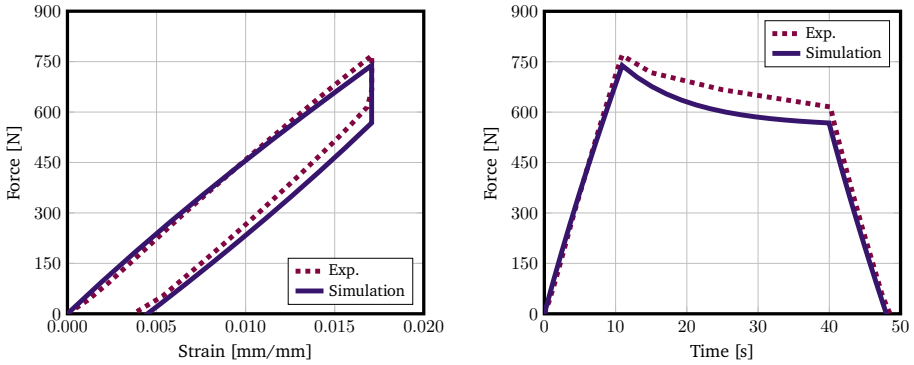

(a) Force–Strain **(b)** Force–Time

Figure 6.5. Validation of numerical simulations in Ansys through experiments in a cyclic loading with relaxation.

Investigation of Rate Dependent Energy Dissipation of Graded Structures

In this section, the study focuses on the investigation of rate-dependent energy dissipation in 3D printed graded structures, following the validation of the numerical framework and simulations in Ansys. To begin with, the mechanical behavior of the complex lattice structure depicted in Figure 6.3 (a) is examined to understand the influence of grading. It is important to note that while the grading method can be modified, it is essential to maintain consistency by ensuring a constant average grayscale value across the entire domain. This consistency is crucial for comparing identical effective stiffness in structure. To ensure similarity in the materials being compared, the effective material distribution, denoted as $\bar{G}$, must be consistent. The condition of consistency can be mathematically expressed as

$$\bar{G} = \frac{1}{\text{vol}(\Omega)} \int_{\Omega} G(\boldsymbol{x}) \mathrm{d}V \quad \forall x \in \Omega \,. \tag{6.2}$$

Consequently, various graded lattice structures are designed as illustrated in Figure 6.6. In the first case, the lattice structure depicted in Figure 6.6 (a) undergoes grading from $G = 1.0$ at the bottom to $G = 0.6$ at the top. This grading method involves assigning a specific grayscale value to each cell layer, resulting in a discontinuous transition between layers. The second case involves a continuous linear grading of the lattice structure, progressing from $G = 1.0$ at the bottom to $G = 0.6$ at the top, as shown in Figure 6.6 (b). In this scenario, the cells are linearly graded, in contrast to the first case in Figure 6.6 (a), where the cells maintain a constant grayscale value. Moving on to the next case presented in Figure 6.6 (c), the structure is graded from left $G = 1.0$ to right $G = 0.6$. In this arrangement, each vertical layer of cells possesses a uniform, constant grayscale. Figure 6.6 (d) demonstrates a disordered grading strategy where the stiffest layer is positioned in the middle of the lattice structure. Finally,

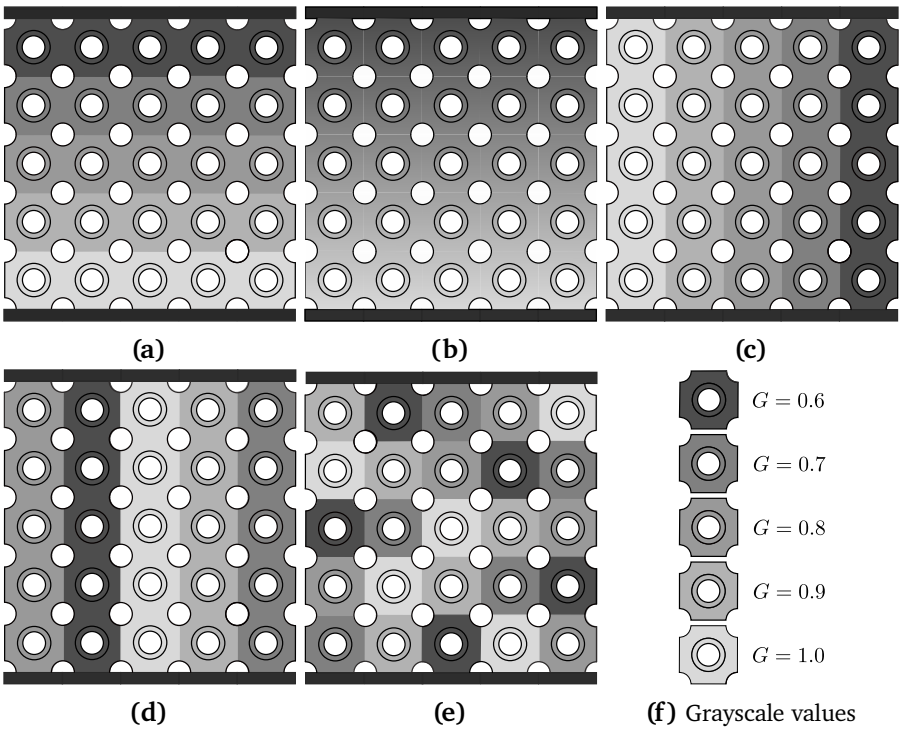

Figure 6.6. Design of various graded lattice structures with identical effective material distribution $\bar{G} = 0.8$: (a) Case 1: Layer grading from bottom to top. (b) Case 2: Linear grading from bottom to top. (c) Case 3: Layer grading from left to right. (d) Case 4: Inhomogenous layer grading. (e) Case 5: Inhomogenous cell grading.

Figure 6.6 (e) shows the lattice structure with inhomogeneous and random grading. In all the schematic illustrations provided in Figure 6.6, the dark cell color corresponds to $G = 0.6$, while the brightest color represents $G = 1.0$. In addition, the effective material distribution is identical for all grading cases as $\bar{G} = 0.8$.

In the initial phase, a comparative analysis is conducted on force-displacement curves corresponding to different gradings, as illustrated in Figure 6.7. This enables the investigation of the mechanical response influenced by diverse gradings. Figure 6.7 also presents the reaction force-displacement curves up to 2% strain with strain rate $\dot{\varepsilon} = 1.56 \cdot 10^{-3}$ s^{-1} for various cases, referred to as Figure 6.6. It can be observed that the mechanical behavior remains mostly unchanged when the effective grayscale values are identical, thus indicating minimal impact of the grading strategy.

In the subsequent stage, the dissipated energy of the graded structure depicted in Figure 6.6 (a) is investigated. The structure is subjected to compression up to 2% strain at various strain rates, ranging from quasi-static conditions at $\dot{\varepsilon} = 1.5 \cdot 10^{-5}$ s^{-1} to higher velocities at $\dot{\varepsilon} = 0.3$ s^{-1}. The normalized dissipated energy for different strain rates is represented by the red dots in Figure 6.8. It can be observed that the dissipated energy is relatively low for lower strain rates.

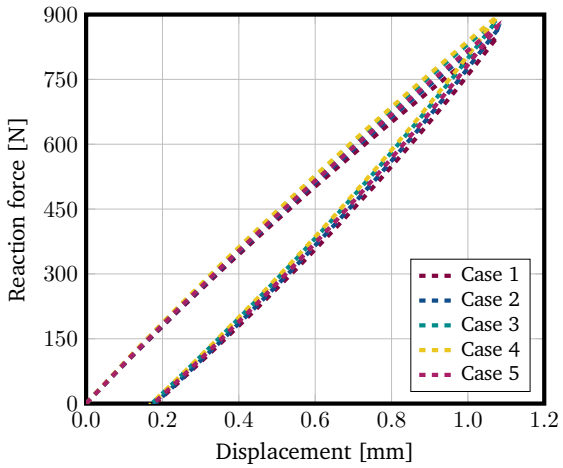

Figure 6.7. Comparison of reaction force-displacement curves for various grading cases in cyclic loading to 2% strain with strain rate $\dot{\varepsilon} = 1.56 \cdot 10^{-3}$ s^{-1}.

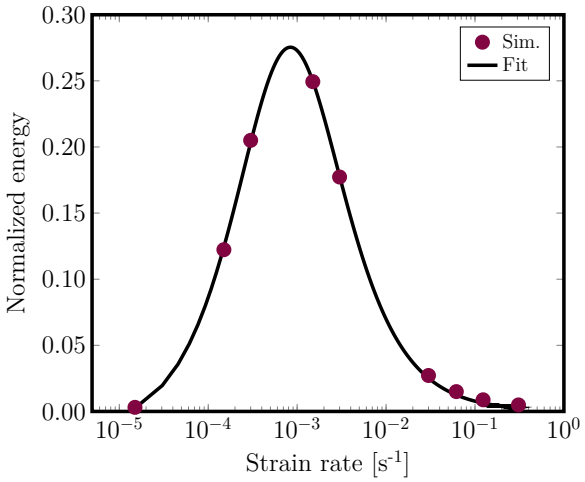

Figure 6.8. Energy dissipation for different strain rates in simulation and fit rational function.

However, as the strain rate increases, the dissipated energy reaches maximum values before decreasing again and converging to very small magnitudes. Understanding this behavior and the energy dissipation across different strain rates is crucial for designing structures intended for energy absorption applications.

In this context, a rational function can be employed to fit the energy dissipation for various strain rates, following the form

$$\mathbf{E}_d(\dot{\varepsilon}) = \frac{p_1 \cdot \dot{\varepsilon} + p_2}{\dot{\varepsilon}^2 + q_1 \cdot \dot{\varepsilon} + q_2}\,, \tag{6.3}$$

where the coefficients are

$$\begin{aligned} p_1 &= 0.04848\,, \\ p_2 &= -3.843 \times 10^{-5}\,, \\ q_1 &= 0.07236\,, \\ q_2 &= 0.002545\,. \end{aligned}$$

The fitted dissipated energy is depicted by the solid line in Figure 6.8. To determine the strain rate at which maximum dissipation occurs, the derivative of Equation (6.3) must be set to zero

$$\frac{d\mathbf{E}_d(\dot{\varepsilon})}{d\dot{\varepsilon}} = \frac{p_1 \cdot ((\dot{\varepsilon})^2 + q_1 \cdot \dot{\varepsilon} + q_2) - (p_1 \cdot \dot{\varepsilon} + p_2) \cdot (2\dot{\varepsilon} + q_1)}{((\dot{\varepsilon})^2 + q_1 \cdot \dot{\varepsilon} + q_2)^2} \equiv 0\,. \tag{6.4}$$

Solving Equation (6.4) yields $\dot{\varepsilon} = 8.6 \cdot 10^{-4}$ s^{-1} as the strain rate at which maximum dissipation takes place. This behavior can be attributed to the fact that, for lower strain rates, the viscoelastic element in Figure 3.4 moves freely and cannot withstand any stress. Consequently, the rheological system behaves like an elastic element with an elastic modulus of E^{∞}. On the other hand, for higher strain rates, the dashpot in the viscoelastic element behaves like a rigid element, resulting in an effective modulus of $E = E^{\infty} + E_i$. However, it is important to note that plastic deformation of the material is not considered in this investigation. Hence, when designing structures, it is important to consider that at higher strain rates, the material may undergo plastic deformation.

7. Enhancing Resin Flexibility for Energy Absorption applications

One drawback of the tough resins utilized in this research is their inherent lack of flexibility and low strain-to-failure characteristics, making them inappropriate for energy absorption applications. The primary objective of this chapter is to regulate the flexibility of the resin material. One proposed solution involves the incorporation of a flexible resin into the tough resin to reduce its toughness. Consequently, the aim is to investigate the impact of combining these two resin types on several crucial mechanical properties, including failure stress, failure strain, ultimate tensile strength, yield stress, and flexibility. The ultimate goal is to determine the optimal resin proportion that achieves the desired mechanical performance, striking a balance between strength and flexibility. Such findings would have significant implications for the design of energy-absorbing structures. To accomplish this objective, the elasto-visco-plastic properties of the material are examined for various resin combinations. Subsequently, an elastic-visco-plastic constitutive model is developed to establish a relationship between the resin proportions and the mechanical properties of interest. This model enables the prediction of the mechanical behavior of different resin proportions under deformation, thereby facilitating the identification of the optimal resin proportion for the intended application.

In the initial phase, it is essential to determine the mechanical response of various resin mixtures under standardized loading conditions. The combination of two distinct resins, namely flexible and tough, is determined based on their weight proportions. To establish a new parameter denoting the ratio of the two resins, the weight fraction of the flexible resin is utilized. This parameter, denoted as θ_f, is defined as the weight of the flexible resin divided by the total weight of both resins. Consequently, θ_f assumes values ranging from 0 to 1. The weight fraction of the flexible resin, θ_f, is calculated as follows

$$\theta_f = \frac{w_f}{w_f + w_t}\,, \tag{7.1}$$

where w_f and w_t denote the weights of the flexible and tough resins, respectively. The total weight of the resin is represented as $w_{\text{tot}} = w_f + w_t$. The weight fraction of the tough resin,

denoted as θ_t, can be determined using the following equation

$$\theta_t = \frac{w_t}{w_{\text{tot}}} = 1 - \theta_f \,. \tag{7.2}$$

In Equation (7.2), θ_f is the weight fraction of the flexible resin. In the subsequent parts of this chapter, various percentages of the proportions of the flexible resin, θ_f, are considered. Specifically, the following proportions are examined: $\theta_f = 0\%$ (pure tough resin), $\theta_f = 25\%$, $\theta_f = 50\%$, $\theta_f = 75\%$, and $\theta_f = 100\%$ (pure flexible resin).

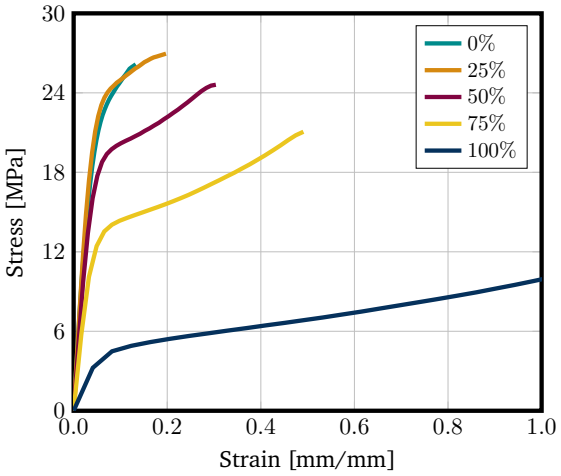

Figure 7.1. The stress-strain curves obtained from uniaxial tension experimental tests for variation of resin proportions ranging from $\theta_f = 0\%$ to $\theta_f = 100\%$.

Uniaxial tension tests were carried out on various combinations of resins to investigate their behavior under axial loading until failure occurred. The tests were conducted at a controlled speed of 5 mm/min, following the ASTM D638 standard, to ensure consistent and reliable results. The stress-strain curves for the complete range of resin combinations are shown in Figure 7.1, including pure tough resin, varying proportions of flexible resin, and pure flexible resin. During the experiments, the specimens were subjected to increasing tensile loads until they reached the point of failure. These curves serve as a fundamental basis for evaluating the mechanical performance and failure behavior of the resin mixtures under uniaxial tension, which is important for understanding their structural integrity and potential applications. As shown in Figure 7.1, the relationship between the proportion of flexible resin and the material's yield stress is evident. With an increase in the proportion of flexible resin, there is a noticeable decrease in the yield stress of the material. This finding suggests that the incorporation of more flexible components renders the material more flexible under tension. Conversely, as the mixture becomes more flexible, another significant observation is the corresponding increase in the failure strain. Specifically, the material's failure strain shows a remarkable rise from approximately 0.13 to well over 1.0. This substantial improvement in the failure strain indicates

that the material becomes considerably more resistant to breaking and can withstand higher levels of deformation before reaching its breaking point. The results of the strain-to-break analysis are illustrated in Figure 7.2. This analysis further confirms the favorable impact of incorporating flexible resin into the material, as it highlights the significant enhancement in the material's overall tensile properties. This graph provides a clear visual representation of how the failure strain increases in conjunction with the proportion of flexible resin, demonstrating the positive correlation between these two factors.

However, the main objective of this study is to enhance the flexibility of the tough resin, which has been the base material utilized throughout this research. Therefore, the resin mixture will only be increased up to $\theta_f = 50\%$. By limiting the mixture to $\theta_f = 50\%$ (half flexible) and keeping it within the range from $\theta_f = 0\%$ (pure tough) to $\theta_f = 50\%$, the base material can be retained as tough. As a result, the experimental data will consist of $\theta_f = 0\%$, $\theta_f = 25\%$, and $\theta_f = 50\%$ resin mixtures.

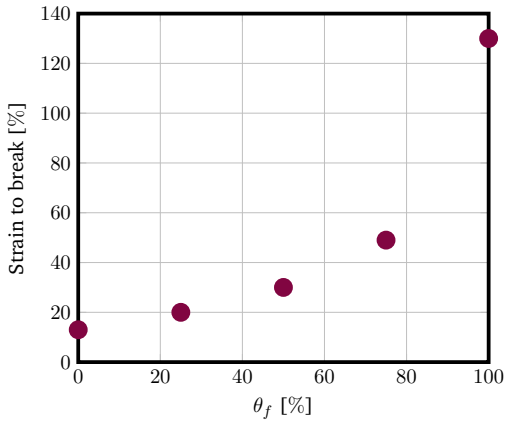

Figure 7.2. Strain to break for different resin proportions from $\theta_f = 0\%$ (pure tough) to $\theta_f = 100\%$ (pure flexible).

To conduct a comprehensive study of the material's behavior, both viscoelastic and plastic properties need to be investigated. Consequently, relaxation tests were conducted at different strain rates, as discussed in the previous section. These relaxation tests involved subjecting the material to controlled strains at varying rates and monitoring the stress response over time. The results of the material's relaxation behavior for various resin proportions are illustrated in Figure 7.3. The relaxation tests reveal interesting trends in the material's stress response concerning flexibility. As the proportion of flexible resin increases, the stress peak observed during the tests decreases. This suggests that incorporating more flexible components leads to a reduction in the material's overall stiffness, making it more yielding under applied stresses. Additionally, when examining the distance between stress peaks for two distinct strain rates, $\dot{\varepsilon} = 4.1 \cdot 10^{-4}$ s^{-1}, and $\dot{\varepsilon} = 4.1 \cdot 10^{-3}$ s^{-1}, it becomes evident that greater material flexibility results in an increased gap between these peaks. This indicates that the material's viscose

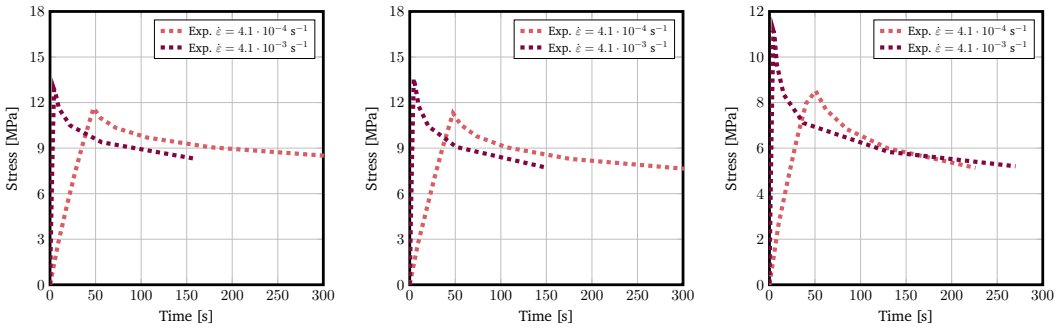

(a) $\theta_f = 0\%$ **(b)** $\theta_f = 25\%$ **(c)** $\theta_f = 50\%$

Figure 7.3. Experimental stress-time relaxation curves of samples printed with different tough–flexible resin proportions ranging from $\theta_f = 0\%$ (pure tough) to $\theta_f = 50\%$ for two strain rates: $\dot{\varepsilon} = 4.1 \cdot 10^{-4}$ s^{-1}, and $\dot{\varepsilon} = 4.1 \cdot 10^{-3}$ s^{-1}.

behavior contribution increases with enhanced flexibility. The presence of a higher proportion of flexible resin raises concerns regarding the material's susceptibility to plastic deformation under such conditions. This needs further investigation into the plastic properties of the material to understand the limits of its mechanical stability under different loading scenarios.

To have better understanding of the plastic behavior of the material, an investigation under cyclic conditions, similar to Section 4.3, was conducted. In this part, different resin mixtures with varying proportions were considered, namely $\theta_f = 0\%$ (pure tough), $\theta_f = 25\%$, and $\theta_f = 50\%$. These resin mixtures were subjected to cyclic loading and unloading to different strain levels, as illustrated in Figure 7.4. The cyclic loading involved progressively increasing the applied strain to 6%, 8%, 10%, and 12% and immediately unloading the samples without any pause. The results of the cyclic loading tests yielded perspectives on how the material's plastic behavior is affected by the changing ratios of flexible resin. As the flexible proportion θ_f increases, a notable trend emerges, where the maximum stress experienced by the material during the loading cycles decreases. This reduction in maximum stress reveals that materials with higher proportions of flexible resin tend to exhibit a lower overall strength under cyclic loading conditions. This observation has significant implications for applications where cyclic loading play a crucial role, as the material's endurance may be affected by the presence of flexible components. Moreover, the cyclic loading tests make the behavior of the plastic strain of the samples more clear. It is evident that as the proportion of flexible resin in the mixture increases, the plastic strain experienced by the samples during the loading and unloading cycles also increases. Understanding this relationship between flexible content and plastic strain is necessary for designing materials that can endure cyclic loading without experiencing excessive deformation or failure, ensuring their reliability and durability in practical applications.

The influence of flexible resin on material properties was investigated by fitting the elasto-visco-plastic constitutive model given by Equation (3.77) to the experimental data. In this

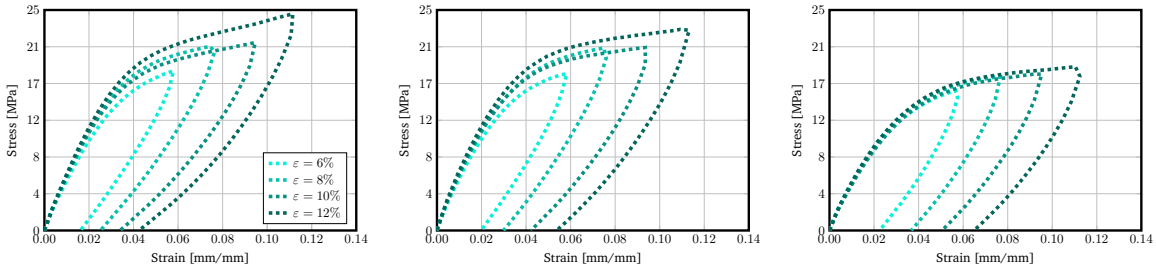

(a) $\theta_f = 0\%$ **(b)** $\theta_f = 25\%$ **(c)** $\theta_f = 50\%$

Figure 7.4. Experimental stress-strain curves in cyclic loading test for samples printed with different tough–flexible resin proportions ranging from $\theta_f = 0\%$ (pure tough) to $\theta_f = 50\%$. These curves are obtained for loading-unloading conditions at strains of 3%, 6%, 8%, and 12%.

chapter, the material modeling approach involved utilizing the elasto-visco-plastic constitutive model designed as explained in detail in Section 3.3.3. Initially, the viscoelastic part of the constitutive model was fitted to the relaxation data presented in Figure 7.3, and the corresponding constitutive parameters were determined. These constitutive parameters are illustrated in Figure 7.5, showing how the material's viscoelastic response changes with the proportion of flexible resin.

As evident from Figure 7.5 (b), the increase in the flexibility of the resin results in a nearly linear decrease in the elastic shear modulus of the samples. This decrease can be attributed to the occurrence of flexible bonds in the material's microstructure, leading to reduced elastic behavior and increased susceptibility to plastic deformation. Consequently, this higher flexibility in the material contributes to the observed higher strain to break, as deduced from Figure 7.2. The trend of linear changes with increasing resin flexibility is also evident in Figure 7.5 (c), Figure 7.5 (d), and Figure 7.5 (e), where the relaxation time τ, isotropic hardening modulus, and relative modulus β, respectively, also exhibit linear variations. As the proportion of flexible resin increases, these material properties show consistent and proportional changes, indicating a clear relationship between the amount of flexible resin and these constitutive parameters. In Figure 7.5 (f), the yield stress limit σ_y is shown for different percentages of flexible resin. Gradual decreases in the yield stress limit are observed with increasing flexibility in the mixture. Overall, it can be inferred from Figure 7.5 that the constitutive parameters demonstrate consistent behavior as the flexibility of the material in the mixture changes. In the next phases, it should be feasible to further customize the flexibility of the material according to the specific application of the printed structure. Achieving an optimized resin mixture for real-world applications requires not only precise blending of the flexible resin but also the ability to tailor the material properties to meet specific performance criteria. To this end, it is essential to determine the elasto-visco-plastic constitutive parameters for any arbitrary weight percentage of flexible resin θ_f. Different interpolation functions can be employed to

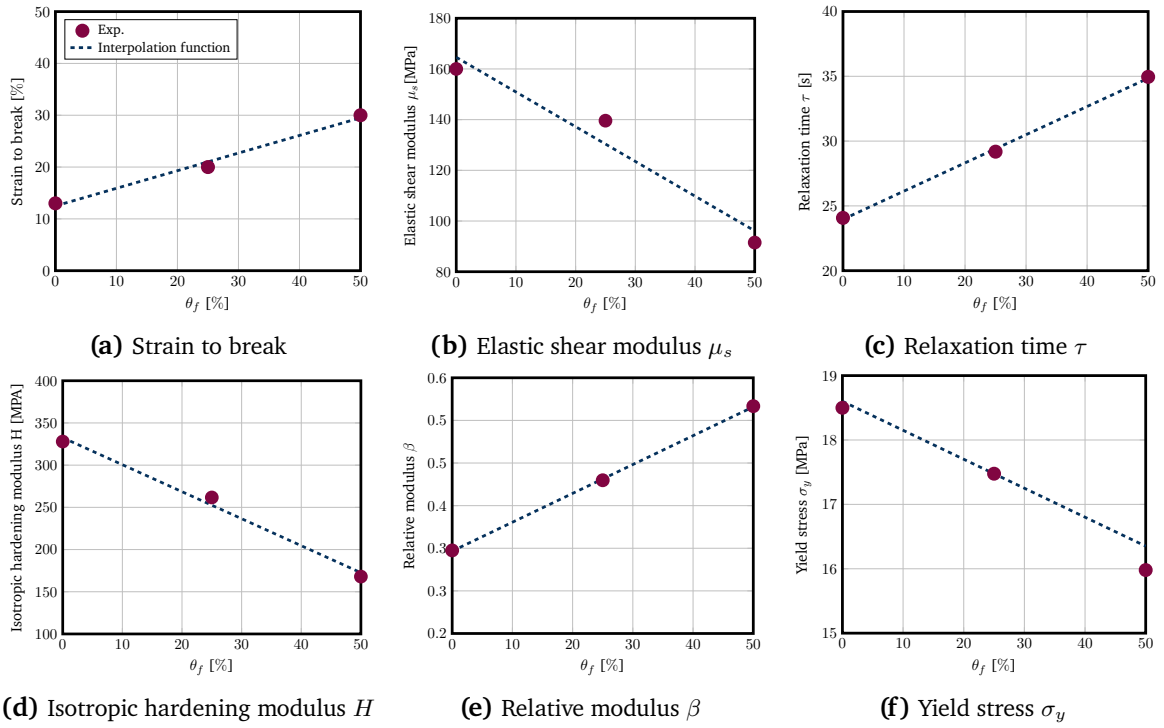

(a) Strain to break **(b)** Elastic shear modulus μ_s **(c)** Relaxation time τ

(d) Isotropic hardening modulus H **(e)** Relative modulus β **(f)** Yield stress σ_y

Figure 7.5. Parameters of the elasto-visco-plastic constitutive model for different percentages of the flexible resin, $\theta_f = 0\%$, $\theta_f = 25\%, \theta_f = 50\%$. Interpolated functions are used to determine the parameters for arbitrary values of resin combination.

approximate the constitutive parameters accurately. Here, linear interpolation functions are then applied to fit the experimental data shown in Figure 7.5. As observed, the quality of the fit appears to be satisfactory, indicating that the interpolation methods can effectively predict the constitutive parameters for intermediate values of θ_f. This capability holds great promise in enabling precisely design materials with desired mechanical properties for specific applications, providing enhanced control over the performance and functionality of 3D printed structures.

In the final stage of this chapter, the constitutive framework for the tough-flexible resin mixture must be validated through experiments for an intricate case. To achieve this, the lattice structure from the previous chapter is chosen due to its complexity, nonlinearity, and its successful validation in ANSYS in the previous chapter. For the validation process, two different weight percentages of flexible material, $\theta_f = 30\%$ and $\theta_f = 40\%$, are selected, and the constitutive parameters are interpolated based on the data presented in Figure 7.5. The shell lattice structure consists of $5 \times 5 \times 3$ cells, with dimensions of 50 mm $\times$ 50 mm $\times$ 30 mm, as illustrated in Figure 6.3 (a). The domain is meshed with tetrahedral second-order elements including 220000 elements in ANSYS Mechanical. In the experimental setup, the lattice structure is compressed at a constant velocity until it reaches the failure point, which is at almost 6 mm displacement in this case. The compression test aims to evaluate the structural

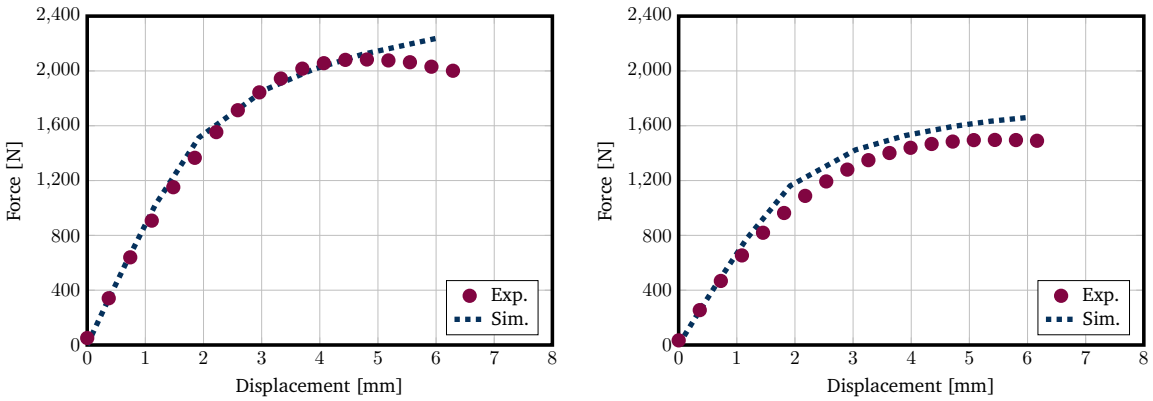

(a) $\theta_f = 30\%$ **(b)** $\theta_f = 40\%$

Figure 7.6. Validation of constitutive framework by comparing experimental and simulated force–displacement curves for interpolated constitutive parameters of $\theta_f = 30\%$ and $\theta_f = 40\%$.

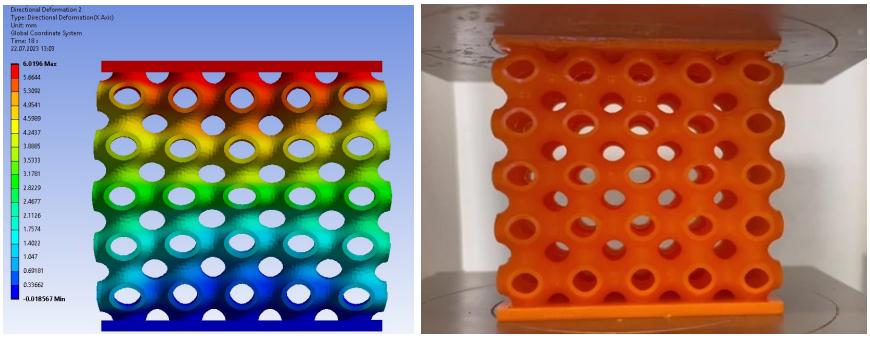

(a) Finite element simulation **(b)** Experiment

Figure 7.7. Qualitative illustration of lattice structure in simulation and experiments by almost 11% strain.

integrity and load-bearing capacity of the lattice structure under practical operating conditions, validating the accuracy and reliability of the constitutive model for the tough-flexible resin mixture. This validation process ensures that the developed constitutive model can predict the mechanical response of the lattice structure, allowing for its effective application in design scenarios.

The Ansys software is used to implement the constitutive model and simulate the lattice structure until the point of failure. The force-displacement curves obtained from experiments and finite element simulations are depicted in Figure 7.6. The qualitative deformation in experiments and simulations is also shown in Figure 7.7. As seen, there is a good agreement between simulations and experiments for $\theta_f = 30\%$ in Figure 7.6 (a). However, after reaching 5 mm of displacement, the experimental curve deviates from the simulation, resulting in noticeable discrepancies during the final phases of the experiments. This difference is attributed to the geometry failure in the experiments, which is not accounted for in the simulations. The

simulated and experimental force-displacement curves are also presented for $\theta_f = 40\%$ in Figure 7.6 (b). Initially, there is good agreement between simulations and experiments, but the deviations between the two curves increase as the deformation progresses. One possible reason for this could be that as flexibility increases in the material, the cells of the lattice structure become more prone to geometrical instabilities. These instabilities may lead to non-linear and unpredictable behavior in the experimental results, causing the deviations between the simulated and experimental force-displacement curves observed during the latter stages of the test. It is essential to thoroughly analyze these observed deviations and consider the effects of geometrical instabilities and other potential factors that could influence the structural response of the lattice under increased flexibility conditions. In future, addressing and understanding these complexities will enable the constitutive model to be refined and improved further, ensuring its accuracy and reliability in predicting the mechanical behavior of lattice structures made from the tough-flexible resin mixture for a wide range of applications.

8. Summary and Conclusions

The application of grayscale masked stereolithography (gMSLA) for the manufacturing of functionally graded engineering parts with varying material properties was explored in this dissertation, with a focus on elastic and inelastic behavior in finite and small deformations. For this purpose, the dependencies of material behavior and geometric deviations on the process parameters were experimentally investigated and modelled computationally for a specific commercial gMSLA 3D printer and photopolymer resin. The feasibility of gMSLA in creating graded parts with customizable mechanical behavior, particularly elastic, viscoelastic, and plastic properties, was successfully demonstrated, thereby presenting new opportunities for designing polymer structures.

In the first stage, a hyperelastic constitutive model was developed, considering the parametric dependence on grayscale value, which controls the intensity of light and consequently the curing of UV-curable photopolymer materials. The Mooney-Rivlin hyperelastic constitutive model with three parameters was utilized for this purpose. Experimental tests, including uniaxial tension and compression, as well as volumetric compression, were conducted on specimens printed at different grayscale levels to determine and interpolate the constitutive parameters. The grayscale-dependent behavior of the Mooney-Rivlin parameters was observed to be mostly monotonic and linear, resulting in a linear relationship between the physical material properties (Young's modulus, bulk modulus, shear modulus, and Poisson's ratio) and grayscale value G. Consequently, these approximately linear in grayscale coefficients provided valid and reasonable physical properties and stress-strain curves. Finally, the resulting material model was implemented in a finite element framework and experimentally validated using three test cases involving plate-like geometries with continuous, linear grayscale grading. The validity of the resulting material model was established through these three test cases.

Next, the correlation between light intensity, determined by the grayscale of the mask, and exposure time per layer, which together control the radiant exposure crucial for photopolymerization and the resulting mechanical properties of grayscale MSLA printed materials, was demonstrated in this research. To describe the dependency of mechanical behavior on the printing process parameters, a single design parameter, referred to as the exposure intensity, was introduced, combining grayscale values and exposure time. A visco-hyperelastic constitutive modeling framework for gMSLA 3D printing of functionally graded photopolymers under finite

deformations and dynamic loading conditions was presented. Experimental results confirmed the suitability of the exposure intensity parameter in capturing the relationship between the degree of curing of photopolymer materials and the process parameters. Consequently, the visco-hyperelastic constitutive model was formulated concerning parametric dependency on the exposure intensity value. The Mooney-Rivlin energy function with two parameters was utilized for the non-equilibrium and equilibrium parts of the model, aiming to minimize complexity for characterization, fitting, and numerical implementation without compromising solution stability and convergence. Constitutive parameters were determined by fitting the model to uniaxial tension tests conducted on printed samples with different combinations of grayscale values and exposure times. These coefficients were then parameterized in terms of the exposure intensity. Hyperbolic tangent functions were employed to express the functional dependency of each material parameter on the exposure intensity. This choice aligned with physical considerations, as the stiffness and relaxation time of the material were expected to monotonically increase with the degree of polymerization and exposure intensity, eventually reaching a level when full curing occurred. Validation of this parametric visco-hyperelastic constitutive model was performed through experiments involving various exposure intensity values and strain rates. Stress-strain curves were compared for different strain rates using couples of grayscale values and exposure times with identical exposure intensity. Subsequently, tests were conducted on couples with exposure intensity values not included in the initial data-set used for fitting, allowing for a comparison against model predictions. Finally, the inelastic behavior of the proposed visco-hyperelastic constitutive model was validated for different strain rates under identical exposure intensity.

In the final stage of constitutive modeling in this research, the influence of the process parameters on the resulting geometric and elasto-visco-plastic properties was systematically investigated and characterized. By including the layer thickness, the investigations focused on three critical process parameters that can be easily configured in the preprocessing stage: light intensity in terms of grayscale value, exposure time, and layer thickness. For this purpose, different process parameters were combined, samples were printed, and various mechanical tests were performed. The results showed that a linear elasto-visco-plastic constitutive model accurately approximates the material behavior in uniaxial tension tests to failure, relaxation tests, and cyclic loadings. The unified parameter, the exposure intensity, which captures the influence of all process parameters on the mechanical properties is extended and it is shown that it can be used for optimizing process parameters in practical applications. With this single adjustable design parameter, it is shown that total print time can be reduced by 42% while maintaining identical mechanical behavior for an intricate shell lattice. Furthermore, the impact of process parameters on geometrical deviations using a simple unit cell was examined, showing that smaller exposure intensity values result in shrinkage due to undercuring and larger ones lead to expansion due to overcuring. In addition, these findings are used to show

that deviations can be corrected by changing the original CAD design and grading of the structure according to the exposure intensity. To express the dependency of the constitutive parameters and geometrical deviations in terms of exposure intensity values, again the hyperbolic tangent functions are used. This approach demonstrated good agreement with experimental results in all investigations and can be utilized in practical structural design applications. Nevertheless, the proposed framework of unifying the process parameters and establishing functional relationships with the resulting material properties is generally applicable to other vat photopolymerization 3D printers and materials. Here, numerous experiments were carried out to demonstrate the reliability of the exposure intensity as the unified adjustable process parameter, but in subsequent investigations for other materials significantly less experiments would be sufficient to calibrate the model parameters. Once these parameters are determined, constitutive models can be used to design, simulate, and optimize functionally graded structural designs, geometric deviations can be accounted for in the CAD designs, and the process parameters can be adjusted to minimize printing times.

Afterwards, the developed constitutive model was used to investigate the rate-dependent dissipative behavior of 3D printed graded structures under various strain rates. It was shown that if the average grayscale is identical, the grading strategy does not significantly affect the mechanical behavior of a graded lattice structure under small deformations. Next, the influence of different strain rates on the energy dissipation was studied. A rational function was employed to fit the dissipated energy data, enabling the determination of the strain rate at which maximum dissipation occurs. In general, this research offers insights into the mechanical dissipation behavior of graded 3D printed structures. It also allows for more studies and improvements to make these structures better at absorbing energy.

Finally, this research addressed the challenge posed by the inherent lack of flexibility and low strain-to-failure characteristics in tough resins, limiting their suitability for energy absorption applications. By incorporating a flexible resin into the tough resin, this study aimed to regulate the material's flexibility while reducing its toughness. Through a comprehensive investigation of various mechanical properties, the optimal resin proportion was explored to achieve a balance between strength and flexibility. The development of an elastic-visco-plastic constitutive model allowed for the prediction of mechanical behavior under deformation, facilitating the identification of the ideal resin combination for the intended application. The findings from this study hold significant implications for the design of energy-absorbing structures, potentially opening up new possibilities in material engineering and industrial applications.

In future works, the parameterized constitutive model could be implemented into open-source or commercial finite element software for design, simulation, and optimization of 3D printed graded structures. Investigation of process parameters and their influence on mechanical properties facilitates optimal choice of process parameters toward optimization of the whole printing process. Furthermore, the correlation of geometrical deviations and process

parameters could be implemented into a CAD or slicer software to adjust the geometry according to the expected shrinkage or expansion during printing. The concept of unifying process parameters can be extended to other additive manufacturing methods for polymers, such as SLA, in which process parameters like laser power and laser speed impact the final mechanical properties. Additionally, the energy absorption of graded structures can be investigated, including an analysis of structure failures. This approach enables the exploration of failure control through grayscale manipulation, controlled deformation, and grading strategies aimed at optimizing energy absorption. In this study, a commercial flexible resin was employed to enhance the flexibility of the tough resin. This notion of blending resins can be further expanded to enhance the stiffness of rubbery resins without sacrificing their flexibility. Furthermore, the concept of how process parameters impact mechanical properties can be extended to include other material behaviors, such as damage. Mullin's effect can also be examined by varying process parameters to investigate its influence during cyclic loading.

A. Appendix

A.1. Grayscale Pixel Modification and Color Transformation in Matlab

The provided Matlab code allows for modifying the grayscale values of pixels within a mask. This code enables uniform color transformation for white pixels. It should be noted that additional grading techniques, such as linear and inhomogeneous grading, can be incorporated into this framework. Within the code below, the mask is read layer by layer. The code imports the pixels in the x and y directions and verifies the RGB value of each pixel. If the color is determined to be white, the code replaces it with the color G. Note that the following code is a simplified representation of grading. Additional functions and grading strategies can be implemented in the same way.

Listing A.1 Matlab code for changing grayscale values of the masks.

```
% specify input file names and location
file_name = 'Box';
dir_path = 'img';
file_path = fullfile(dir_path, file_name);
output_path = fullfile(dir_path, 'out');
num_layers = numel(dir(fullfile(dir_path,sprintf('%s*.png',file_name))));

% define Grayscale value G
G= 0.5;

[status, msg] = mkdir(output_path);
if ~isempty(msg)
    fprintf('%s: %s\n', msg, output_path);
    delete(fullfile(output_path,sprintf('%s*.png',file_name)))
end

for i = 0:(num_layers-1) % loop over masks
    strIn = sprintf('%s%05i.png',file_path,i);  % Read png data
    [img, map, alpha] = imread(strIn); % img = rows x columns


```

```
22      % Change map
23      for m = 1:size(img,1)% loop over rows
24          for n= 1:size(img,2) %  loop over columns
25              if  (img(m,n)>200) % identify white pixels
26                  img(m,n) = G * 255; % change grayscale value
27              end
28          end
29      end
30
31      %  Write png output
32      strOut = sprintf('%s\\%s%05i.png',output_path,file_name,i);
33      imwrite(img,strOut);
34  end
```

A.2. Ansys APDL Code for Material Grading

The provided Ansys APDL code demonstrates a method for material grading within a structural analysis. Material grading involves assigning varying material properties to different elements based on their position or other criteria. This code allows for the grading of materials along the x-direction of the structure. The code begins by selecting all elements that will undergo grading. The element selection is saved to a component for further use. Material properties, such as the minimum and maximum Young's modulus (E_min and E_max), are defined. The geometry parameters, specifically the length of the structure in the x-direction, are also set. The grading process begins with a loop that iterates over a large number of elements. The x-coordinate of each element's centroid is obtained. All elements at this x-coordinate location are then selected and assigned to a separate component. The material parameters at the current x position are computed based on the defined grading formula. A new material is created with the computed material properties, and the material number attribute of the selected elements is updated accordingly. The code then proceeds to the next iteration, repeating the process until no more elements are selected. Upon completion of the grading process, the material assignment for all elements is finalized. Finally, the code concludes by saving and sending the defined materials. Note that the following code is a simplified representation of linear grading. Additional functions and grading strategies can be implemented in the same way.

Listing A.2 Ansys parametric design language for material grading.

```
1  /wb,mat,start               !  starting to send materials
2  /com,*********** Send Materials ***********
3  Temperature = 'TEMP' ! Temperature
4  !*------------------------------------------------------!
```

```
! Step 1: Setup                                          !
!-------------------------------------------------------!

! Select all elements to be graded
esel,all

! Save the selected elements to a component
cm,remainingElem,elem

! Define material properties
E_min = 100000
E_max = 200000

! Set the geometry
lengthx = 50

!-----------------------------------------!
! Step 2: Grading Loop Initialization     !
!-----------------------------------------!

*DO, matID, 1, 10000000

! Get the element ID of the next lowest element that is still selected
nextElem = ELNEXT(0)

! Get the x-coordinate of the element's centroid
*get, elemXposition, ELEM, nextElem, CENT, X

! Select all elements at this centroid location
esel, R, CENT, X, elemXposition

! Assign component name to these elements for later reference
cm, elementXgroup, elem

! Compute material parameters at the current x position
factor = elemXposition / lengthx
Ex = E_min + factor * (E_max - E_min)

! Create material with computed Young's modulus
MP, EX, matID, Ex, ! Pa
MP, NUXY, matID, 0.3,

! Change material number attribute of elements
```

```
48 MPCHG, matID, all
49
50 ! Restore the original element selection (excluding the graded elements)
51 cmsel, S, remainingElem !S - Select a new set (default).
52 cmsel, U, elementXgroup !U - Unselect a set from the current set.
53 cm, remainingElem, elem
54
55 ! Get the number of selected elements
56 *GET, num_elem_sel, ELEM, , COUNT
57
58 ! Exit the do-loop if no more elements are selected
59 *if, num_elem_sel, eq, 0, exit
60
61 *ENDDO
62
63 allsel, all
64
65 !-----------------------------------------!
66 !  Grading Completed                !
67 !-----------------------------------------!
68
69 /wb,mat,end                !  done sending materials
```

A.3. Data sheets

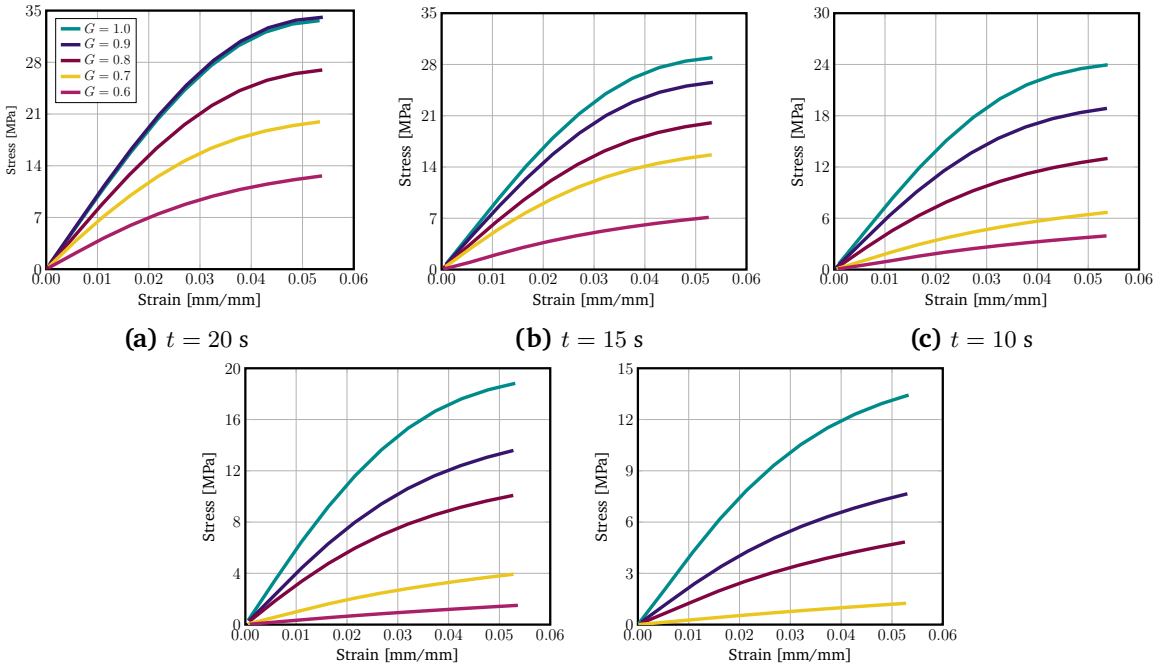

(a) $t = 20$ s **(b)** $t = 15$ s **(c)** $t = 10$ s

(d) $t = 8$ s **(e)** $t = 6$ s

Figure A.1. The experimental stress-strain curves were averaged for quasi-static uniaxial tension tests, considering a grayscale variation with constant exposure times ranging from $t = 20$ s to $t = 6$ s.

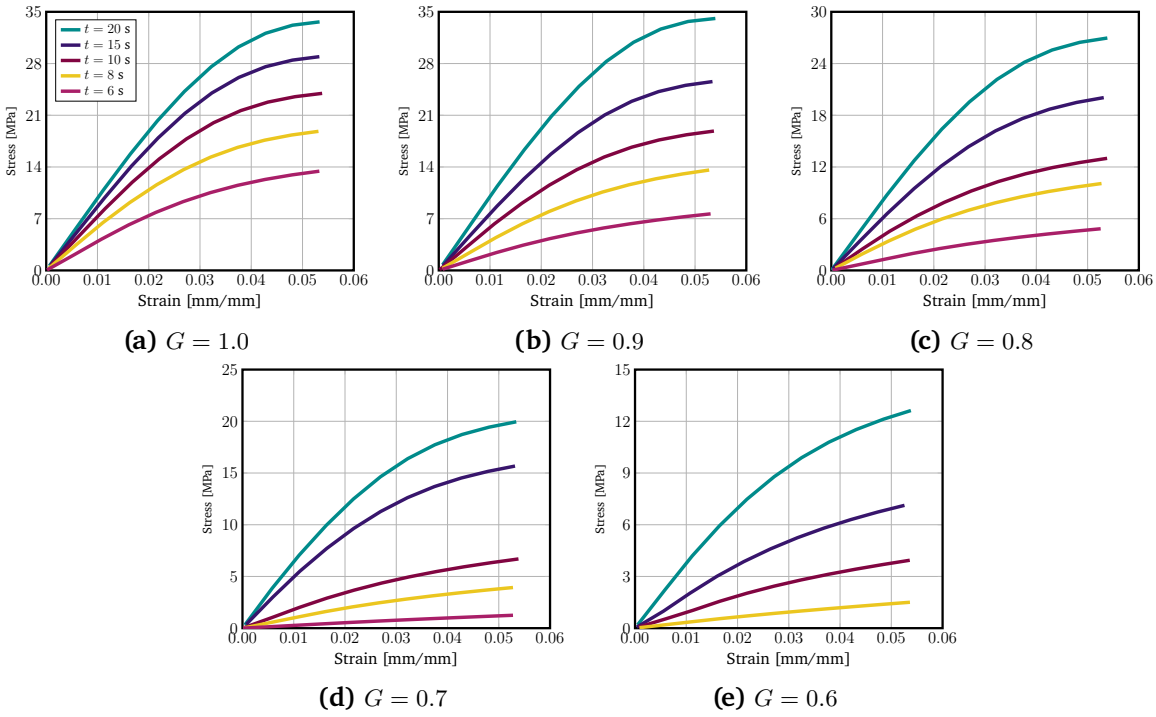

(a) $G = 1.0$ **(b)** $G = 0.9$ **(c)** $G = 0.8$

(d) $G = 0.7$ **(e)** $G = 0.6$

Figure A.2. The experimental stress-strain curves were averaged for quasi-static uniaxial tension tests, considering an exposure time variation with constant grayscale values ranging from $G = 1.0$ to $G = 0.6$.

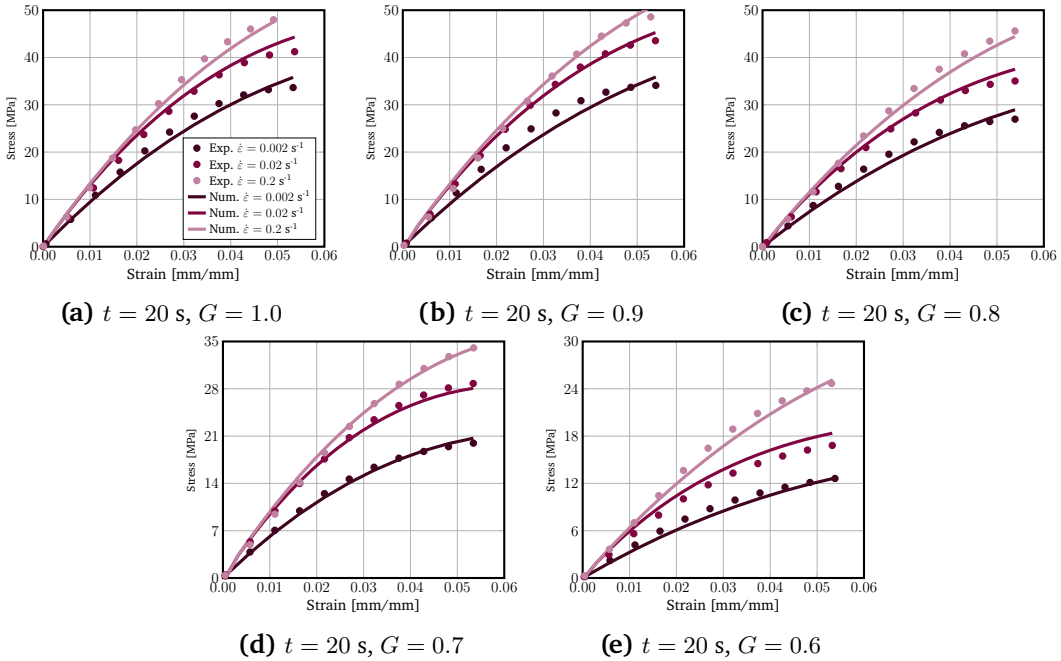

(a) $t = 20$ s, $G = 1.0$ **(b)** $t = 20$ s, $G = 0.9$ **(c)** $t = 20$ s, $G = 0.8$

(d) $t = 20$ s, $G = 0.7$ **(e)** $t = 20$ s, $G = 0.6$

Figure A.3. Experimental stress-strain curves were averaged and combined with a fitted material model of visco-hyperelastic for the purpose of uniaxial tension tests. The grayscales varied from $G = 1.0$ to $G = 0.6$ for constant exposure time $t = 20$ s. Additionally, different strain rates were considered, including $\dot{\varepsilon} = 0.002$ s^{-1} (quasi-static), $\dot{\varepsilon} = 0.02$ s^{-1}, and $\dot{\varepsilon} = 0.2$ s^{-1}.

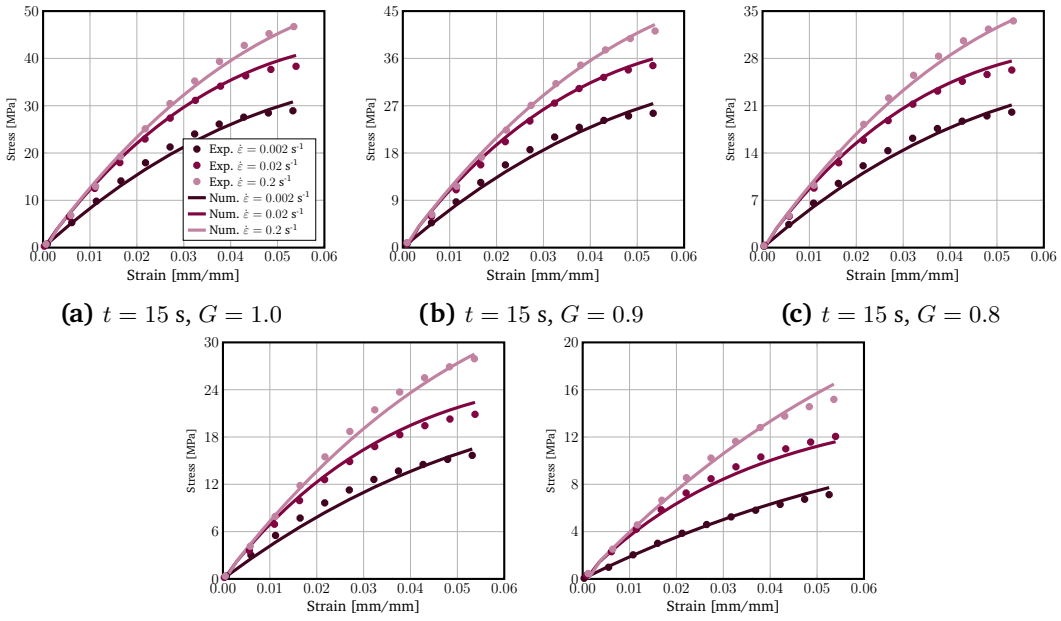

(a) $t = 15$ s, $G = 1.0$ **(b)** $t = 15$ s, $G = 0.9$ **(c)** $t = 15$ s, $G = 0.8$

(d) $t = 15$ s, $G = 0.7$ **(e)** $t = 15$ s, $G = 0.6$

Figure A.4. Experimental stress-strain curves were averaged and combined with a fitted material model of visco-hyperelastic for the purpose of uniaxial tension tests. The grayscales varied from $G = 1.0$ to $G = 0.6$ for constant exposure time $t = 15$ s. Additionally, different strain rates were considered, including $\dot{\varepsilon} = 0.002$ s^{-1} (quasi-static), $\dot{\varepsilon} = 0.02$ s^{-1}, and $\dot{\varepsilon} = 0.2$ s^{-1}.

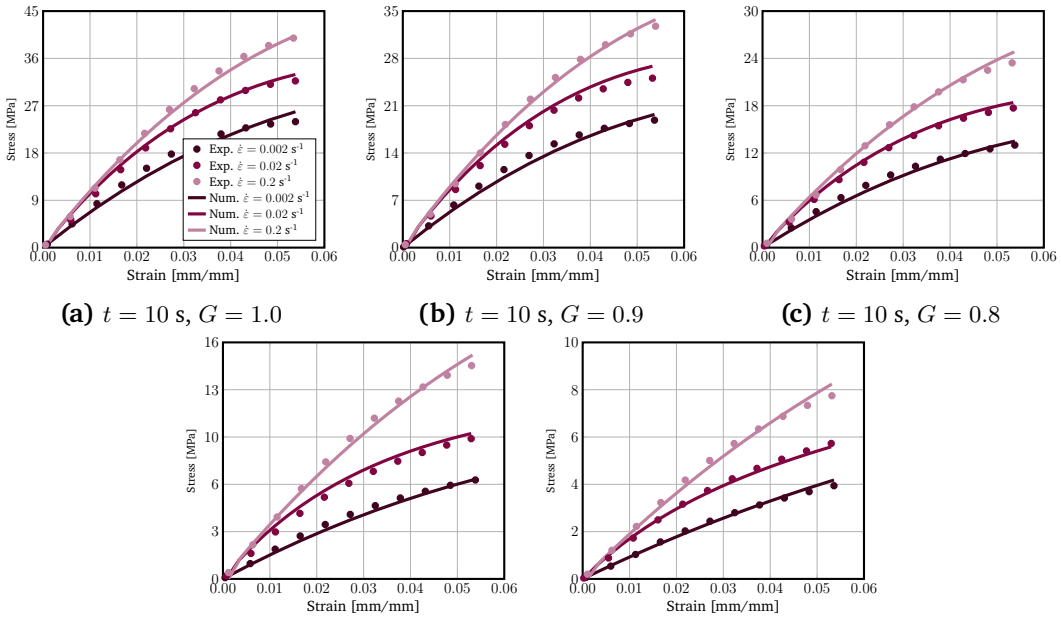

(a) $t = 10$ s, $G = 1.0$ **(b)** $t = 10$ s, $G = 0.9$ **(c)** $t = 10$ s, $G = 0.8$

(d) $t = 10$ s, $G = 0.7$ **(e)** $t = 10$ s, $G = 0.6$

Figure A.5. Experimental stress-strain curves were averaged and combined with a fitted material model of visco-hyperelastic for the purpose of uniaxial tension tests. The grayscales varied from $G = 1.0$ to $G = 0.6$ for constant exposure time $t = 10$ s. Additionally, different strain rates were considered, including $\dot{\varepsilon} = 0.002$ s^{-1} (quasi-static), $\dot{\varepsilon} = 0.02$ s^{-1}, and $\dot{\varepsilon} = 0.2$ s^{-1}.

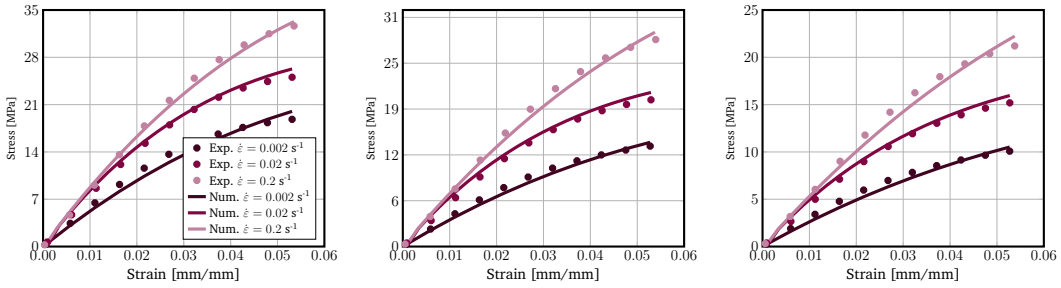

(a) $t = 8$ s, $G = 1.0$ **(b)** $t = 8$ s, $G = 0.9$ **(c)** $t = 8$ s, $G = 0.8$

(d) $t = 8$ s, $G = 0.7$ **(e)** $t = 8$ s, $G = 0.6$

Figure A.6. Experimental stress-strain curves were averaged and combined with a fitted material model of visco-hyperelastic for the purpose of uniaxial tension tests. The grayscales varied from $G = 1.0$ to $G = 0.6$ for constant exposure time $t = 8$ s. Additionally, different strain rates were considered, including $\dot{\varepsilon} = 0.002$ s^{-1} (quasi-static), $\dot{\varepsilon} = 0.02$ s^{-1}, and $\dot{\varepsilon} = 0.2$ s^{-1}.

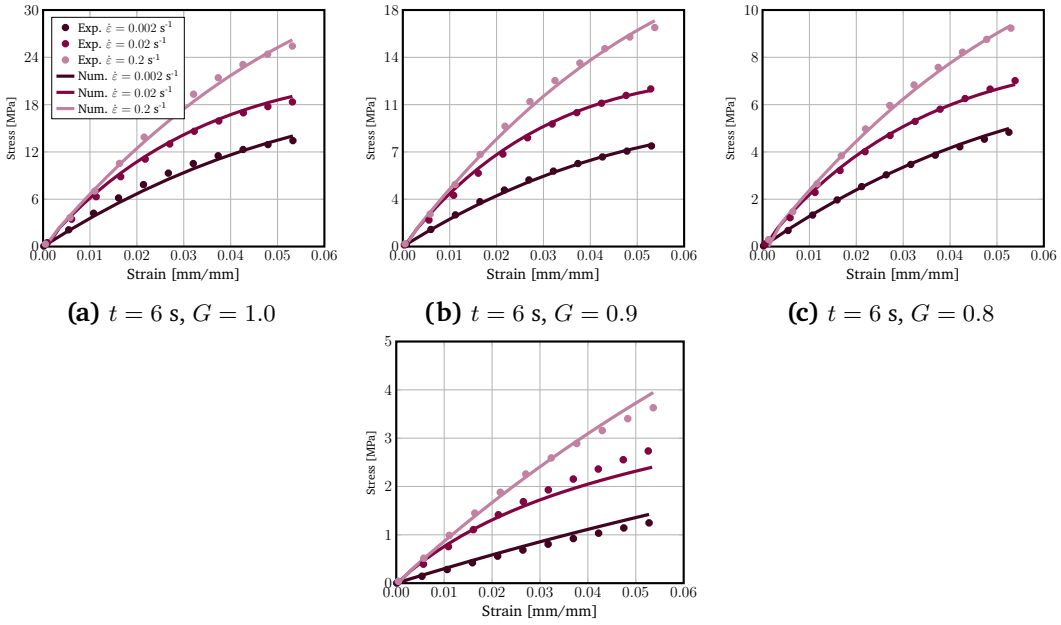

(a) $t = 6$ s, $G = 1.0$ **(b)** $t = 6$ s, $G = 0.9$ **(c)** $t = 6$ s, $G = 0.8$

(d) $t = 6$ s, $G = 0.7$

Figure A.7. Experimental stress-strain curves were averaged and combined with a fitted material model of visco-hyperelastic for the purpose of uniaxial tension tests. The grayscales varied from $G = 1.0$ to $G = 0.6$ for constant exposure time $t = 6$ s. Additionally, different strain rates were considered, including $\dot{\varepsilon} = 0.002$ s^{-1} (quasi-static), $\dot{\varepsilon} = 0.02$ s^{-1}, and $\dot{\varepsilon} = 0.2$ s^{-1}.

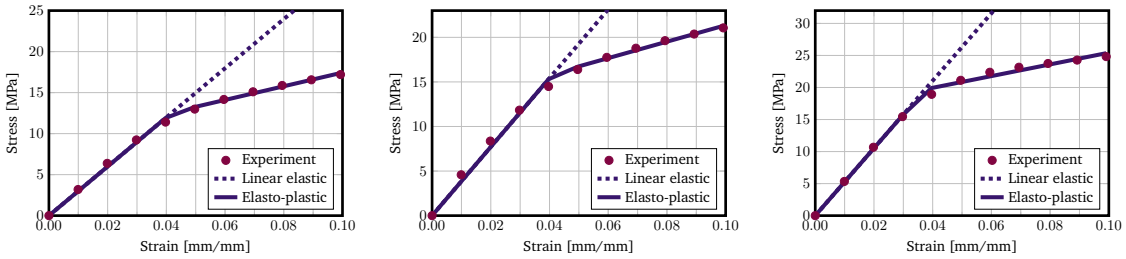

(a) $H_v = 0.91$ ($t = 1.5, G = 1.0, h = 0.05$) **(b)** $H_v = 1.57$ ($t = 3, G = 0.8, h = 0.05$) **(c)** $H_v = 3.60$ ($t = 5, G = 1.0, h = 0.05$)

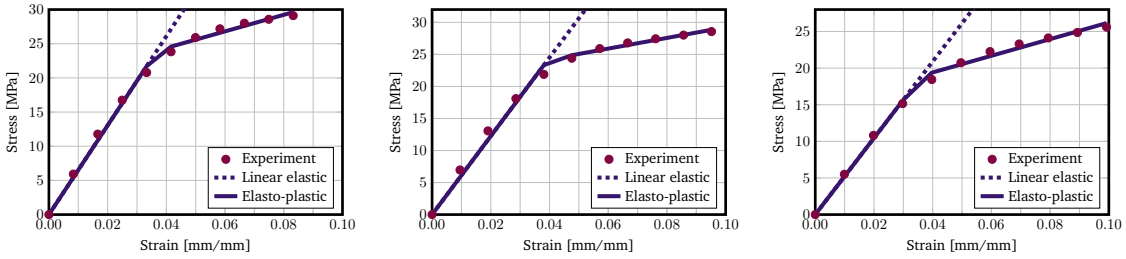

(d) $H_v = 5.71$ ($t = 3, G = 1.0, h = 0.02$) **(e)** $H_v = 5.35$ ($t = 5, G = 0.8, h = 0.02$) **(f)** $H_v = 3.01$ ($t = 5, G = 0.6, h = 0.02$)

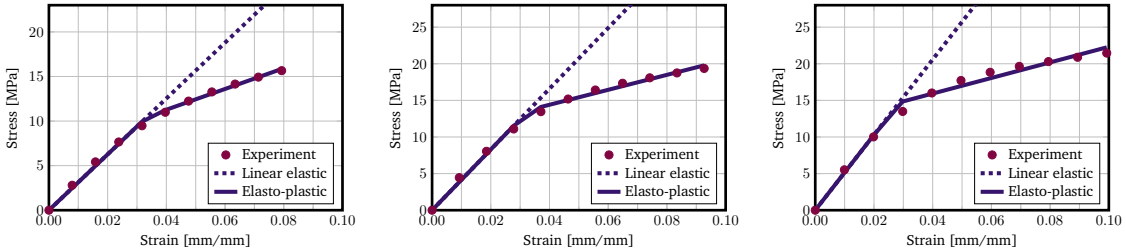

(g) $H_v = 1.43$ ($t = 2.5, G = 1.0, h = 0.1$) **(h)** $H_v = 1.72$ ($t = 3, G = 1.0, h = 0.1$) **(i)** $H_v = 2.52$ ($t = 5, G = 1.0, h = 0.1$)

Figure A.8. Characterization of uniaxial tension behavior of materials through varying grayscale, exposure time, and layer thickness. Averaged experimental stress-strain curves (dots), linear elastic models (dashed), and elasto-plastic models (solid) enable comprehensive analysis and comparison of mechanical properties.

Bibliography

[1] E. J. Jansen, R. E. Sladek, H. Bahar, A. Yaffe, M. J. Gijbels, R. Kuijer, S. K. Bulstra, N. A. Guldemond, I. Binderman, and L. H. Koole. “Hydrophobicity as a design criterion for polymer scaffolds in bone tissue engineering”. In: *Biomaterials* 26.21 (2005), pp. 4423–4431. DOI: 10.1016/j.biomaterials.2004.11.011.

[2] S. V. Murphy and A. Atala. “3D bioprinting of tissues and organs”. In: *Nature Biotechnology* 32.8 (2014), pp. 773–785. DOI: 10.1038/nbt.2958.

[3] C. L. Ventola. “Medical applications for 3D printing: current and projected uses”. In: *Pharmacy and Therapeutics* 39.10 (2014), pp. 704–11.

[4] K. Markstedt, A. Mantas, I. Tournier, H. Martínez Ávila, D. Hägg, and P. Gatenholm. “3D bioprinting human chondrocytes with nanocellulose-alginate bioink for cartilage tissue engineering applications”. In: *Biomacromolecules* 16.5 (2015), pp. 1489–1496. DOI: 10.1021/acs.biomac.5b00188.

[5] K. Qiu, Z. Zhao, G. Haghiashtiani, S. Z. Guo, M. He, R. Su, Z. Zhu, D. B. Bhuiyan, P. Murugan, F. Meng, S. H. Park, C. C. Chu, B. M. Ogle, D. A. Saltzman, B. R. Konety, R. M. Sweet, and M. C. McAlpine. “3D Printed Organ Models with Physical Properties of Tissue and Integrated Sensors”. In: *Advanced Materials Technologies* 3.3 (2018), pp. 1–9. DOI: 10.1002/admt.201700235.

[6] Q. Ge, B. Jian, and H. Li. “Shaping soft materials via digital light processing-based 3D printing: a review”. In: *Forces in Mechanics* 6 (2022), p. 100074. DOI: 10.1016/j.finmec.2022.100074.

[7] F. Yang, M. Zhang, and B. Bhandari. “Recent development in 3D food printing”. In: *Critical Reviews in Food Science and Nutrition* 57.14 (2017), pp. 3145–3153. DOI: 10.1080/10408398.2015.1094732.

[8] X. Zheng, H. Lee, T. H. Weisgraber, M. Shusteff, J. DeOtte, E. B. Duoss, J. D. Kuntz, M. M. Biener, Q. Ge, J. A. Jackson, S. O. Kucheyev, N. X. Fang, and C. M. Spadaccini. “Ultralight, ultrastiff mechanical metamaterials”. In: *Science* 344.6190 (2014), pp. 1373–1377. DOI: 10.1126/science.1252291.

[9] J. A. Jackson, M. C. Messner, N. A. Dudukovic, W. L. Smith, L. Bekker, B. Moran, A. M. Golobic, A. J. Pascall, E. B. Duoss, K. J. Loh, and C. M. Spadaccini. "Field responsive mechanical metamaterials". In: *Science Advances* 4.12 (2018), eaau6419. DOI: 10.1126/sciadv.aau6419.

[10] Y. Kim, H. Yuk, R. Zhao, S. A. Chester, and X. Zhao. "Printing ferromagnetic domains for untethered fast-transforming soft materials". In: *Nature* 558.7709 (2018), pp. 274–279. DOI: 10.1038/s41586-018-0185-0.

[11] X. Kuang, K. Chen, C. K. Dunn, J. Wu, V. C. Li, and H. J. Qi. "3D printing of highly stretchable, shape-memory, and self-healing elastomer toward novel 4D printing". In: *ACS applied materials & interfaces* 10.8 (2018), pp. 7381–7388. DOI: 10.1021/acsami.7b18265.

[12] Z. Ding, C. Yuan, X. Peng, T. Wang, H. J. Qi, and M. L. Dunn. "Direct 4D printing via active composite materials". In: *Science Advances* 3.4 (2017), e1602890. DOI: 10.1126/sciadv.1602890.

[13] Z. Zhao, J. Wu, X. Mu, H. Chen, H. J. Qi, and D. Fang. "Origami by frontal photopolymerization". In: *Science Advances* 3.4 (2017), pp. 1–8. DOI: 10.1126/sciadv.1602326.

[14] X. Kuang, D. J. Roach, J. Wu, C. M. Hamel, Z. Ding, T. Wang, M. L. Dunn, and H. J. Qi. "Advances in 4D printing: Materials and applications". In: *Advanced Functional Materials* 29.2 (2019), p. 1805290. DOI: 10.1002/adfm.201805290.

[15] X. Kuang, J. Wu, K. Chen, Z. Zhao, Z. Ding, F. Hu, D. Fang, and H. J. Qi. "Grayscale digital light processing 3D printing for highly functionally graded materials". In: *Science advances* 5.5 (2019), eaav5790. DOI: 10.1126/sciadv.aav5790.

[16] Q. Zhang, X. Kuang, S. Weng, Z. Zhao, H. Chen, D. Fang, and H. J. Qi. "Rapid Volatilization Induced Mechanically Robust Shape-Morphing Structures toward 4D Printing". In: *ACS Applied Materials & Interfaces* 12.15 (2020), pp. 17979–17987. DOI: 10.1021/acsami.0c02038.

[17] L. Ge, L. Dong, D. Wang, Q. Ge, and G. Gu. "A digital light processing 3D printer for fast and high-precision fabrication of soft pneumatic actuators". In: *Sensors and Actuators A: Physical* 273 (2018), pp. 285–292. DOI: 10.1016/j.sna.2018.02.041.

[18] T.-S. Wei, B. Y. Ahn, J. Grotto, and J. A. Lewis. "3D printing of customized Li-ion batteries with thick electrodes". In: *Advanced Materials* 30.16 (2018), p. 1703027. DOI: 10.1002/adma.201703027.

[19] D. Espalin, D. W. Muse, E. MacDonald, and R. B. Wicker. "3D Printing multifunctionality: Structures with electronics". In: *International Journal of Advanced Manufacturing Technology* 72.5-8 (2014), pp. 963–978. DOI: 10.1007/s00170-014-5717-7.

[20] J. A. Lewis and B. Y. Ahn. “Three-dimensional printed electronics”. In: *Nature* 518.7537 (2015), pp. 42–43. DOI: 10.1038/518042a.

[21] *Roland Berger*. Accessed: October 31, 2023. URL: https://www.rolandberger.com/en/Insights/Publications/Polymer-additive-manufacturing-Market-today-and-in-the-future.html.

[22] I. Gibson, D. Rosen, and B. Stucker. *Additive Manufacturing Technologies: 3D Printing, Rapid Prototyping, and Direct Digital Manufacturing*. 2nd. Springer New York, 2015.

[23] *Mesago Messe Frankfurt GmbH, formnext AM Field Guide compact*. Brochure, 2021.

[24] W. D. Cook and M. Johannson. “The influence of postcuring on the fracture properties of photo-cured dimethacrylate based dental composite resin”. In: *Journal of Biomedical Materials Research* 21.8 (1987), pp. 979–989. DOI: 10.1002/jbm.820210804.

[25] T. Rehbein, A. Lion, M. Johlitz, and A. Constantinescu. “Experimental investigation and modelling of the curing behaviour of photopolymers”. In: *Polymer Testing* 83 (2020), p. 106356. DOI: 10.1016/j.polymertesting.2020.106356.

[26] D. Dendukuri, P. Panda, R. Haghgooie, J. M. Kim, T. A. Hatton, and P. S. Doyle. “Modeling of oxygen-inhibited free radical photopolymerization in a PDMS microfluidic device”. In: *Macromolecules* 41.22 (2008), pp. 8547–8556. DOI: 10.1021/ma801219w.

[27] R. Brighenti, M. P. Cosma, L. Marsavina, A. Spagnoli, and M. Terzano. “Multiphysics modelling of the mechanical properties in polymers obtained via photo-induced polymerization”. In: *International Journal of Advanced Manufacturing Technology* 117.1 (2021), pp. 481–499. DOI: 10.1007/S00170-021-07273-2.

[28] Z. Zhao, X. Mu, N. Sowan, Y. Pei, C. N. Bowman, H. Jerry Qi, and D. Fang. “Effects of oxygen on light activation in covalent adaptable network polymers”. In: *Soft Matter* 11.30 (2015), pp. 6134–6144. DOI: 10.1039/C5SM00555H.

[29] G. I. Peterson, J. J. Schwartz, D. Zhang, B. M. Weiss, M. A. Ganter, D. W. Storti, and A. J. Boydston. “Production of Materials with Spatially-Controlled Cross-Link Density via Vat Photopolymerization”. In: *ACS Applied Materials and Interfaces* 8.42 (2016), pp. 29037–29043. DOI: 10.1021/acsami.6b09768.

[30] L. Yue, S. Macrae Montgomery, X. Sun, L. Yu, Y. Song, T. Nomura, M. Tanaka, and H. Jerry Qi. “Single-vat single-cure grayscale digital light processing 3D printing of materials with large property difference and high stretchability”. In: *Nature Communications* 14.1 (2023), p. 1251. DOI: 10.1038/s41467-023-36909-y.

[31] J. Wu, Z. Zhao, C. M. Hamel, X. Mu, X. Kuang, Z. Guo, and H. J. Qi. “Evolution of material properties during free radical photopolymerization”. In: *Journal of the Mechanics and Physics of Solids* 112 (2018), pp. 25–49. DOI: 10.1016/j.jmps.2017.11.018.

[32] J. R. C. Dizon, A. H. Espera, Q. Chen, and R. C. Advincula. “Mechanical characterization of 3D-printed polymers”. In: *Additive Manufacturing* 20 (2018), pp. 44–67. DOI: 10.1016/J.ADDMA.2017.12.002.

[33] P. Obst, J. Riedelbauch, P. Oehlmann, D. Rietzel, M. Launhardt, S. Schmölzer, T. A. Osswald, and G. Witt. “Investigation of the influence of exposure time on the dual-curing reaction of RPU 70 during the DLS process and the resulting mechanical part properties”. In: *Additive Manufacturing* 32.9 (2020), p. 101002. DOI: 10.1016/J.ADDMA.2019.101002.

[34] A. Garland and G. Fadel. “Design and Manufacturing Functionally Gradient Material Objects With an Off the Shelf 3D printer: Challenges and Solutions”. In: *ASME Journal of Mechanical Design* 137.11 (2015), p. 111407. DOI: 10.1115/1.4031097.

[35] B. Zhang, P. Jaiswal, R. Rai, and S. Nelaturi. “Additive Manufacturing of Functionally Graded Objects: A Review”. In: International Design Engineering Technical Conferences and Computers and Information in Engineering Conference Volume 1A: 36th Computers and Information in Engineering Conference (2016). DOI: 10.1115/DETC2016-60320.

[36] G. H. Loh, E. Pei, D. Harrison, and M. D. Monzón. “An overview of functionally graded additive manufacturing”. en. In: *Additive Manufacturing* 23 (2018), pp. 34–44. DOI: 10.1016/j.addma.2018.06.023.

[37] A. Bandyopadhyay and B. Heer. “Additive manufacturing of multi-material structures”. en. In: *Materials Science and Engineering: R: Reports* 129 (2018), pp. 1–16. DOI: 10.1016/j.mser.2018.04.001.

[38] N. Oxman. “Variable property rapid prototyping”. In: *Virtual and Physical Prototyping* 6.1 (2011), pp. 3–31. DOI: 10.1080/17452759.2011.558588.

[39] O. Weeger, Y. Kang, S.-K. Yeung, and M. Dunn. “Optimal Design and Manufacture of Active Rod Structures with Spatially Variable Materials”. In: *3D Printing and Additive Manufacturing* 3.4 (2016), pp. 204–215. DOI: 10.1089/3dp.2016.0039.

[40] I. F. Ituarte, N. Boddeti, V. Hassani, M. L. Dunn, and D. W. Rosen. “Design and additive manufacture of functionally graded structures based on digital materials”. en. In: *Additive Manufacturing* 30 (2019), p. 100839. DOI: 10.1016/j.addma.2019.100839.

[41] Q. Ge, A. H. Sakhaei, H. Lee, C. K. Dunn, N. X. Fang, and M. L. Dunn. “Multimaterial 4D printing with tailorable shape memory polymers”. In: *Scientific reports* 6.1 (2016), pp. 1–11. DOI: 10.1038/srep31110.

[42] K. Kowsari, S. Akbari, D. Wang, N. X. Fang, and Q. Ge. “High-efficiency high-resolution multimaterial fabrication for digital light processing-based three-dimensional printing”. In: *3D Printing and Additive Manufacturing* 5.3 (2018), pp. 185–193. DOI: 10.1089/3dp.2018.0004.

[43] Y. Lu, G. Mapili, G. Suhali, S. Chen, and K. Roy. “A digital micro-mirror device-based system for the microfabrication of complex, spatially patterned tissue engineering scaffolds”. In: *Journal of Biomedical Materials Research Part A* 77A.2 (2006), pp. 396–405. DOI: 10.1002/jbm.a.30601.

[44] J. H. Na, N. P. Bende, J. Bae, C. D. Santangelo, and R. C. Hayward. “Grayscale gel lithography for programmed buckling of non-Euclidean hydrogel plates”. In: *Soft Matter* 12.22 (2016), pp. 4985–4990. DOI: 10.1039/c6sm00714g.

[45] D. Xue, Y. Wang, and D. Mei. “Multi-step exposure method for improving structure flatness in digital light processing-based printing”. In: *Journal of Manufacturing Processes* 39 (2019), pp. 106–113. DOI: 10.1016/j.jmapro.2019.02.013.

[46] D. Kolesky, R. Truby, A. Gladman, T. Busbee, K. Homan, and J. Lewis. “3D Bioprinting of Vascularized, Heterogeneous Cell-Laden Tissue Constructs”. In: *Advanced Materials* 26 (2014), pp. 3124–3130. DOI: 10.1002/adma.201305506.

[47] Q. Mu, L. Wang, C. Dunn, X. Kuang, F. Duan, Z. Zhang, H. Qi, and T. Wang. “Digital light processing 3D printing of conductive complex structures”. In: *Additive Manufacturing* 18 (2017), pp. 74–83. DOI: 10.1016/j.addma.2017.08.011.

[48] S. Norris, P. Tseng, and A. Kasko. “Direct Gradient Photolithography of Photodegradable Hydrogels with Patterned Stiffness Control with Submicrometer Resolution”. In: *ACS Biomaterials Science & Engineering* 2 (2016), pp. 1309–1318. DOI: 10.1021/acsbiomaterials.6b00237.

[49] J. Wu, Z. Zhao, X. Kuang, C. M. Hamel, D. Fang, and H. J. Qi. “Reversible shape change structures by grayscale pattern 4D printing”. In: *Multifunctional Materials* 1.1 (2018), p. 015002. DOI: 10.1088/2399-7532/aac322.

[50] Z. Zhao, J. Wu, X. Mu, H. Chen, H. J. Qi, and D. Fang. “Desolvation Induced Origami of Photocurable Polymers by Digit Light Processing”. In: *Macromolecular Rapid Communications* 38.13 (2017), pp. 1–6. DOI: 10.1002/marc.201600625.

[51] Y. Xiang, Cody Schilling, N. Arora, A. J. Boydston, and S. Rudykh. “Mechanical characterization and constitutive modeling of visco-hyperelasticity of photocured polymers”. In: *Additive Manufacturing* 36 (2020), p. 101511. DOI: 10.1016/j.addma.2020.101511.

[52] M. Robinson, S. Soe, R. Johnston, R. Adams, B. Hanna, R. Burek, G. McShane, R. Celeghini, M. Alves, and P. Theobald. “Mechanical characterisation of additively manufactured elastomeric structures for variable strain rate applications”. In: *Additive Manufacturing* 27 (2019), pp. 398–407. DOI: 10.1016/j.addma.2019.03.022.

[53] J. Liljenhjerte, P. Upadhyaya, and S. Kumar. “Hyperelastic strain measurements and constitutive parameters identification of 3D printed soft polymers by image processing”. In: *Additive Manufacturing* 11 (2016), pp. 40–48. DOI: 10.1016/j.addma.2016.03.005.

[54] F. F. Abayazid and M. Ghajari. “Material characterisation of additively manufactured elastomers at different strain rates and build orientations”. In: *Additive Manufacturing* 33 (2020), p. 101160. DOI: 10.1016/j.addma.2020.101160.

[55] T. Rehbein, M. Johlitz, A. Lion, K. Sekmen, and A. Constantinescu. “Temperature-and degree of cure-dependent viscoelastic properties of photopolymer resins used in digital light processing”. In: *Progress in Additive Manufacturing* 6.4 (2021), pp. 743–756. DOI: 10.1007/s40964-021-00194-2.

[56] Z. Zhao, D. Wu, H. Chen, H. Qi, and D. Fang. “Indentation experiments and simulations of nonuniformly photocrosslinked polymers in 3D printed structures”. In: *Additive Manufacturing* 35 (2020), p. 101420. DOI: 10.1016/j.addma.2020.101420.

[57] Y. Xiang, D. Zhong, S. Rudykh, H. Zhou, S. Qu, and W. Yang. “A Review of Physically Based and Thermodynamically Based Constitutive Models for Soft Materials”. In: *Journal of Applied Mechanics, Transactions ASME* 87.11 (2020), pp. 1–21. DOI: 10.1115/1.4047776.

[58] Y. Yang, L. Li, and J. Zhao. “Mechanical property modeling of photosensitive liquid resin in stereolithography additive manufacturing: Bridging degree of cure with tensile strength and hardness”. In: *Materials and Design* 162 (2019), pp. 418–428. DOI: 10.1016/j.matdes.2018.12.009.

[59] V. K. Chinthala, S. S. Mulay, and A. B. Harish. “Constitutive modeling of pH-sensitive hydrogel: Multi-physics coupling of electromagnetics with mechanics and thermodynamics”. In: *Mechanics of Materials* 161 (2021), p. 104002. DOI: 10.1016/j.mechmat.2021.104002.

[60] R. Brighenti, L. Marsavina, M. P. Marghitas, M. P. Cosma, and M. Montanari. “Mechanical characterization of additively manufactured photopolymerized polymers”. In: *Mechanics of Advanced Materials and Structures* 30 (2022), pp. 1–12. DOI: 10.1080/15376494.2022.2045655.

[61] S. Yoshida, Y. Takahata, S. Horiuchi, H. Kurata, and M. Yamamoto. “Numerical model of radical photopolymerization based on interdiffusion”. In: *International Journal of Polymer Science* 2014 (2014), pp. 1–8. DOI: 10.1155/2014/243895.

[62] R. Brighenti and M. P. Cosma. “Mechanical behavior of photopolymerized materials”. In: *Journal of the Mechanics and Physics of Solids* 153 (2021), p. 104456. DOI: 10.1016/j.jmps.2021.104456.

[63] M. Hossain and P. Steinmann. “Continuum physics of materials with time-dependent properties: reviewing the case of polymer curing”. In: *Advances in applied mechanics* 48 (2015), pp. 141–259. DOI: 10.1016/bs.aams.2015.10.003.

[64] M. Zarrelli, A. A. Skordos, and I. K. Partridge. “Toward a constitutive model for cure-dependent modulus of a high temperature epoxy during the cure”. In: *European Polymer Journal* 46.8 (2010), pp. 1705–1712. DOI: 10.1016/J.EURPOLYMJ.2010.06.002.

[65] A. Vitale, M. G. Hennessy, O. K. Matar, and J. T. Cabral. “Interfacial profile and propagation of frontal photopolymerization waves”. In: *Macromolecules* 48.1 (2015), pp. 198–205. DOI: 10.1021/ma5021215.

[66] M. Hossain and P. Steinmann. “Degree of cure-dependent modelling for polymer curing processes at small-strain. Part I: consistent reformulation”. In: *Computational Mechanics* 53 (2014), pp. 777–787. DOI: 10.1007/s00466-013-0929-5.

[67] M. Hossain, G. Possart, and P. Steinmann. “A finite strain framework for the simulation of polymer curing. Part I: elasticity”. In: *Computational Mechanics* 44 (2009), pp. 621–630. DOI: 10.1007/s00466-009-0397-0.

[68] S. Hartmann. “Numerical studies on the identification of the material parameters of Rivlin’s hyperelasticity using tension-torsion tests”. In: *Acta Mechanica* 148.1-4 (2001), pp. 129–155. DOI: 10.1007/BF01183674.

[69] Y. I. Dimitrienko. *Nonlinear continuum mechanics and large inelastic deformations*. Vol. 174. Springer Science & Business Media, 2010.

[70] R. W. Ogden, G. Saccomandi, and I. Sgura. “Fitting hyperelastic models to experimental data”. In: *Computational Mechanics* 34.6 (2004), pp. 484–502. DOI: 10.1007/s00466-004-0593-y.

[71] J. C. Simo. “On a fully three-dimensional finite-strain viscoelastic damage model: Formulation and computational aspects”. In: *Computer Methods in Applied Mechanics and Engineering* 60.2 (1987), pp. 153–173. DOI: 10.1016/0045-7825(87)90107-1.

[72] M. Hossain, G. Possart, and P. Steinmann. “A finite strain framework for the simulation of polymer curing. Part II. Viscoelasticity and shrinkage”. In: *Computational Mechanics* 46 (2010), pp. 363–375. DOI: 10.1016/j.addma.2020.101511.

[73] R. S. Rivlin, D. W. Saunders, and E. N. D. C. Andrade. “Large elastic deformations of isotropic materials VII. Experiments on the deformation of rubber”. In: *Philosophical Transactions of the Royal Society of London. Series A, Mathematical and Physical Sciences* 243.865 (1951), pp. 251–288. DOI: 10.1098/rsta.1951.0004.

[74] T. Y. Chang, A. F. Saleeb, and G. Li. “Large strain analysis of rubber-like materials based on a perturbed Lagrangian variational principle”. In: *Computational Mechanics* 8.4 (1991), pp. 221–233. DOI: 10.1007/BF00577376.

[75] L. Treloar. “The elasticity and related properties of rubbers”. In: *Reports on progress in physics* 36.7 (1973), p. 755. DOI: 10.1088/0034-4885/36/7/001.

[76] J. B. Pascual-Francisco, L. I. Farfan-Cabrera, E. Cuan-Urquizo, A. Álvarez-Trejo, and A. Roman-Flores. “Additive manufacturing and viscoelasticity evaluation of Bézier metamaterials fabricated via vat photopolymerization”. In: *Additive Manufacturing* 60 (2022), p. 103281. DOI: 10.1016/j.addma.2022.103281.

[77] D. Wang, K. Wu, G. Li, and L. Wang. “The viscoelastic mechanical property and constitutive models of 3D printed photopolymer”. In: *Rapid Prototyping Journal* 27.2 (2021), pp. 346–354. DOI: 10.1108/RPJ-07-2020-0163.

[78] Y. Wang, X. Li, Y. Chen, and C. Zhang. “Strain rate dependent mechanical properties of 3D printed polymer materials using the DLP technique”. In: *Additive Manufacturing* 47 (2021), p. 102368. DOI: 10.1016/j.addma.2021.102368.

[79] K. Upadhyay, G. Subhash, and D. Spearot. “Hyperelastic constitutive modeling of hydrogels based on primary deformation modes and validation under 3D stress states”. In: *International Journal of Engineering Science* 154 (2020), p. 103314. DOI: 10.1016/j.ijengsci.2020.103314.

[80] M. Bodaghi, A. Damanpack, G. Hu, and W. Liao. “Large deformations of soft metamaterials fabricated by 3D printing”. In: *Materials & Design* 131 (2017), pp. 81–91. DOI: 10.1016/j.matdes.2017.06.002.

[81] M. Bodaghi and W. Liao. “4D printed tunable mechanical metamaterials with shape memory operations”. In: *Smart Materials and Structures* 28.4 (2019), p. 045019. DOI: 10.1088/1361-665X/ab0b6b.

[82] I. Valizadeh and O. Weeger. “Parametric visco-hyperelastic constitutive modeling of functionally graded 3D printed polymers”. In: *International Journal of Mechanical Sciences* 226 (2022), p. 107335. DOI: 10.1016/j.ijmecsci.2022.107335.

[83] S. M. Montgomery, F. Demoly, K. Zhou, and H. J. Qi. “Pixel-Level Grayscale Manipulation to Improve Accuracy in Digital Light Processing 3D Printing”. In: *Advanced Functional Materials* (2023), p. 2213252. DOI: 10.1002/adfm.202213252.

[84] J. Mueller, K. H. Matlack, K. Shea, and C. Daraio. “Energy Absorption Properties of Periodic and Stochastic 3D Lattice Materials”. In: *Advanced Theory and Simulations* 2.10 (2019), p. 1900081. DOI: 10.1002/adts.201900081.

[85] S. Wang, J. Wang, Y. Xu, W. Zhang, and J. Zhu. “Compressive behavior and energy absorption of polymeric lattice structures made by additive manufacturing”. In: *Frontiers of Mechanical Engineering 2019 15:2* 15.2 (2019), pp. 319–327. DOI: 10.1007/S11465-019-0549-7.

[86] L. Bai, C. Gong, X. Chen, Y. Sun, L. Xin, H. Pu, Y. Peng, and J. Luo. “Mechanical properties and energy absorption capabilities of functionally graded lattice structures: Experiments and simulations”. In: *International Journal of Mechanical Sciences* 182 (2020), p. 105735. DOI: 10.1016/J.IJMECSCI.2020.105735.

[87] I. Maskery, N. T. Aboulkhair, A. O. Aremu, C. J. Tuck, and I. A. Ashcroft. “Compressive failure modes and energy absorption in additively manufactured double gyroid lattices”. In: *Additive Manufacturing* 16 (2017), pp. 24–29. DOI: 10.1016/J.ADDMA.2017.04.003.

[88] Z. P. Sun, Y. B. Guo, and V. P. Shim. “Characterisation and modeling of additively-manufactured polymeric hybrid lattice structures for energy absorption”. In: *International Journal of Mechanical Sciences* 191 (2021), p. 106101. DOI: 10.1016/J.IJMECSCI.2020.106101.

[89] S. Shan, S. H. Kang, J. R. Raney, P. Wang, L. Fang, F. Candido, J. A. Lewis, and K. Bertoldi. “Multistable Architected Materials for Trapping Elastic Strain Energy”. In: *Advanced Materials* 27.29 (2015), pp. 4296–4301. DOI: 10.1002/ADMA.201501708.

[90] L. Wu, X. Xi, B. Li, and J. Zhou. “Multi-Stable Mechanical Structural Materials”. In: *Advanced Engineering Materials* 20.2 (2018), p. 1700599. DOI: 10.1002/ADEM.201700599.

[91] T. Frenzel, C. Findeisen, M. Kadic, P. Gumbsch, M. T. Wegener Frenzel, M. Kadic, M. Wegener, C. Findeisen, and P. Gumbsch. “Tailored Buckling Microlattices as Reusable Light-Weight Shock Absorbers”. In: *Advanced Materials* 28.28 (2016), pp. 5865–5870. DOI: 10.1002/ADMA.201600610.

[92] S. Y. Jeon, B. Shen, N. A. Traugutt, Z. Zhu, L. Fang, C. M. Yakacki, T. D. Nguyen, and S. H. Kang. “Synergistic Energy Absorption Mechanisms of Architected Liquid Crystal Elastomers”. In: *Advanced Materials* 34.14 (2022), p. 2200272. DOI: 10.1002/ADMA.202200272.

[93] M. Bodaghi, A. Serjouei, A. Zolfagharian, M. Fotouhi, H. Rahman, and D. Durand. “Reversible energy absorbing meta-sandwiches by FDM 4D printing”. In: *International Journal of Mechanical Sciences* 173 (2020), p. 105451. DOI: 10.1016/J.IJMECSCI.2020.105451.

[94] X. Tan, S. Chen, S. Zhu, B. Wang, P. Xu, K. Yao, and Y. Sun. “Reusable metamaterial via inelastic instability for energy absorption”. In: *International Journal of Mechanical Sciences* 155 (2019), pp. 509–517. DOI: 10.1016/J.IJMECSCI.2019.02.011.

[95] S. Sun, N. An, G. Wang, M. Li, and J. Zhou. “Snap-back induced hysteresis in an elastic mechanical metamaterial under tension”. In: *Applied Physics Letters* 115.9 (2019), p. 091901. DOI: 10.1063/1.5119275.

[96] H. Rahman, E. Yarali, A. Zolfagharian, A. Serjouei, and M. Bodaghi. “Energy absorption and mechanical performance of functionally graded soft–hard lattice structures”. In: *Materials* 14.6 (2021), p. 1366. DOI: 10.3390/ma14061366.

[97] I. Valizadeh, T. Tayyarian, and O. Weeger. “Influence of process parameters on geometric and elasto-visco-plastic material properties in vat photopolymerization”. In: *Additive Manufacturing* 72 (2023), p. 103641. DOI: 10.1016/j.addma.2023.103641.

[98] C. Decker. “Photoinitiated crosslinking polymerisation”. In: *Progress in Polymer Science* 21.4 (1996), pp. 593–650. DOI: 10.1016/0079-6700(95)00027-5.

[99] I. Valizadeh, A. Al Aboud, E. Dörsam, and O. Weeger. “Tailoring of functionally graded hyperelastic materials via grayscale mask stereolithography 3D printing”. In: *Additive Manufacturing* 47 (2021), p. 102108. DOI: 10.1016/j.addma.2021.102108.

[100] Y. Wang, D. Xue, and D. Mei. “Projection-Based Continuous 3D Printing Process With the Grayscale Display Method”. In: *Journal of Manufacturing Science and Engineering* 142.2 (2020), pp. 1–10. DOI: 10.1115/1.4045616.

[101] *Prusa Research a.s., https://www.prusa3d.com, 2021*.

[102] I. Valizadeh, P. Steinmann, and A. Javili. “Growth-induced instabilities of an elastic film on a viscoelastic substrate: analytical solution and computational approach via eigenvalue analysis”. In: *Journal of Mechanics of Materials and Structures* 13.4 (2018), pp. 571–585. DOI: 10.2140/jomms.2018.13.571.

[103] R. W. Ogden and E. Sternberg. “Nonlinear Elastic Deformations”. In: *Journal of Applied Mechanics* 52.3 (1985), pp. 740–741. DOI: 10.1115/1.3169137.

[104] P. Wriggers. *Nonlinear finite element methods*. Springer Science & Business Media, 2008. DOI: 10.1007/978-3-540-71001-1.

[105] W. Noll, B. D. Coleman, and W. Noll. “The thermodynamics of elastic materials with heat conduction and viscosity”. In: *The Foundations of Mechanics and Thermodynamics: Selected Papers* (1974), pp. 145–156. DOI: 10.1007/978-3-642-65817-4_9.

[106] B. D. Coleman and M. E. Gurtin. “Thermodynamics with Internal State Variables”. In: *The Journal of Chemical Physics* 47.2 (May 2004), pp. 597–613. DOI: 10.1063/1.1711937.

[107] S. Wang, Y. Ma, Z. Deng, K. Zhang, and S. Dai. “Implementation of an elastoplastic constitutive model for 3D-printed materials fabricated by stereolithography”. In: *Additive Manufacturing* 33 (2020), p. 101104. DOI: 10.1016/j.addma.2020.101104.

[108] R. S. Rivlin, P. Trans, and R. S. Lond. “Large elastic deformations of isotropic materials IV. further developments of the general theory”. In: *Philosophical Transactions of the Royal Society of London. Series A, Mathematical and Physical Sciences* 241.835 (1948), pp. 379–397. DOI: 10.1098/rsta.1948.0024.

[109] G. A. Holtzapfel. *Nonlinear Solid Mechanics: A Continuum Approach for Engineering*. Wiley, Chichester, England, 2000.

[110] J. C. Simo and T. J. Hughes. *Computational inelasticity*. Vol. 7. Springer Science & Business Media, 2006. DOI: 10.1007/b98904.

[111] M. Kaliske and H. Rothert. “Formulation and implementation of three-dimensional viscoelasticity at small and finite strains”. In: *Computational Mechanics* 19.3 (1997), pp. 228–239. DOI: 10.1007/s004660050171.

[112] S. M. Goh, M. N. Charalambides, and J. G. Williams. “Determination of the constitutive constants of non-linear viscoelastic materials”. In: *Mechanics of Time-Dependent Materials* 8 (2004), pp. 255–268. DOI: 10.1023/B:MTDM.0000046750.65395.fe.

[113] J. Zhou, L. Jiang, and R. E. Khayat. “A micro–macro constitutive model for finite-deformation viscoelasticity of elastomers with nonlinear viscosity”. In: *Journal of the Mechanics and Physics of Solids* 110 (2018), pp. 137–154. DOI: 10.1016/j.jmps.2017.09.016.

[114] D. S. Pearson and E. Helfand. “Viscoelastic Properties of Star-Shaped Polymers”. In: *Macromolecules* 17.4 (1984), pp. 888–895. DOI: 10.1021/ma00134a060.

[115] M. Mooney. “A theory of large elastic deformation”. In: *Journal of Applied Physics* 11 (1940), pp. 582–592. DOI: 10.1063/1.1712836.

[116] ANSYS, Inc. *Ansys® Academic Research Mechanical, Release 2021 R2 (21.2), Help System, Mechanical APDL Theory Reference Guide*. ANSYS, Inc. 2021.

[117] J. Simo. “A framework for finite strain elastoplasticity based on maximum plastic dissipation and the multiplicative decomposition: Part I. Continuum formulation”. In: *Computer Methods in Applied Mechanics and Engineering* 66.2 (1988), pp. 199–219. DOI: 10.1016/0045-7825(88)90076-X.

[118] P. Steinmann and K. Runesson. *The catalogue of computational material models: basic geometrically linear models in 1D*. Springer Nature, 2021. DOI: 10.1007/978-3-030-63684-5.

[119] J. C. Simo. “Algorithms for static and dynamic multiplicative plasticity that preserve the classical return mapping schemes of the infinitesimal theory”. In: *Computer Methods in Applied Mechanics and Engineering* 99.1 (1992), pp. 61–112. DOI: 10.1016/0045-7825(92)90123-2.

[120] J. R. Barber. *Elasticity*. Springer, 2002. DOI: 10.1007/978-90-481-3809-8.

[121] N. S. Ottosen and M. Ristinmaa. *The mechanics of constitutive modeling*. Elsevier, 2005.

[122] J. N. Goodier and S. Timoshenko. *Theory of Elasticity*. McGraw-Hill, 1969.

[123] P. G. Ciarlet. *Mathematical Elasticity: Three-Dimensional Elasticity*. Philadelphia, PA: Society for Industrial and Applied Mathematics, 2021. DOI: 10.1137/1.9781611976786.

[124] A. D. Lindsay, D. R. Gaston, C. J. Permann, J. M. Miller, D. Andrs, A. E. Slaughter, F. Kong, J. Hansel, R. W. Carlsen, C. Icenhour, L. Harbour, G. L. Giudicelli, R. H. Stogner, P. German, J. Badger, S. Biswas, L. Chapuis, C. Green, J. Hales, T. Hu, W. Jiang, Y. S. Jung, C. Matthews, Y. Miao, A. Novak, J. W. Peterson, Z. M. Prince, A. Rovinelli, S. Schunert, D. Schwen, B. W. Spencer, S. Veeraraghavan, A. Recuero, D. Yushu, Y. Wang, A. Wilkins, and C. Wong. “2.0 - MOOSE: Enabling massively parallel multiphysics simulation”. In: *SoftwareX* 20 (2022), p. 101202. DOI: 10.1016/j.softx.2022.101202.

[125] M. A. Meyers and K. K. Chawla. *Mechanical behavior of materials*. Cambridge university press, 2008.